Challenge Journal of
STRUCTURAL MECHANICS

Vol.9 No.1 (2023)

auxetic building codes compressive strength dynamic analysis earthquake finite element analysis finite element method girder bridge mechanical properties metaheuristic algorithms modal analysis optimization prestresing pushover analysis reinforced concrete seismic design shallow foundations smart concrete steel structures structural dynamics temperature effects thick plate wind

ISSN 2149-8024

TULPAR ACADEMIC PUBLISHING

Challenge Journal of Structural Mechanics

E-mail: *cjsmec@challengejournal.com*

Web page: *cjsmec.challengejournal.com*

TULPAR Academic Publishing
www.tulparpublishing.com

Challenge Journal of Structural Mechanics

CONTENTS

Research Articles

Reviews

TULPAR ACADEMIC PUBLISHING

Challenge Journal of Structural Mechanics

Research Article

Natural frequencies of porous orthotropic two-layered plates within the shear deformation theory

Ferruh Turan [a,*]

[a] *Department of Civil Engineering, Ondokuz Mayıs University, 55139 Samsun, Türkiye*

ABSTRACT

This paper analyzes the natural frequencies of porous orthotropic laminated composite plates with two different porosity models based on the higher-order shear deformation theory. The fundamental relations of natural frequency analysis are derived by using the virtual work principle and hyperbolical shear deformation theory. The obtained partial differential equations system is reduced to an ordinary differential equations system via approximation functions suitable for simply supported boundary conditions and the Galerkin method. After some mathematical operations, the natural frequency equation of porous orthotropic laminated composite plates is obtained in the framework of hyperbolical shear deformation theory. The natural frequency equation based on the classical laminated plate theory can be determined by ignoring the shear strains in the theoretical formulations. After two validation studies by using appropriate results in the literature, parametric analyses are performed to show the sensitivity of natural frequencies to shear deformation, porosity model, orthotropy, layer sequence, and geometric properties.

ARTICLE INFO

Article history:
Received 9 August 2022
Revised 2 November 2022
Accepted 18 November 2022

Keywords:
Porosity
Porous plate
Laminated composite
Vibration
Shear deformation
Orthotropy

1. Introduction

Structural elements in many industries such as aviation, maritime, automotive, and military are required to consist of lightweight materials with high strength, excellent energy absorption, and low thermal conductivity. The pores in the structural elements can also occur as micro-defects. Therefore, the sensitivity of structural responses such as stability and vibration frequency to micro-defects or pores needs to be analyzed in detail.

Zhou et al. (2020) analyzed the free vibration response of rectangular functionally graded plates with two different distributed interior pores and platelets of graphene. Zhong et al. (2021) investigated the in-plane vibration of porous circular plates with porosity distributions in thickness and radial directions. Teng and Xi (2021) examined the porosity effect on the free vibration and stability behavior of functionally graded rectangular plates. Pan et al. (2021) analyzed the free vibration problem of graphene-reinforced porous plates. Pham et al. (2021) investigated static and dynamic responses of functionally graded nano-plates with uneven and logarithmic-uneven porosity distributions. Esen and Özmen (2022) studied the thermal vibration and buckling responses of functionally graded nano-plates modeled by porosity distribution functions. Lahdiri and Kadri (2022) examined the effect of porosity distributions on the free vibration of the multi-directional functionally graded porous plates. Chen et al. (2022) investigated the free in-plane vibration response of functionally graded plates with porosity distributions in the thickness and in-plane directions.

Neglecting transverse shear deformations while investigating structural elements' static and dynamic responses leads to inaccurate results. Therefore, there is an increasing tendency for researchers to develop novel theories that include the effects of transverse shear deformations (Aydogdu 2009; Mahi et al. 2015; Shi et al. 2018). Depending on the development of novel shear deformations, articles have appeared in the literature on examining the static and dynamic responses of porous structure components within the scope of shear defor-

* *Corresponding author*. Tel.: +90-362-312-1919 ; Fax: +90-362-457-6091 ; E-mail address: ferruh.turan@omu.edu.tr (F. Turan)
ISSN: 2149-8024 / DOI: https://doi.org/10.20528/cjsmec.2023.01.001

mation theory. Arshid et al. (2020) investigated the static and dynamic behavior of functionally graded graphene-reinforced porous annular microplates based on first-order shear deformation theory. Li et al. (2020) analyzed the static and dynamic responses of porous bi-directional functionally graded plates within the first-order shear deformation theory. Kumar et al. (2021) examined the vibration frequencies of functionally graded porous nano-plates under the trigonometric shear deformation theory. Wang et al. (2022) investigated the vibration response of functionally graded circular plates modeled by the modified porous material power-law rule in the thermal environment within the first-order shear deformation theory. Kumar and Harsha (2022) analyzed the static and vibration behavior of sigmoid functionally graded piezoelectric plates with two porosity distributions under the first-order shear deformation theory. Hung et al. (2022) examined the free vibration and buckling behavior of porous micro-plates with three porosity distributions based on shear deformation theory.

Laminated composite plates can be more sensitive than conventional plates due to the disadvantages such as discontinuity between layers and weak shear strength. In addition, different orientation angles or layer stacks can also affect the structural performance of laminated composite plates. The laminated composite plates' static and dynamic responses were investigated using shear deformation theories (Reddy and Phan 1985; Fares and Zenkour 1999; Zenkour and Radwan 2016; Turan et al. 2017). Furthermore, it is necessary to analyze micro-defects and determine their effect on laminated composite plates' static and dynamic behavior. Yuan et al. (2019) analyzed the static problem of sandwich plates with three porosity distributions within first-order shear deformation theory. Xu et al. (2019) examined the influence of three different porosity distributions through the core thickness on the buckling of functionally graded porous cores sandwich plates under the shear deformation theory. Safaei (2020) studied the porosity effect on the free vibration frequencies of porous laminated composite sandwich plates based on the shear deformation theory. Esmaeilzadeh et al. (2020) examined the dynamic response of an axially moving two-layer porous laminated plate within the first-order shear deformation theory.

Porous materials are widely used today to reduce structural weight and manage vibration responses. On the other hand, laminated composites are other materials commonly used in industries such as automotive and aircraft due to their properties, such as strength/weight ratio. Accordingly, porous laminated composites are expected to be more advantageous than conventional laminated composite structures in terms of weight reduction, stiffness increase, and vibration response management. However, mechanical analyzes of such structures need to be carried out in detail. In addition, the literature review reveals that the free vibration problem of porous orthotropic two-layered plates has not yet been investigated. Therefore, this study is analyzed the natural vibration behavior of porous orthotropic layered plates. Two different porosity distributions and hyperbolic shear deformation theory are considered. The effects of porosity, shear deformation, orthotropy, layer arrangement, and geometric properties on the natural frequencies of porous orthotropic laminated plates are investigated.

2. Mathematical Model

Composite structures, known as two-layered porous structures, are produced by bonding two porous orthotropic layers to each other. In general, adopting porous composite structures can significantly reduce the system mass while maintaining the same level of stiffness. One of the most attractive applications for porous laminated composite structures is the prototype fabrication of high-speed trains. A porous orthotropic laminated composite plate with a length of edges a, b, and uniform thickness h is considered. Fig.1 presents a coordinate system $(\bar{x}, \bar{y}, \bar{z})$ in which the $(\bar{x}, \bar{y})$ plane is on the plate's mid-plane and $\bar{z}$ in the thickness direction. The angles $\theta_1, \theta_2, \ldots, \theta_N$ represents the layer orientation angle.

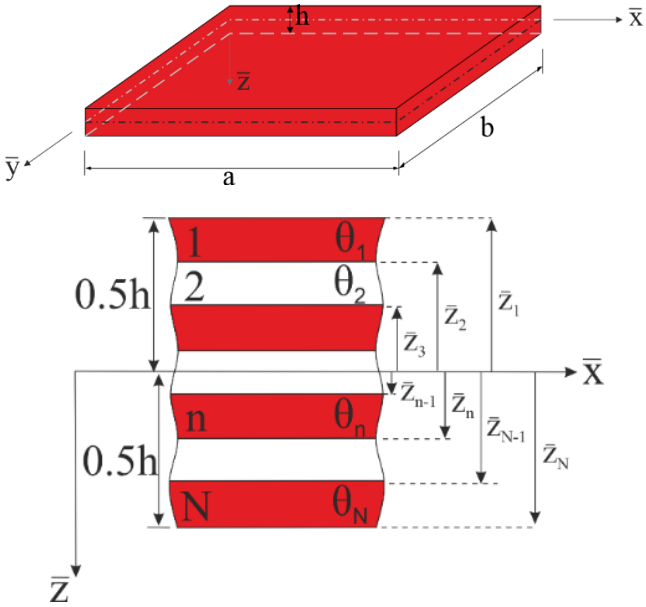

Fig. 1. Geometry, coordinate system and cross-section of a porous orthotropic laminated composite plate.

The material properties of porous materials are modeled by location's continuous function as two types of porosity model (pm). Eq. (1) determine the porous material properties.

$$El_{11}^{(n)}(z) = El_{01}^{(n)}\left(1 - kf^{(n)}(z)\right)$$

$$El_{22}^{(n)}(z) = El_{02}^{(n)}\left(1 - kf^{(n)}(z)\right)$$

$$Sh_{12}^{(n)}(z) = Sh_{012}^{(n)}\left(1 - kf^{(n)}(z)\right)$$

$$Sh_{13}^{(n)}(z) = Sh_{013}^{(n)}\left(1 - kf^{(n)}(z)\right)$$

$$Sh_{23}^{(n)}(z) = Sh_{023}^{(n)}\left(1 - kf^{(n)}(z)\right)$$

$$\rho^{(n)}(z) = \rho_0^{(n)}\left(1 - kf^{(n)}(z)\right)$$

$$n = 1,2,..,N, z = \bar{z}/h \quad (1)$$

where $El_{01}^{(n)}$ and $El_{02}^{(n)}$ are the Young's modulus of the non-porous material in the $\bar{x}$ and $\bar{y}$ directions, and $\rho_0^{(n)}$ is the mass density of the non-porous material. $Sh_{012}^{(n)}$, $Sh_{013}^{(n)}$, and $Sh_{023}^{(n)}$ are the shear modulus of the non-porous orthotropic material in the $\bar{x}\bar{y}$, $\bar{x}\bar{z}$, and $\bar{y}\bar{z}$ planes, respectively. k is the porosity coefficient and the condition $0 \leq k < 1$ is satisfied. Also, $k = 0$ corresponds to the non-porous orthotropic material (pm_1). $f^{(n)}(z)$ is the porosity distribution function of the *n*nt layer and is defined as:

$$f^{(n)}(z) = \begin{cases} \cos(\pi z), pm_2 \\ \frac{3.45}{\pi}\sin(\pi z), pm_3 \end{cases} \tag{2}$$

Fig. 2 presents the porosity models' graphical representation for the $El_{11}(z)$ function.

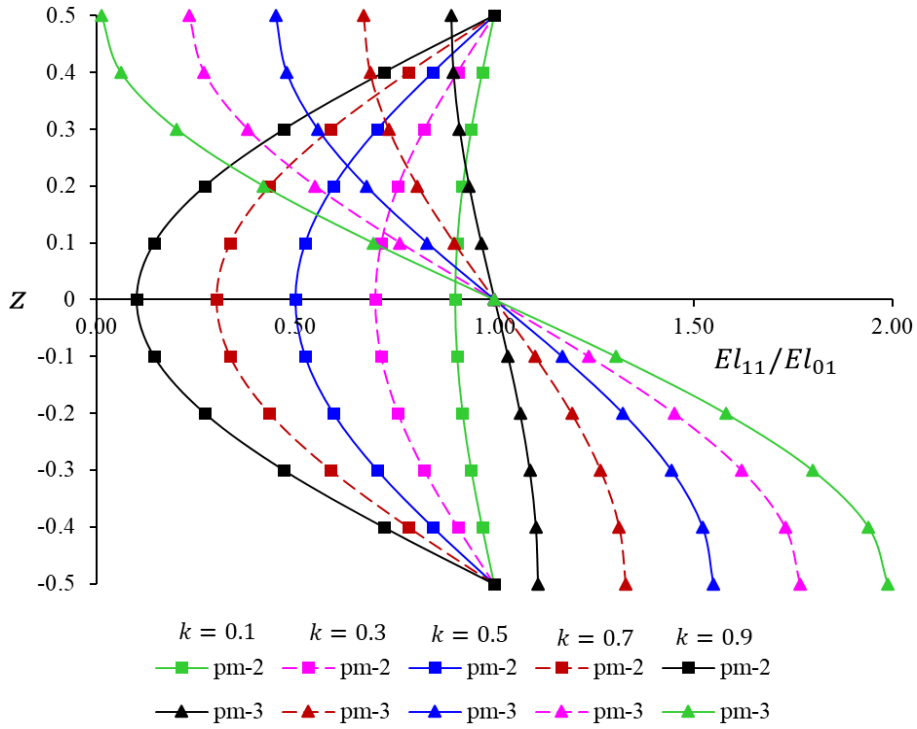

Fig. 2. Graphical representation of the porosity models for the $El_{11}(z)$ function.

3. Governing Equations

The governing equations are derived by using hyperbolical shear deformation theory in this study. The stress-strain relations of the nth porous orthotropic layer are (Reddy and Phan 1985; Fares and Zenkour 1999; Turan et al. 2017).

$$\begin{Bmatrix} \sigma_{\bar{x}} \\ \sigma_{\bar{y}} \\ \sigma_{\bar{y}\bar{z}} \\ \sigma_{\bar{x}\bar{z}} \\ \sigma_{\bar{x}\bar{y}} \end{Bmatrix}^{(n)} = \begin{bmatrix} d_{11} & d_{12} & 0 & 0 & d_{16} \\ d_{21} & d_{22} & 0 & 0 & d_{26} \\ 0 & 0 & d_{44} & d_{45} & 0 \\ 0 & 0 & d_{45} & d_{55} & 0 \\ d_{16} & d_{26} & 0 & 0 & d_{66} \end{bmatrix}^{(n)} \begin{Bmatrix} \varepsilon_{\bar{x}} \\ \varepsilon_{\bar{y}} \\ \varepsilon_{\bar{y}\bar{z}} \\ \varepsilon_{\bar{x}\bar{z}} \\ \varepsilon_{\bar{x}\bar{y}} \end{Bmatrix} \tag{3}$$

where $\varepsilon_{\bar{x}}$ and $\varepsilon_{\bar{y}}$ are strains in the $\bar{x}$ and $\bar{y}$ directions, $\varepsilon_{\bar{x}\bar{y}}$, $\varepsilon_{\bar{x}\bar{z}}$, $\varepsilon_{\bar{y}\bar{z}}$ are shear strains on the planes $\bar{x}\bar{y}$, $\bar{x}\bar{z}$, $\bar{y}\bar{z}$, respectively, and $d_{ij}^{(n)}(i,j = 1,2,..,6)$are the transformed material properties of the nth porous orthotropic layer given by (Zenkour and Radwan 2016; Turan et al. 2017)

$$d_{11} = e_{11}c^4 + e_{22}s^4 + 2(e_{12} + 2e_{66})s^2c^2, d_{12} = (e_{11} + e_{22} - 4e_{66})s^2c^2 + e_{12}(s^4 + c^4)$$

$$d_{16} = (e_{11} - e_{12} - 2e_{66})sc^3 + (e_{12} - e_{22} + 2e_{66})s^3c, d_{22} = e_{11}s^4 + e_{22}c^4 + 2(e_{12} + 2e_{66})s^2c^2$$

$$d_{26} = (e_{11} - e_{12} - 2e_{66})cs^3 + (e_{12} - e_{22} + 2e_{66})c^3s, d_{66} = (e_{11} + e_{22} - 2e_{12} - 2e_{66})c^2s^2 + e_{66}(s^4 + c^4)$$

$$d_{44} = e_{44}c^2 + e_{55}s^2, d_{45} = (e_{55} - e_{44})cs, d_{55} = e_{44}s^2 + e_{55}c^2$$

$$s = \sin\theta\,,\ c = \cos\theta \tag{4}$$

where θ is the angle between the global and local $\bar{x}$ −axes. $e_{ij}^{(n)}(i,j = 1,2,..,6)$ are the material properties of the n^{th} porous orthotropic layer defined as

$$e_{11}^{(n)}(z) = \frac{El_{11}^{(n)}(z)}{1-\upsilon_{12}^{(n)}\upsilon_{21}^{(n)}}, e_{12}^{(n)}(z) = \frac{\upsilon_{12}^{(n)}El_{22}^{(n)}(z)}{1-\upsilon_{12}^{(n)}\upsilon_{21}^{(n)}}, e_{21}^{(n)}(z) = \frac{\upsilon_{21}^{(n)}El_{11}^{(n)}(z)}{1-\upsilon_{12}^{(n)}\upsilon_{21}^{(n)}}$$

$$e_{22}^{(n)}(z) = \frac{El_{22}^{(n)}(z)}{1-\upsilon_{12}^{(n)}\upsilon_{21}^{(n)}}, e_{44}^{(n)}(z) = Sh_{23}^{(n)}(z), e_{55}^{(n)}(z) = Sh_{13}^{(n)}(z), e_{66}^{(n)}(z) = Sh_{12}^{(n)}(z)$$

$$z = \bar{z}/h, n = 1,2,..,N \tag{5}$$

where υ_{12} and υ_{21} are the Poisson ratios of the porous orthotropic layers and are assumed to be constant.

The porous orthotropic laminated composite plates' force and moment resultants based on the hyperbolical shear deformation theory are determined as:

$$\begin{aligned}
&\left(N_{\bar{x}}, N_{\bar{y}}, N_{\bar{x}\bar{y}}, M_{\bar{x}}, M_{\bar{y}}, M_{\bar{x}\bar{y}}\right) \\
&\quad = \sum_{n=1}^{N} \int_{\bar{z}_{n-1}}^{\bar{z}_n} \left(\sigma_{\bar{x}}^{(n)}, \sigma_{\bar{y}}^{(n)}, \sigma_{\bar{x}\bar{y}}^{(n)}, \bar{z}\sigma_{\bar{x}}^{(n)}, \bar{z}\sigma_{\bar{y}}^{(n)}, \bar{z}\sigma_{\bar{x}\bar{y}}^{(n)}\right) d\bar{z} \\
&\left(S_{\bar{x}}, S_{\bar{y}}, S_{\bar{x}\bar{y}}\right) \\
&\quad = \sum_{n=1}^{N} \int_{\bar{z}_{n-1}}^{\bar{z}_n} \left(\varphi(\bar{z})\sigma_{\bar{x}}^{(n)}, \varphi(\bar{z})\sigma_{\bar{y}}^{(n)}, \varphi(\bar{z})\sigma_{\bar{x}\bar{y}}^{(n)}\right) d\bar{z} \\
&\left(Q_{\bar{x}}, Q_{\bar{y}}\right) = \sum_{n=1}^{N} \int_{\bar{z}_{n-1}}^{\bar{z}_n} \left(\frac{d\varphi(\bar{z})}{d\bar{z}}\sigma_{\bar{x}\bar{z}}^{(n)}, \frac{d\varphi(\bar{z})}{d\bar{z}}\sigma_{\bar{y}\bar{z}}^{(n)}\right) d\bar{z}
\end{aligned} \tag{6}$$

where N, M, Q, and S represent force, moment, transverse shear force, and higher-order force components, respectively. Substituting Eq. (3) into Eq. (6) and then substituting the results into the virtual work principle yields

$$\begin{aligned}
&(\mathfrak{I}_{11}^0 + \mathfrak{I}_{22}^0 - 2\mathfrak{I}_{66}^0)\frac{\partial^4\gamma}{\partial\bar{x}\partial\bar{y}} + \mathfrak{I}_{21}^0\frac{\partial^4\gamma}{\partial\bar{y}^4} + \mathfrak{I}_{12}^0\frac{\partial^4\gamma}{\partial\bar{x}^4} + \mathfrak{I}_{11}^1\frac{\partial^4 w}{\partial\bar{x}^4} \\
&\quad + (\mathfrak{I}_{12}^1 + \mathfrak{I}_{21}^1 + 2\mathfrak{I}_{66}^1)\frac{\partial^4 w}{\partial\bar{x}^2\partial\bar{y}^2} + \mathfrak{I}_{22}^1\frac{\partial^4 w}{\partial\bar{y}^4} + \mathfrak{I}_{11}^2\frac{\partial^3\phi_1}{\partial\bar{x}^3} \\
&\quad + (\mathfrak{I}_{21}^2 + 2\mathfrak{I}_{66}^2)\frac{\partial^3\phi_1}{\partial\bar{x}\partial\bar{y}^2} + (\mathfrak{I}_{12}^2 + 2\mathfrak{I}_{66}^2)\frac{\partial^3\phi_2}{\partial\bar{x}^2\partial\bar{y}} + \mathfrak{I}_{22}^2\frac{\partial^3\phi_2}{\partial\bar{y}^3} \\
&\quad = \bar{\imath}_1\left(\frac{\partial^4 w}{\partial\bar{x}^2\partial t^2} + \frac{\partial^4 w}{\partial t^2\partial\bar{y}^2}\right) + \bar{\imath}_2\left(\frac{\partial^3\phi_1}{\partial\bar{x}\partial t^2} + \frac{\partial^3\phi_2}{\partial t^2\partial\bar{y}}\right) + \imath_0\frac{\partial^2 w}{\partial t^2}
\end{aligned} \tag{7a}$$

$$\begin{aligned}
&(\mathfrak{I}_{11}^3 - \mathfrak{I}_{66}^3)\frac{\partial^4\gamma}{\partial\bar{x}^2\partial\bar{y}^2} + \mathfrak{I}_{12}^3\frac{\partial^4\gamma}{\partial\bar{x}^4} + \mathfrak{I}_{11}^4\frac{\partial^4 w}{\partial\bar{x}^4} + \\
&\quad + (\mathfrak{I}_{12}^4 + \mathfrak{I}_{66}^4)\frac{\partial^4 w}{\partial\bar{x}^2\partial\bar{y}^2} + \mathfrak{I}_{11}^5\frac{\partial^3\phi_1}{\partial\bar{x}^3} + \mathfrak{I}_{66}^5\frac{\partial^3\phi_1}{\partial\bar{x}\partial\bar{y}^2} \\
&\quad + (\mathfrak{I}_{12}^5 + \mathfrak{I}_{66}^5)\frac{\partial^3\phi_2}{\partial\bar{x}^2\partial\bar{y}} - \tilde{d}_{55}^0\frac{\partial\phi_1}{\partial\bar{x}} \\
&\quad = -\bar{\imath}_2\frac{\partial^4 w}{\partial\bar{x}^2\partial t^2} + \bar{\imath}_3\frac{\partial^3\phi_1}{\partial\bar{x}\partial t^2}
\end{aligned} \tag{7b}$$

$$\begin{aligned}
&\mathfrak{I}_{21}^3\frac{\partial^4\gamma}{\partial\bar{y}^4} + (\mathfrak{I}_{22}^3 - \mathfrak{I}_{66}^3)\frac{\partial^4\gamma}{\partial\bar{x}^2\partial\bar{y}^2} + (\mathfrak{I}_{21}^4 + \mathfrak{I}_{66}^4)\frac{\partial^4 w}{\partial\bar{x}^2\partial\bar{y}^2} \\
&\quad + \mathfrak{I}_{22}^4\frac{\partial^4 w}{\partial\bar{y}^4} + (\mathfrak{I}_{21}^5 + \mathfrak{I}_{66}^5)\frac{\partial^3\phi_1}{\partial\bar{x}\partial\bar{y}^2} + \mathfrak{I}_{22}^5\frac{\partial^3\phi_2}{\partial\bar{y}^3} + \mathfrak{I}_{66}^5\frac{\partial^3\phi_2}{\partial\bar{x}^2\partial\bar{y}} \\
&\quad - \tilde{d}_{44}^0\frac{\partial\phi_2}{\partial\bar{y}} = -\bar{\imath}_2\frac{\partial^4 w}{\partial\bar{y}^2\partial t^2} + \bar{\imath}_3\frac{\partial^3\phi_2}{\partial\bar{y}\partial t^2}
\end{aligned} \tag{7c}$$

in which the terms may be found in Appendix A. $\gamma(\bar{x}, \bar{y}, t)$ is the Airy stress function. The compatibility equation for the porous orthotropic laminated composite plate can be written as

$$\begin{aligned}
&\tau_{11}^0\frac{\partial^4\gamma}{\partial\bar{y}^4} + (\tau_{12}^0 + \tau_{21}^0 + \tau_{66}^0)\frac{\partial^4\gamma}{\partial\bar{x}^2\partial\bar{y}^2} + \tau_{22}^0\frac{\partial^4\gamma}{\partial\bar{x}^4} \\
&\quad + (\tau_{11}^1 + \tau_{22}^1 - \tau_{66}^1)\frac{\partial^4 w}{\partial\bar{x}^2\partial\bar{y}^2} + \tau_{12}^1\frac{\partial^4 w}{\partial\bar{y}^4} + \tau_{21}^1\frac{\partial^4 w}{\partial\bar{x}^4} \\
&\quad + (\tau_{11}^3 - \tau_{66}^3)\frac{\partial^3\phi_1}{\partial\bar{x}\partial\bar{y}^2} + (\tau_{22}^3 - \tau_{66}^3)\frac{\partial^3\phi_2}{\partial\bar{x}^2\partial\bar{y}} + \tau_{21}^3\frac{\partial^3\phi_1}{\partial\bar{x}^3} \\
&\quad + \tau_{12}^3\frac{\partial^3\phi_2}{\partial\bar{y}^3} = 0
\end{aligned} \tag{8}$$

The porous orthotropic laminated composite plates' natural frequencies are determined with Eqs. (7) and (8).

4. Solution Procedure

Consider a simply supported porous orthotropic laminated composite plate whose boundary conditions are as follows:

$$\begin{aligned}
&v_0 = w = \phi_2 = M_{\bar{x}} = 0, \text{at } \bar{x} = 0, a \\
&u_0 = w = \phi_1 = M_{\bar{y}} = 0, \text{at } \bar{y} = 0, b
\end{aligned} \tag{9}$$

Based on the boundary conditions (9), the approximate solutions can be represented by

$$\begin{aligned}
&w(\bar{x}, \bar{y}, t) = \tilde{w}(t)\sin(\eta_1\bar{x})\sin(\eta_2\bar{y}) \\
&\phi_1(\bar{x}, \bar{y}, t) = \tilde{\phi}_1(t)\cos(\eta_1\bar{x})\sin(\eta_2\bar{y}) \\
&\phi_2(\bar{x}, \bar{y}, t) = \tilde{\phi}_2(t)\sin(\eta_1\bar{x})\cos(\eta_2\bar{y}) \\
&\eta_1 = \frac{m_1\pi}{a}, \quad \eta_2 = \frac{m_2\pi}{b}
\end{aligned} \tag{10}$$

where $\tilde{w}(t), \tilde{\phi}_1(t), \tilde{\phi}_2(t)$ are the time dependent coefficients and m_1,m_2 are the numbers of half waves.

By substituting Eq. (10) into the compatibility Eq. (8) and solving obtained equation for unknown γ leads to

$$\begin{aligned}
&\gamma(x, y, t) = \left(\tilde{w}(t)\beta_1 + \tilde{\phi}_1(t)\beta_2 + \right. \\
&\left.\tilde{\phi}_2(t)\beta_3\right)\sin(\eta_1\bar{x})\sin(\eta_2\bar{y})
\end{aligned} \tag{11}$$

with

$$\begin{aligned}
&\beta_1 = -\frac{\eta_1^4\tau_{21}^1 + \eta_1^2\eta_2^2(\tau_{11}^1 + \tau_{22}^1 - \tau_{66}^1) + \eta_2^2\tau_{12}^1}{\alpha} \\
&\beta_2 = -\frac{\eta_1\eta_2^2(\tau_{11}^3 - \tau_{66}^3) + \eta_1^3\tau_{21}^3}{\alpha} \\
&\beta_3 = -\frac{\eta_1^2\eta_2(\tau_{22}^3 - \tau_{66}^3) + \eta_1^3\tau_{12}^3}{\alpha} \\
&\alpha = \eta_1^4\tau_{22}^0 + \eta_1^2\eta_2^2(\tau_{12}^0 + \tau_{21}^0 + \tau_{66}^0) + \eta_2^4\tau_{11}^0
\end{aligned} \tag{12}$$

Replacing Eqs. (10) and (11) into Eqs. (7a), (7b), and (7c) and then applying Galerkin method to the resulting equations yields

$$\begin{aligned}
&\ell_{11}\frac{d^2\tilde{w}}{dt^2} + \ell_{12}\frac{d^2\tilde{\phi}_1}{dt^2} + \ell_{13}\frac{d^2\tilde{\phi}_2}{dt^2} + \left(\ell_{14} + \ell_{15}\tilde{\phi}_1 + \ell_{16}\tilde{\phi}_2\right)\tilde{w} \\
&\quad + \ell_{17}\tilde{\phi}_1 + \ell_{18}\tilde{\phi}_2 = 0
\end{aligned} \tag{13a}$$

$$-\ell_{21}\frac{d^2\tilde{w}}{dt^2} + \ell_{22}\frac{d^2\tilde{\phi}_1}{dt^2} + \ell_{23}\tilde{w} + \ell_{24}\tilde{\phi}_1 + \ell_{25}\tilde{\phi}_2 = 0 \tag{13b}$$

$$-\ell_{31}\frac{d^2\tilde{w}}{dt^2} + \ell_{32}\frac{d^2\tilde{\phi}_1}{dt^2} + \ell_{33}\tilde{w} + \ell_{34}\tilde{\phi}_1 + \ell_{35}\tilde{\phi}_2 = 0 \tag{13c}$$

in which the coefficients $\ell_{1i}(i = 1,2,..,8)$, $\ell_{ij}(i = 2,3; j = 1,2,.,5)$may be found in Appendix B. The inertial forces caused by the rotation angles $\tilde{\phi}_1$,$\tilde{\phi}_2$ are small so they can be ignored (i.e. $\ell_{12} = \ell_{13} = \ell_{21} = \ell_{22} = \ell_{31} = \ell_{32} = 0$) for Eqs. (13a), (13b), (13c). Eqs. (13a), (13b), (13c) can be rewritten as

$$\ell_{11}\frac{d^2\tilde{w}}{dt^2}+\left(\ell_{14}+\ell_{15}\tilde{\phi}_1+\ell_{16}\tilde{\phi}_2\right)\tilde{w}+\ell_{17}\tilde{\phi}_1+\ell_{18}\tilde{\phi}_2=0 \quad (14a)$$

$$\ell_{23}\tilde{w}+\ell_{24}\tilde{\phi}_1+\ell_{25}\tilde{\phi}_2=0 \quad (14b)$$

$$\ell_{33}\tilde{w}+\ell_{34}\tilde{\phi}_1+\ell_{35}\tilde{\phi}_2=0 \quad (14c)$$

Solving the Eqs. (14b) and (14c) with respect to $\tilde{\phi}_1$ and $\tilde{\phi}_2$ then substituting the results into the Eq. (14a) yields

$$\ell_{11}\frac{d^2\tilde{w}}{dt^2}+\tilde{\ell}_1\tilde{w}=0 \quad (15)$$

where

$$\tilde{\ell}_1=\ell_{14}+\frac{(\ell_{25}\ell_{33}-\ell_{23}\ell_{35})}{\ell_{25}(\ell_{24}\ell_{35}-\ell_{25}\ell_{34})}[\ell_{17}\ell_{25}-\ell_{18}(\ell_{23}+\ell_{24})] \quad (16)$$

The natural frequencies of a porous orthotropic laminated composite plate can be determined based on the hyperbolical shear deformation theory as:

$$\omega_{free}^{sdt}=\sqrt{\frac{\tilde{\ell}_1}{\ell_{11}}} \quad (17)$$

The natural frequencies within the classical plate theory can be determined by ignoring the shear strains in the theoretical formulations as:

$$\omega_{free}^{cpt}=\sqrt{\frac{\ell_{14}}{\ell_{11}}} \quad (18)$$

The non-dimensional natural frequencies can be determined as:

$$\bar{\omega}_{free}^{g}=\omega_{free}^{g}\left[\frac{a^2}{h}\sqrt{\rho_0/El_{02}}\right], g: sdt, cpt \quad (19)$$

5. Results and Discussion

The author focuses on the natural frequencies of two-layered plates with two porosity distributions as sinus and cosine functions. The author considers classical plate theory and hyperbolic shear deformation theory for frequency analysis. Also, the sensitivity of frequencies to porosity distributions, shear deformation, orthotropy ratio, and geometric properties are analyzed.

5.1. Verification study

This section focuses on comparing and verifying the obtained equations with the results available in the literature. As a first comparison, the current study's natural frequencies are compared with those in Reddy and Phan (1985). The results are presented in Table 1. The material and geometric properties of the non-porous orthotropic laminated plate are as follows:

$El_{01}=40El_{02},\ Sh_{023}=0.5El_{02},\ Sh_{012}=Sh_{013}=0.6El_{02},\ \upsilon_{012}=0.25, \frac{a}{b}=1,\ k=0$

Table 1 illustrates that the present study's results are consistent with the literature.

Table 1. Dimensionless natural frequencies, $\bar{\omega}_{\text{free}}^{g}(g: sdt, cpt)$, of non-porous orthotropic laminated composite plates.

Reddy and Phan (1985)				
	$0^o/90^o/90^o/0^o$		$0^o/90^o$	
a/h	*cpt*	*sdt*	*cpt*	*sdt*
12.5	18.707	16.276	11.066	10.686
25	18.780	18.050	11.139	11.037
50	18.799	17.606	11.158	11.132
Present study				
a/h	*cpt*	*sdt*	*cpt*	*sdt*
12.5	18.793	16.141	11.249	10.852
25	18.867	18.063	11.294	11.190
50	18.885	18.673	11.305	11.279

In the second comparison, the orthotropy ratio-dependent natural frequencies of layered plates are compared with those in Fares and Zenkour (1999). Table 2 shows the obtained results. The material and geometric properties of the considered non-porous orthotropic laminate are as follows: $El_{01}/El_{02}=open, Sh_{023}=0.5El_{02}, Sh_{012}=Sh_{013}=0.6El_{02}, \upsilon_{012}=0.25, a/b=1, a/h=5, k=0$. Table 2 shows that the current study's results are in good agreement with the literature.

Table 2. Dimensionless natural frequencies, $\tilde{\omega}_{\text{free}}^{sdt}=\omega_{\text{free}}^{sdt}h\sqrt{\rho_0 El_{02}}$, of non-porous orthotropic laminated composite plates.

El_{01}/El_{02}	Fares and Zenkour (1999)	Present study
3	0.2576	0.2593
10	0.3229	0.3212
20	0.3670	0.3631
30	0.3920	0.3869

5.2. Natural frequency analysis

This section involves the natural frequencies of two-layered plates with two different porosity models within the classical plate and shear deformation theories. The considered material properties of two-layered plates are given by: $El_{01}=137.9GPa,\ El_{02}=8.96GPa,\ Sh_{012}=Sh_{013}=7.10GPa,\ Sh_{023}=6.21GPa,\ \upsilon_{012}=0.3, \rho_0=1450kg.m^{-3}$.

Table 3 shows the variation of natural frequencies of two-layered plates with/without porosity (pm_3/pm_1). The considered parameters for analysis are given as $a/h=10, a/b=0.5, m=n=1$ and $k=0.4, 0.6$ and 0.8. The dimensionless natural frequencies of the non-porous/porous two-layered plates increase with the rising El_{01}/El_{02} ratio. The dimensionless natural frequencies of the porous single- and $90^o/0^o$ -layered plates decrease depending on the increase in the k coefficient. At the same time, the $0^o/90^o$-layered plates' natural frequencies diminish in $El_{01}/El_{02}\leq 25$ and rise in $El_{01}/El_{02}>25$.

Table 3. Dimensionless natural frequencies, $\bar{\omega}^{g}_{\text{free}}(g: sdt, cpt)$, of pm_1 and pm_3 model orthotropic laminated composite plates versus orthotropy ratio for three different layer sequences.

		0^o				$0^o/90^o$				$90^o/0^o$			
		pm_1		pm_3		pm_1		pm_3		pm_1		pm_3	
k	El_{01}/El_{02}	*cpt*	*sdt*	*cpt*	*sdt*	*cpt*	*sdt*	*cpt*	*sdt*	*cpt*	*sdt*	*cpt*	*sdt*
0.4	5	7.001	6.782	6.663	6.474	4.951	4.876	4.719	4.656	4.951	4.876	4.836	4.763
	15	11.373	10.439	10.824	10.012	6.008	5.883	5.970	5.854	6.008	5.883	5.783	5.663
	25	14.480	12.655	13.781	12.186	6.854	6.675	6.977	6.801	6.854	6.675	6.483	6.320
	35	17.030	14.235	16.208	13.752	7.599	7.361	7.853	7.607	7.599	7.361	7.094	6.886
	45	19.245	15.443	18.316	14.960	8.274	7.974	8.639	8.317	8.274	7.974	7.649	7.394
0.6	5	7.001	6.782	6.214	6.061	4.951	4.876	4.481	4.428	4.951	4.876	4.591	4.527
	15	11.373	10.439	10.094	9.430	6.008	5.883	5.870	5.764	6.008	5.883	5.495	5.388
	25	14.480	12.655	12.852	11.536	6.854	6.675	6.970	6.800	6.854	6.675	6.116	5.973
	35	17.030	14.235	15.115	13.075	7.599	7.361	7.915	7.670	7.599	7.361	6.649	6.469
	45	19.245	15.443	17.081	14.277	8.274	7.974	8.757	8.430	8.274	7.974	7.130	6.913
0.8	5	7.001	6.782	5.522	5.415	4.951	4.876	4.146	4.106	4.951	4.876	4.133	4.085
	15	11.373	10.439	8.970	8.499	6.008	5.883	5.708	5.614	6.008	5.883	4.960	4.878
	25	14.480	12.655	11.421	10.477	6.854	6.675	6.911	6.749	6.854	6.675	5.474	5.366
	35	17.030	14.235	13.432	11.954	7.599	7.361	7.929	7.688	7.599	7.361	5.898	5.765
	45	19.245	15.443	15.179	13.129	8.274	7.974	8.828	8.500	8.274	7.974	6.276	6.119

The non-porous laminated plates' frequencies are more significant than the porous ones for single- and $90^o/0^o$-layered plates. In contrast, they are less than the porous ones for $0^o/90^o$-layered plates in $El_{01}/El_{02} > 15$. With a rising orthotropy ratio, the natural frequency value difference between porous and non-porous laminated plates increases for single- and $90^o/0^o$-layered plates. It first decreases and then increases for $0^o/90^o$-layered plates. It rises depending on the increase in the k coefficient for all layer sequences. The non-porous/porous two-layered plates' natural frequencies are less than that of the non-porous/porous single-layered plates. The difference in natural frequency value between non-porous/porous single- and two-layered plates increases due to the rise of the orthotropy ratio. It diminishes with increasing the k coefficient. Suppose fiber orientation angles of two-layered plates are compared. In that case, the natural frequency values of non-porous two-layered plates are the same. However, the porous $0^o/90^o$-layered plates' natural frequency values are more significant than those of the porous $90^o/0^o$-layered plates in $El_{01}/El_{02} > 5$. The natural frequency value difference between porous two-layered plates increases with a rising in orthotropy ratio and k coefficient.

The influence of shear deformation on the natural frequencies of non-porous/porous laminated plates increases with a rising in the orthotropy ratio. With increasing El_{01}/El_{02} ratio from 5 to 45 at $k = 0.4$, the shear deformation effect on the natural frequencies of porous $0^o/90^o$ -layered plates rises from (1.3%) to (3.7%). The effect of shear deformation on the porous laminated plates' natural frequencies diminishes with an increase in porosity coefficient. The shear deformation effect on the natural frequencies of porous single-layered plates decreases from (18.3%) to (13.5%) with rising k from 0.4 to 0.8 at $El_{01}/El_{02} = 45$. The shear deformation effect on the natural frequencies of porous laminated plates is less than those of non-porous laminated plates. The shear deformation effect difference between the non-porous and porous two-layered plates is less than (1%) for increasing k and El_{01}/El_{02}. In contrast, the shear deformation effect difference between the non-porous and porous single-layered plates increases with rising k and El_{01}/El_{02}. It increases from (1.4%) to (6.3%) depending on the rise in k from 0.4 to 0.8 at $El_{01}/El_{02} = 45$. The shear deformation effect on the natural frequencies of non-porous/porous single-layered plates is more significant than two-layered plates' frequencies. The difference in shear deformation effect between non-porous single- and two-layered plates increases (15%) with increasing El_{01}/El_{02} from 5 to 45. The shear deformation effect difference between porous single- and two-layered plates decreases depending on the increase of k. With rising in k from 0.4 to 0.8 at $El_{01}/El_{02} = 45$, it diminishes from (14.6%) to (9.8%) for $0^o/90^o$-layer sequence. If fiber orientation angles of two-layered plates are compared, the shear deformation effect on the natural frequency of non-porous two-layered plates is the same. At the same time, the influence of shear deformation on the porous $90^o/0^o$ -layered plates' natural frequency is less than those of the porous $0^o/90^o$-layered plates in the range of $El_{01}/El_{02} > 15$. The shear deformation effect difference between porous two-layered plates increases with a rising k. This increase is less than (1%).

Due to the increase in the El_{01}/El_{02} ratio, the effect of the porosity model on the natural frequencies of porous single-layered plates diminishes for sdt and remains constant for cpt. At the same time, the porosity model effect on the natural frequencies increases for $90^o/0^o$, while it first decreases and then rises for $0^o/90^o$. With rising El_{01}/El_{02} from 5 to 45 at $k = 0.8$, the effect of the porosity model on the porous $0^o/90^o$-layered plates' natural frequencies diminishes first (11%) and then increases (6%).

The influence of the porosity model on the natural frequencies of porous laminated plates rises with increasing k coefficient for all layer sequences. The porosity model effect on the natural frequencies of $90^o/0^o$-layered plates increases (17%) with rising k from 0.4 to 0.8 when $El_{01}/El_{02} = 45$. The influence of the porosity model on the single-layered plates' natural frequencies is more significant than that of the $0^o/90^o$-layered plates. However, it is less than that of the $90^o/0^o$-layered plates in the range of $El_{01}/El_{02} > 25$. Due to the rise in the El_{01}/El_{02} ratio, the difference in the porosity model effect between the porous single- and two-layered plates increases first and then diminishes for the $0^o/90^o$-layer sequence. On the contrary, it decreases first and then rises for the $90^o/0^o$-layer sequence. Depending on the increase in El_{01}/El_{02} from 5 to 45 at $k = 0.8$ for sdt, the porosity model effect difference between the single- and $90^o/0^o$-layered plates diminishes first by (2.5%) and then rises by (6.8%).

The difference in the porosity model effect between the porous single- and two-layered plates increases with the rising k coefficient. The porosity model effect difference between the single- and $0^o/90^o$-layered plates increases from (1.8%) to (16.1%) with rising k from 0.4 to 0.8 at $El_{01}/El_{02} = 25$ for sdt. When two-layered plates' fiber orientation angles are compared, the influence of the porosity model on the natural frequencies of porous $0^o/90^o$-layered plates is less than that of $90^o/0^o$-layered plates in the range of $El_{01}/El_{02} > 5$. The porosity model effect difference between porous two-layered plates increases with a rise in k in the range of $El_{01}/El_{02} > 5$. It rises around (14%) for cpt and sdt due to the increase of k from 0.4 to 0.8 at $El_{01}/El_{02} = 45$. The difference in porosity model effect between porous two-layered plates rises first and then diminishes depending on the increase in the El_{01}/El_{02} ratio. It increases first by (19%) and then decreases by (2%) depending on the rise of El_{01}/El_{02} from 5 to 45 at $k = 0.8$ for sdt.

Fig. 3 presents the variation of natural frequencies of non-porous/porous two-layered plates. The selected parameters for analysis are given as $a/h = 10, m = n = 1$ and $k = 0.4, 0.6, 0.8$. The non-dimensional natural frequencies of the two-layered plates with/without porosity (pm_2/pm_1) rise with the increasing aspect ratio (a/b). The dimensionless natural frequencies of the porous single- and two-layered plates increase depending on the increase in the k coefficient. The porous laminated plates' natural frequencies are more significant than non-porous laminated plate ones. The natural frequency value difference between non-porous and porous laminated plates increases with the rise in aspect ratio and porosity coefficient for single-layered plates. It increases with increasing aspect ratio and porosity coefficient in the range of $a/b < 2.75$ for two-layered plates. The natural frequencies of non-porous/porous two-layered plates are less than those of non-porous/porous single-layered plates in $a/b < 1.75$. The natural frequency value difference between the single- and two-layered plates firstly diminishes and then increases with the rising aspect ratio. It increases depending on the rise of the porosity coefficient.

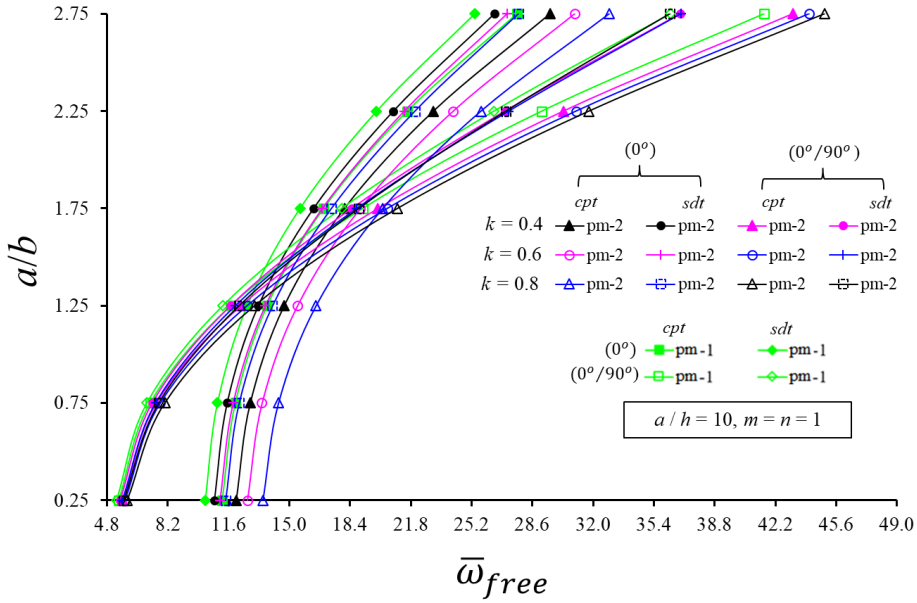

Fig. 3. Variation of the natural frequencies of porous orthotropic two-layered plate versus a/b and k for three different layer sequences.

Due to an increase in aspect ratio, the influence of shear deformation on the natural frequencies rises for two-layered plates. At the same time, it decreases first and then increases for single-layered plates. The shear deformation effect on the natural frequencies of non-porous two-layered plates increases by (11%) depending on the rise in a/b from 0.25 to 2.75. The effect of shear deformation on natural frequencies of porous two-layered plates rises with an increasing porosity coefficient. The shear deformation effect on the porous two-layered plates' natural frequencies increases from (14.6%) to (19.3%) with the rise in k from 0.4 to 0.8 at $a/b = 2.75$. The influence of shear deformation on the non-porous/porous single-layered plates' natural frequencies is more significant than that of non-porous/porous two-layered plates in $a/b < 2.25$. The difference in shear deformation effect between the non-porous/porous single- and two-layered plates firstly diminishes and then rises with increasing aspect ratio. The shear deformation effect difference between the non-porous single- and two-layered plates firstly decreases by (5%) and then increases by (2.7%) due to a rise in a/b from 0.25 to 2.75. The difference in shear deformation effect between the porous single- and two-layered plates increases with rising porosity coefficient (for $a/b < 2.25$). The shear deformation effect difference between the porous single- and two-layered plates rises from (7.9%) to (12.1%) with a rise in k from 0.4 to 0.8.

Depending on the increase in aspect ratio, the porosity model effect on the natural frequencies of porous laminated plates firstly increases and then decreases for two-layered plates. At the same time, it diminishes for single-layered plates. With rising a/b from 0.25 to 2.75 at $k = 0.8$ for sdt, the influence of the porosity model on the natural frequencies of porous two-layered plates firstly increases by (2%) and then decreases by (9.3%). The effect of the porosity model on the natural frequencies of porous laminated plates increases with the rise in the k coefficient. With increasing k from 0.4 to 0.8 at $a/b = 0.25$, the porosity model effect on the natural frequencies of porous single-layered plates rises (13%) and (6%) for cpt and sdt, respectively. The porosity model effect on the natural frequencies of porous two-layered plates is less than that of porous single-layered. The difference in porosity model effect between the porous single- and two-layered plates increases first and then decreases with increasing aspect ratio. Due to the rise in a/b from 0.25 to 2.75 at $k = 0.8$, the porosity model effect difference between the porous single- and two-layered plates firstly increases by (1.9%) and then decreases by (2.2%) for cpt. At the same time, it rises first (2%) and then diminishes (8.2%) for sdt. The difference in the porosity model effect between the porous single- and two-layered plates increases with the rising k. The porosity model effect difference between the porous single- and two-layered plates increases around (9%) with an increase in k from 0.4 to 0.8 at $a/b = 2.75$.

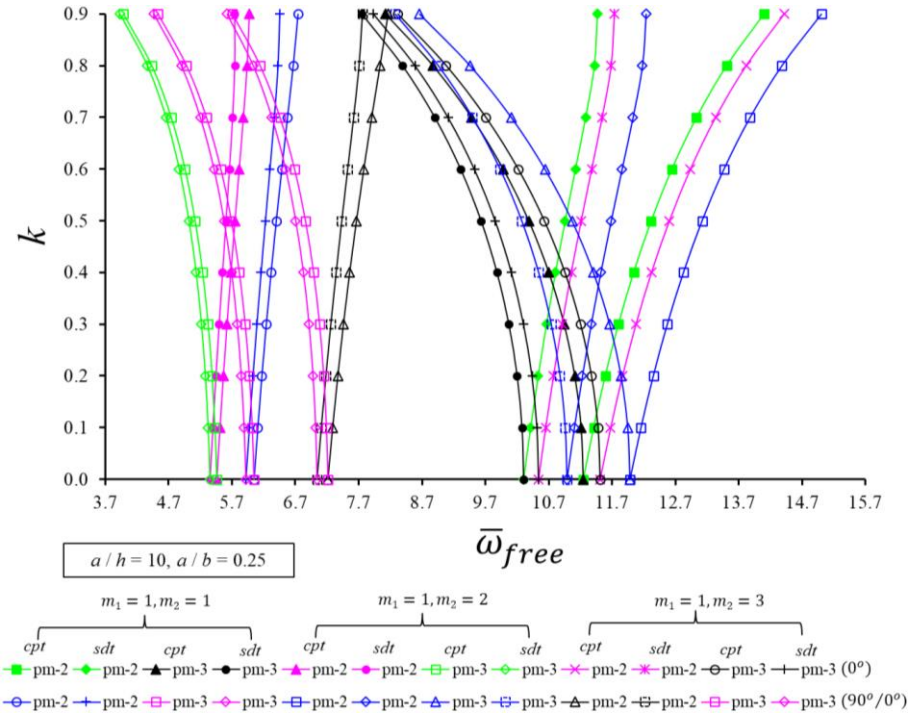

Fig. 4. Variation of the natural frequencies of porous orthotropic two-layered plate versus k and m_2 for different porosity models.

Fig. 4 illustrates the variation of natural frequencies of porous laminated plates depending on the k coefficient and wavenumbers. The considered parameters for analysis are given by $a/h = 10, a/b = 0.25$ and $m_2 = 1, 2, 3$. The dimensionless natural frequencies of the porous laminated plates increase for the pm_2 model and decrease for the pm_3 model with a rising k coefficient. The porous laminated plates' non-dimensional natural frequencies increase due to the rise in wavenumbers. The pm_3 model single- and two-layered plates' natural

frequencies are less than those of the pm_2 model ones in $k > 0$. The natural frequency value difference between the pm_2 and pm_3 models laminated plates rises with increasing k and m_2. The natural frequencies of porous single-layered plates are more significant than those of two-layered ones. Due to the rise in the k coefficient, the difference in natural frequency value between single- and two-layered plates diminishes for the pm_3 model and increases for the pm_2 model. At the same time, it decreases for pm_2 and pm_3 models with increasing m_2.

Depending on the rise in the k coefficient, the effect of shear deformation on the porous laminated plates' natural frequencies increases for the pm_2 model and decreases for the pm_3 model. Due to increasing k from 0 to 0.9 at $m_2 = 3$, the variations of shear deformation effect on single-layered plates' frequencies are (10%) and (4%) for pm_2 and pm_3 models, respectively. With increasing m_2, the influence of shear deformation on the natural frequencies of porous laminated plates diminishes for porous single-layered plates and rises for porous two-layered plates. The variations of shear deformation effect on two-layered plates' frequencies are less than (1.5%) depending on the rising m_2 from 1 to 3. The shear deformation effect on the pm_3 model laminated plates' natural frequencies is less than that of the pm_2 model ones. The difference in shear deformation effect between the pm_2 and pm_3 model laminated plates is more significant for porous single-layered plates. The shear deformation effect difference between the pm_2 and pm_3 model laminated plates increases with the rising k coefficient. Due to increasing k from 0 to 0.9 at $m_2 = 3$, it rises (14%) and (3.5%) for single- and two-layered plates, respectively. Depending on the increasing m_2, the difference in shear deformation effect between the pm_2 and pm_3 model laminated plates decreases for single-layered plates and rises for two-layered plates. The difference variation is around (1%) for both porous laminated plates due to the rise in m_2 from 1 to 3 at $k = 0.9$. The influence of shear deformation on the natural frequencies of the porous single-layered plates is more significant than those of porous two-layered plates. The shear deformation effect difference between the porous single- and two-layered plates decreases with increasing m_2. At the same time, it diminishes for pm_3 model and rises for pm_2 model with rising k. It rises from (6%) to (14%) depending on the increase in k from 0 to 0.9 at $m_2 = 3$. Also, its variation is less than (1.5%) depending on the rising m_2 from 1 to 3 at $k = 0.9$.

The effect of the porosity model on the porous laminated plates' natural frequencies increases depending on the rise in the k coefficient. With increasing k from 0 to 0.9 at $m_2 = 2$ for single-layered plates in sdt, it rises (11.3%) and (24.8%) for pm_2 and pm_3 models, respectively. The porosity model effect on natural frequencies of porous laminated plates decreases with rising m_2 for single-layered plates. At the same time, it increases for the pm_2 model and diminishes for pm_3 with increasing m_2 in two-layered plates. With rising m_2 from 1 to 3 at $k = 0.9$ for porous two-layered plates in sdt, the porosity model effect increases by (2.8%) and decreases by (6.3%) for the pm_2 and pm_3 models, respectively. The pm_3 model effect on the laminated plates' natural frequencies is more significant than the pm_2 model ones in the range of $k > 0.4$ for sdt. The porosity model effect difference between the pm_2 and pm_3 models increases for rising k and decreases for increasing m_2. The difference in the porosity model effect between the pm_2 and pm_3 model two-layered plates increases (15.4%) with rising k from 0 to 0.9 at $m_2 = 2$ for sdt. It diminishes (9.1%) with rising m_2 from 1 to 3 at $k = 0.9$ for sdt. The pm_2 model effect on the porous single-layered plates' natural frequencies is more significant than that of two-layered ones. However, the pm_3 model effect on the porous single-layered plates' natural frequencies is less than that of two-layered ones in $k < 0.4$ and $k < 0.5$ for cpt and sdt, respectively. The difference in the porosity model effect between the porous single- and two-layered plates increases with rising k. At the same time, it diminishes for the pm_2 model and increases for the pm_3 model with the rise in m_2. With rising k from 0 to 0.9 at $m_2 = 3$ for sdt, the porosity model effect difference between the single- and two-layered plates increases (1.3%) and (4.5%) for pm_2 and pm_3 models, respectively. Its variation depending on the increase in m_2 from 1 to 3 at $k = 0.9$ for sdt is (2.8%) in pm_2 and pm_3 models.

6. Conclusions

Porous materials, widely used to reduce structural weight and manage vibration responses, and laminated composites, used in the aircraft and aerospace industries due to their superior properties, are combined in this study. The effects of this combination on the free vibration response of the porous laminated plates were emphasized by comparing them with the classical or non-porous laminated plates. This paper analyzes the natural frequencies of two-layered composite plates with two different porosity distributions within the higher-order shear deformation theory. The influences of porosity models, shear deformation, and geometric parameters on porous two-layered composite plates are discussed in detail. The notable results are as follows:

- The dimensionless natural frequencies of the pm_3 model single- and $90^o/0^o$ -layered plates decrease with the rising k coefficient. The non-dimensional natural frequencies of the pm_2 model $0^o/90^o$ - and $90^o/0^o$-layered plates increase with increasing k coefficient.
- The natural frequencies of non-porous $0^o/90^o$ -layered plates are less than those of the porous ones, and the non-porous $90^o/0^o$ -layered plates' natural frequencies are more significant than those of the porous ones.
- The pm_3 model laminated plates' natural frequencies are less than those of the pm_2 model ones.
- The influence of shear deformation on the natural frequencies of porous two-layered plates increases for the pm_2 model and decreases for the pm_3 model depending on the rise in the k coefficient.
- The shear deformation effect on the natural frequencies of porous laminated plates is less than those of non-porous ones.

- The shear deformation effect on the natural frequencies of porous single-layered plates is more significant than two-layered plates' frequencies.
- The shear deformation effect on the pm_3 model laminated plates' natural frequencies is less than that of the pm_2 model ones.
- The porosity model effect on the natural frequencies of porous two-layered plates rises with increasing k coefficient.
- The pm_2 and pm_3 (for $k > 0.4$) model effect on the porous single-layered plates' natural frequencies is more significant than that of $0^o/90^o$-layered ones for sdt.

Appendix A.

$$\Im_{11}^0 = \tilde{d}_{11}^1\tau_{11}^0 + \tilde{d}_{12}^1\tau_{21}^0, \Im_{12}^0 = \tilde{d}_{11}^1\tau_{12}^0 + \tilde{d}_{12}^1\tau_{22}^0, \Im_{21}^0 = \tilde{d}_{21}^1\tau_{11}^0 + \tilde{d}_{22}^1\tau_{21}^0, \Im_{22}^0 = \tilde{d}_{21}^1\tau_{12}^0 + \tilde{d}_{22}^1\tau_{22}^0,$$

$$\Im_{11}^1 = \tilde{d}_{11}^1\tau_{11}^1 + \tilde{d}_{12}^1\tau_{21}^1 - \tilde{d}_{11}^2, \Im_{12}^1 = \tilde{d}_{11}^1\tau_{12}^1 + \tilde{d}_{12}^1\tau_{22}^1 - \tilde{d}_{12}^2, \Im_{21}^1 = \tilde{d}_{21}^1\tau_{11}^1 + \tilde{d}_{22}^1\tau_{21}^1 - \tilde{d}_{21}^2,$$

$$\Im_{22}^1 = \tilde{d}_{21}^1\tau_{12}^1 + \tilde{d}_{22}^1\tau_{22}^1 - \tilde{d}_{22}^2, \Im_{11}^2 = \tilde{d}_{11}^1\tau_{11}^3 + \tilde{d}_{12}^1\tau_{21}^3 + \tilde{d}_{11}^4, \Im_{12}^2 = \tilde{d}_{11}^1\tau_{12}^3 + \tilde{d}_{12}^1\tau_{22}^3 + \tilde{d}_{12}^4,$$

$$\Im_{21}^2 = \tilde{d}_{21}^1\tau_{11}^3 + \tilde{d}_{22}^1\tau_{21}^3 + \tilde{d}_{21}^4, \Im_{22}^2 = \tilde{d}_{21}^1\tau_{12}^3 + \tilde{d}_{22}^1\tau_{22}^3 + \tilde{d}_{22}^4, \Im_{11}^3 = \tilde{d}_{11}^3\tau_{11}^0 + \tilde{d}_{12}^3\tau_{21}^0,$$

$$\Im_{12}^3 = \tilde{d}_{11}^3\tau_{12}^0 + \tilde{d}_{12}^3\tau_{22}^0, \Im_{21}^3 = \tilde{d}_{21}^3\tau_{11}^0 + \tilde{d}_{22}^3\tau_{21}^0, \Im_{22}^3 = \tilde{d}_{21}^3\tau_{12}^0 + \tilde{d}_{22}^3\tau_{22}^0, \Im_{11}^4 = \tilde{d}_{11}^3\tau_{11}^1 + \tilde{d}_{12}^3\tau_{21}^1 - \tilde{d}_{11}^4,$$

$$\Im_{12}^4 = \tilde{d}_{11}^3\tau_{12}^1 + \tilde{d}_{12}^3\tau_{22}^1 - \tilde{d}_{12}^4, \Im_{21}^4 = \tilde{d}_{21}^3\tau_{11}^1 + \tilde{d}_{22}^3\tau_{21}^1 - \tilde{d}_{21}^4, \Im_{22}^4 = \tilde{d}_{21}^3\tau_{12}^1 + \tilde{d}_{22}^3\tau_{22}^1 - \tilde{d}_{22}^4,$$

$$\Im_{11}^5 = \tilde{d}_{11}^3\tau_{11}^3 + \tilde{d}_{12}^3\tau_{21}^3 + \tilde{d}_{11}^5, \Im_{12}^5 = \tilde{d}_{11}^3\tau_{12}^3 + \tilde{d}_{12}^3\tau_{22}^3 + \tilde{d}_{12}^5, \Im_{21}^5 = \tilde{d}_{21}^3\tau_{11}^3 + \tilde{d}_{22}^3\tau_{21}^3 + \tilde{d}_{21}^5,$$

$$\Im_{22}^5 = \tilde{d}_{21}^3\tau_{12}^3 + \tilde{d}_{22}^3\tau_{22}^3 + \tilde{d}_{22}^5, \Im_{66}^0 = \tilde{d}_{66}^1\tau_{66}^0, \Im_{66}^1 = \tilde{d}_{66}^1\tau_{66}^1 - 2\tilde{d}_{66}^2, \Im_{66}^2 = \tilde{d}_{66}^1\tau_{66}^3 + \tilde{d}_{66}^4, \Im_{66}^3 = \tilde{d}_{66}^3\tau_{66}^0,$$

$$\Im_{66}^4 = \tilde{d}_{66}^3\tau_{66}^1 - 2\tilde{d}_{66}^4, \Im_{66}^5 = \tilde{d}_{66}^3\tau_{66}^3 + \tilde{d}_{66}^5 \quad \text{(A1)}$$

with

$$\tau_{11}^0 = \frac{\tilde{d}_{22}^0}{\tilde{\Delta}}, \tau_{12}^0 = \frac{-\tilde{d}_{12}^0}{\tilde{\Delta}}, \tau_{21}^0 = \frac{-\tilde{d}_{21}^0}{\tilde{\Delta}}, \tau_{22}^0 = \frac{\tilde{d}_{11}^0}{\tilde{\Delta}},$$

$$\tau_{11}^1 = \frac{\tilde{d}_{22}^0\tilde{d}_{11}^1 - \tilde{d}_{12}^0\tilde{d}_{21}^1}{\tilde{\Delta}}, \tau_{12}^1 = \frac{\tilde{d}_{22}^0\tilde{d}_{12}^1 - \tilde{d}_{12}^0\tilde{d}_{22}^1}{\tilde{\Delta}},$$

$$\tau_{21}^1 = \frac{\tilde{d}_{11}^0\tilde{d}_{21}^1 - \tilde{d}_{21}^0\tilde{d}_{11}^1}{\tilde{\Delta}}, \tau_{22}^1 = \frac{\tilde{d}_{11}^0\tilde{d}_{22}^1 - \tilde{d}_{21}^0\tilde{d}_{12}^1}{\tilde{\Delta}},$$

$$\tau_{11}^3 = \frac{\tilde{d}_{12}^0\tilde{d}_{21}^3 - \tilde{d}_{22}^0\tilde{d}_{11}^3}{\tilde{\Delta}}, \tau_{12}^3 = \frac{\tilde{d}_{12}^0\tilde{d}_{22}^3 - \tilde{d}_{22}^0\tilde{d}_{12}^3}{\tilde{\Delta}},$$

$$\tau_{21}^3 = \frac{\tilde{d}_{21}^0\tilde{d}_{11}^3 - \tilde{d}_{11}^0\tilde{d}_{21}^3}{\tilde{\Delta}}, \tau_{22}^3 = \frac{\tilde{d}_{21}^0\tilde{d}_{12}^3 - \tilde{d}_{11}^0\tilde{d}_{22}^3}{\tilde{\Delta}},$$

$$\tau_{66}^0 = \frac{1}{\tilde{d}_{66}^0}, \tau_{66}^1 = \frac{2\tilde{d}_{66}^1}{\tilde{d}_{66}^0}, \tau_{66}^3 = \frac{-\tilde{d}_{66}^3}{\tilde{d}_{66}^0}, \tilde{\Delta} = \tilde{d}_{11}^0\tilde{d}_{22}^0 - \tilde{d}_{12}^0\tilde{d}_{21}^0,$$

$$\tilde{d}_{ij}^\ell = \sum_{n=1}^N \int_{\bar{z}_{n-1}}^{\bar{z}_n} (\bar{z})^\ell d_{ij}^{(n)} d\bar{z},$$

$$\tilde{d}_{ij}^{\ell+3} = \sum_{n=1}^N \int_{\bar{z}_{n-1}}^{\bar{z}_n} (\bar{z})^{2\ell-\ell^2} \varphi(\bar{z})^{0.5(\ell^2-\ell+2)} d_{ij}^{(n)} d\bar{z}, i, j = 1,2,6; \ell = 0,1,2,$$

$$\tilde{d}_{ij}^0 = \sum_{n=1}^N \int_{\bar{z}_{n-1}}^{\bar{z}_n} \left(\frac{d\varphi(\bar{z})}{d\bar{z}}\right)^2 d_{ij}^{(n)} d\bar{z}, i, j = 4,5 \quad \text{(A2)}$$

with

$$\bar{\iota}_1 = \frac{\iota_1^2}{\iota_0} - \iota_2, \bar{\iota}_2 = \iota_4 - \frac{\iota_1\iota_3}{\iota_0}, \bar{\iota}_3 = \iota_5 - \frac{\iota_3^2}{\iota_0},$$

$$(\iota_0, \iota_1, \iota_2, \iota_3, \iota_4, \iota_5) = \sum_{n=1}^N \int_{\bar{z}_{n-1}}^{\bar{z}_n} \rho(\bar{z})(1, \bar{z}, \bar{z}^2, \varphi(\bar{z}), \bar{z}\varphi(\bar{z}), \varphi(\bar{z})^2) d\bar{z} \quad \text{(A3)}$$

Appendix B.

$$\ell_{11} = \frac{ab(\bar{\iota}_1(\eta_1^2+\eta_2^2)-\iota_0)}{4}, \ \ell_{12} = \frac{ab\eta_1\bar{\iota}_2}{4}, \ \ell_{13} = \frac{ab\eta_2\bar{\iota}_2}{4},$$

$$\ell_{14} = \frac{ab}{4}[\eta_1^4(r_4 + r_3\beta_1) + \eta_1^2\eta_2^2(r_5 + r_1\beta_1) + \eta_2^4(r_6 + r_2\beta_1)],$$

$$\ell_{15} = \frac{8\eta_1\eta_2\beta_2}{3}, \ \ell_{16} = \frac{8\eta_1\eta_2\beta_3}{3},$$

$$\ell_{17} = \frac{ab}{4}[(\eta_1^4 r_3 + \eta_1^2\eta_2^2 r_1 + \eta_2^4 r_2)\beta_2 + \eta_1(\eta_1^2 r_7 + \eta_2^2 r_8)],$$

$$\ell_{18} = \frac{ab}{4}[(\eta_1^4 r_3 + \eta_1^2\eta_2^2 r_1 + \eta_2^4 r_2)\beta_3 + \eta_2(\eta_1^2 r_9 + \eta_2^2 r_{10}),$$

$$\ell_{21} = \eta_1^2\bar{\iota}_2\frac{ab}{4}, \ \ell_{22} = \eta_1\bar{\iota}_3\frac{ab}{4},$$

$$\ell_{23} = \frac{ab}{4}[\eta_1^4(r_{13} + r_{12}\beta_1) + \eta_1^2\eta_2^2(r_{14} + r_{11}\beta_1)],$$

$$\ell_{24} = \frac{ab}{4}[(\eta_1^4 r_{12} + \eta_1^2\eta_2^2 r_{11})\beta_2 + \eta_1(\eta_1^2 r_{15} + \eta_2^2 r_{16} + r_{18})],$$

$$\ell_{25} = \frac{ab}{4}[(\eta_1^4 r_{12} + \eta_1^2\eta_2^2 r_{11})\beta_3 + \eta_1^2\eta_2 r_{17}],$$

$$\ell_{31} = \eta_2^2\bar{\iota}_2\frac{ab}{4}, \ \ell_{32} = \eta_2\bar{\iota}_3\frac{ab}{4},$$

$$\ell_{33} = \frac{ab}{4}[\eta_1^2\eta_2^2(r_{21} + r_{20}\beta_1) + \eta_2^4(r_{22} + r_{19}\beta_1)],$$

$$\ell_{34} = \frac{ab}{4}[(\eta_1^2\eta_2^2 r_{20} + \eta_2^4 r_{19})\beta_2 + \eta_1\eta_2^2 r_{23}],$$

$$\ell_{35} = \frac{ab}{4}[(\eta_1^2\eta_2^2 r_{20} + \eta_2^4 r_{19})\beta_3 + \eta_2(\eta_1^2 r_{25} + \eta_2^2 r_{24} + r_{26})] \quad \text{(B1)}$$

with

$$r_1 = \Im_{11}^0 + \Im_{22}^0 - 2\Im_{66}^0, \ r_2 = \Im_{21}^0, \ r_3 = \Im_{12}^0, \ r_4 = \Im_{11}^1,$$

$$r_5 = \Im_{12}^1 + \Im_{21}^1 + 2\Im_{66}^1,\ r_6 = \Im_{22}^1,\ r_7 = \Im_{11}^2,$$

$$r_8 = \Im_{21}^2 + 2\Im_{66}^2,\ r_9 = \Im_{12}^2 + 2\Im_{66}^2,$$

$$r_{10} = \Im_{22}^2,\ r_{11} = \Im_{11}^3 - \Im_{66}^3,\ r_{12} = \Im_{12}^3,\ r_{13} = \Im_{11}^4,$$

$$r_{14} = \Im_{12}^4 + \Im_{66}^4,\ r_{15} = \Im_{11}^5,\ r_{16} = \Im_{66}^5,\ r_{17} = \Im_{12}^5 + \Im_{66}^5,$$

$$r_{18} = \tilde{d}_{55}^0,\ r_{19} = \Im_{21}^3,\ r_{20} = \Im_{22}^3 - \Im_{66}^3,\ r_{21} = \Im_{21}^4 + \Im_{66}^4,$$

$$r_{22} = \Im_{22}^4,\ r_{23} = \Im_{21}^5 + \Im_{66}^5,\ r_{24} = \Im_{22}^5,$$

$$r_{25} = \Im_{66}^5,\ r_{26} = \tilde{d}_{44}^0 \qquad \text{(B2)}$$

Acknowledgements

None declared.

Funding

The author received no financial support for the research, authorship, and/or publication of this manuscript.

Conflict of Interest

The author declared no potential conflicts of interest with respect to the research, authorship, and/or publication of this manuscript.

References

Arshid E, Amir S, Loghman A (2020). Static and dynamic analyses of FG-GNPs reinforced porous nanocomposite annular micro-plates based on MSGT. *International Journal of Mechanical Sciences*, 180, 105656.

Aydogdu M (2009). A new shear deformation theory for laminated composite plates. *Composite Structures*, 89(1), 94-101.

Chen Z, Qin B, Zhong R, Wang Q (2022). Free in-plane vibration analysis of elastically restrained functionally graded porous plates with porosity distributions in the thickness and in-plane directions. *The European Physical Journal Plus*, 137(1), 1-21.

Esen I, Özmen R (2022). Thermal vibration and buckling of magneto-electro-elastic functionally graded porous nanoplates using nonlocal strain gradient elasticity. *Composite Structures*, 296, 115878.

Esmaeilzadeh M, Kadkhodayan M, Mohammadi S, Turvey GJ (2020). Nonlinear dynamic analysis of moving bilayer plates resting on elastic foundations. *Applied Mathematics and Mechanics (English Edition)*, 41(3), 439-458.

Fares M, Zenkour A (1999). Buckling and free vibration of non-homogeneous composite cross-ply laminated plates with various plate theories. *Composite Structures*, 44(4), 279-287.

Hung P, Phung-Van P, Thai CH (2022). A refined isogeometric plate analysis of porous metal foam microplates using modified strain gradient theory. *Composite Structures*, 289, 115467.

Kumar P, Harsha SP (2022). Static and vibration response analysis of sigmoid function-based functionally graded piezoelectric non-uniform porous plate. *Journal of Intelligent Material Systems and Structures*, 1045389X221077433.

Kumar Y, Gupta A, Tounsi A (2021). Size-dependent vibration response of porous graded nanostructure with FEM and nonlocal continuum model. *Advances in Nano Research*, 11(1), 1-17.

Lahdiri A, Kadri M (2022). Free vibration behaviour of multi-directional functionally graded imperfect plates using 3D isogeometric approach. *Earthquakes and Structures*, 22(5), 527-538.

Li S, Zheng S, Chen D (2020). Porosity-dependent isogeometric analysis of bi-directional functionally graded plates. *Thin-Walled Structures*, 156, 106999.

Mahi A, Adda Bedia EA, Tounsi A (2015). A new hyperbolic shear deformation theory for bending and free vibration analysis of isotropic, functionally graded, sandwich and laminated composite plates. *Applied Mathematical Modelling*, 39(9), 2489-2508.

Pan H-G, Wu Y-S, Zhou J-N, Fu Y-M, Liang X, Zhao T-Y (2021). Free vibration analysis of a graphene-reinforced porous composite plate with different boundary conditions. *Materials*, 14(14), 3879.

Pham Q-H, Nguyen P-C, Tran V-K, Nguyen-Thoi T (2021). Finite element analysis for functionally graded porous nano-plates resting on elastic foundation. *Steel and Composite Structures*, 41(2), 149-166.

Reddy JN, Phan ND (1985). Stability and vibration of isotropic, orthotropic and laminated plates according to a higher-order shear deformation theory. *Journal of Sound and Vibration*, 98(2), 157-170.

Safaei B, (2020). The effect of embedding a porous core on the free vibration behavior of laminated composite plates. *Steel and Composite Structures*, 35(5), 659-670.

Shi P, Dong C, Sun F, Liu W, Hu Q (2018). A new higher order shear deformation theory for static, vibration and buckling responses of laminated plates with the isogeometric analysis. *Composite Structures*, 204 342-358.

Teng Z, Xi P (2021). Analysis on free vibration and critical buckling load of a FGM porous rectangular plate. *Xibei Gongye Daxue Xuebao/Journal of Northwestern Polytechnical University*. 39(2), 317-325.

Turan F, Başoğlu MF, Zerin Z (2017). Analytical solution for bending and buckling response of laminated non-homogeneous plates using a simplified-higher order theory. *Challenge Journal of Structural Mechanics*, 3(1), 1-16.

Wang W, Xue G, Teng Z (2022). Analysis of free vibration characteristics of porous FGM circular plates in a temperature field. *Journal of Vibration Engineering & Technologies*, 1-12.

Xu K, Yuan Y, Li M (2019). Buckling behavior of functionally graded porous plates integrated with laminated composite faces sheets. *Steel and Composite Structures*, 32(5), 633-642.

Yuan Y, Zhao K, Xu K (2019). Enhancing the static behavior of laminated composite plates using a porous layer. *Structural Engineering and Mechanics*, 72(6), 763-774.

Zenkour AM, Radwan AF (2016). Free vibration analysis of multilayered composite and soft core sandwich plates resting on Winkler–Pasternak foundations. *Journal of Sandwich Structures & Materials*, 20(2), 169-190.

Zhong R, Qin B, Wang Q, Shao W, Shuai C (2021). Prediction of the in-plane vibration behavior of porous annular plate with porosity distributions in the thickness and radial directions. *Mechanics of Advanced Materials and Structures*, 1-25.

Zhou C, Zhan Z, Zhang J, Fang Y, Tahouneh V (2020). Vibration analysis of FG porous rectangular plates reinforced by graphene platelets. *Steel and Composite Structures*, 34(2), 215-226.

Challenge Journal of Structural Mechanics

Research Article

Optimum parameters for adjacent structures coupled by fluid viscous dampers considering soil–structure interaction

Oğuz Akın Düzgün [a,*], Yavuz Selim Hatipoğlu [b], Osman Ünsal Bayrak [a]

[a] *Department of Civil Engineering, Atatürk University, 25240 Erzurum, Türkiye*
[b] *Department of Civil Engineering, Bayburt University, 69000 Bayburt, Türkiye*

ABSTRACT

In this paper, the optimum conditions which ensure that the resulting minimum base shear force and minimum roof displacement for two adjacent frame structures interconnected by fluid viscous dampers, including soil-structure interaction (SSI) effects under seismic excitation were presented. A two-dimensional (2D) finite element analysis was carried out with the Taguchi method. As non-reflecting boundaries, viscous boundary conditions were used on the edges of finite soil region. An optimization study was carried out for four parameters such as soil type, height ratio of the frames, damping coefficient of viscous damper, and the location of the viscous damper each with four levels. The optimum conditions which minimize maximum roof displacements and the maximum base shear forces have been obtained. The most affecting parameter on the system response was found to be soil type. It was also found that the sufficient damping coefficient of the viscous damper is equal to $1x10^5$ N.s/m for minimum response. The minimum system response can be achieved by using only one damper. It can be drawn that the Taguchi method can be used with the finite element (FE) method for determining optimum conditions of a soil-structure system for minimum system response.

ARTICLE INFO

Article history:
Received 12 September 2022
Revised 31 October 2022
Accepted 18 November 2022

Keywords:
Adjacent frames
Fluid viscous dampers
Soil-structure interaction
Optimum conditions
Taguchi method

1. Introduction

Vibrations due to several reasons like earthquake excitations, machine foundations, heavy traffic, blasting, or strong wind can cause damage to structures and annoyance to residents. The effect of such vibrations can be mitigated or prevented by implementing vibration control systems in structures. The main purpose of such systems is to provide additional damping to the structures by either transmitting it directly to any connected structure or converting energy to heat (Bhaskarao and Jangid 2006a; Patel and Jangid 2014). Coupling neighboring structures with suitable energy dissipation devices is an effective and practical approach to get some advantages such as avoiding pounding and response reduction (Bhaskarao and Jangid 2006a; Bharti et al. 2010). Vibration control systems may be divided into four categories such as active, passive, semi-active, and hybrid systems according to their energy consumption (Housner et al. 1997; Zhu et al. 2001). However, employing passive energy absorbers is the most common way of adding damping to structures when considering their simplicity in design, operation, and maintenance (Bakre and Jangid 2007; Patel and Jangid 2014). There are various types of passive energy-absorbing devices. One of them is viscous dampers. A typical viscous damper is usually composed of a piston in the damper housing filled with viscous material in the form of either solid (rubber or acrylics) or fluid (silicone or oil). One of the viscous damper types is fluid viscous dampers. In a fluid viscous damper, the energy is dispersed by the movement of the piston in the viscous fluid. It is considered that the output force of the viscous damper is in direct proportion to the velocity of the piston (Makris and Constantinou 1990; Housner et al. 1997; Patel and Jangid 2014).

* *Corresponding author*. Tel.: +90-442-231-4771 ; Fax: +90-442-231-4910 ; E-mail address: oaduzgun@atauni.edu.tr (O. A. Düzgün)
ISSN: 2149-8024 / DOI: https://doi.org/10.20528/cjsmec.2023.01.002

Numerous studies have been carried out on the dynamic response of adjacent structures interconnected by different energy-dissipating devices. Westermo (1989), one of the pioneering works on the subject, examined the effectiveness of hinged links for adjacent structures to avoid pounding damages. The effectiveness of viscous dampers on the system response of adjacent coupled structures under dynamic excitation was studied by Luco and De Barros (1998), Xu et al. (1999), Bhaskararao and Jangid (2007), Cimellaro and Garcia (2007), Tubaldi et al. (2014), Tubaldi (2015), Wu et al. (2017), and De Domenico et al. (2019). These studies indicated that response reduction and avoiding mutual pounding can be achieved by coupling adjacent structures with viscous dampers. In addition, the number and location of the dampers affect the dynamic behavior of coupled structures. Apart from these issues, optimum locations of dampers for response mitigation (Luco and De Barros 1998; Bhaskararao and Jangid 2006b; De Domenico et al. 2019), optimum damping coefficient of damper (Xu et al. 1999; Zhu and Xu 2005; Bhaskararao and Jangid 2007; Wu et al. 2017; De Domenico et al. 2019), and effective damping coefficient of fluid viscous dampers (FVDs) for dynamic response mitigation (Düzgün and Hatipoğlu 2022) were also studied. It is well known that considering the mechanical properties of soil medium in the modeling and analysis is considerably affected the dynamic behavior of structures. However, studies on coupled adjacent buildings that considering soil-structure interaction (SSI) are quite limited. The effects of geotechnical properties of soil on the dynamic response of adjacent buildings interconnected by dampers were studied by Patel and Jangid (2008), Zou et al. (2012), and Avinash et al. (2017). In these studies, the problem was handled in a simplified manner probably due to the complexity of the problem. It is clear that there is a need to conduct more studies on the dynamic response of coupled adjacent buildings including SSI effects to get a better understanding of the effects of the soil medium on coupled system response.

In the conventional design of experiments, increasing the number of variables leads to increasing the number of experiments. Hence, more material, money, time, and personnel are necessary for the conventional experiment design. Therefore, researchers have tried to develop methods to reduce the number of experiments without any data loss. The Taguchi method is a statistical method developed by Taguchi (1960) to investigate the effects of different parameters on determining the optimum operating conditions of any process. Optimization of the process is carried out with the design of the experiment tool using an orthogonal array, which is formed according to parameters and their levels. This method computes the optimum conditions according to the analysis of variance using obtained data. However, the optimum condition is a point estimation. Therefore, the result of the optimum condition should be controlled with an error ratio whether it is in a certain confidence interval. Moreover, the most effective parameter or the influence rank of the parameters can be determined by the Taguchi method too (Bayrak and Hınıslıoğlu 2017).

The goal of this study is to determine the parameters such as soil type, height ratio of the structures, damping coefficient of damper, and the location of the damper which ensure that the resulting minimum base shear force and minimum roof displacement for two adjacent multi-story frame structures interconnected by FVDs, including SSI effects under earthquake excitation by finite element (FE) method. Viscous boundary conditions were used as special non-reflecting boundaries on the edges of finite soil region. Since the dynamic response of the system is affected by many factors and different solutions, the FE analyses were carried out with the Taguchi method which is a special design of experiment. As a result of the study, the optimum conditions were determined for the minimum roof displacements and minimum base shear forces of the coupled structures-soil system.

2. The Taguchi Method

The Taguchi method is a mighty tool to use to investigate the effects of different parameters on determining the optimum conditions of any process. In this method, more information can be obtained by using lesser data (Taguchi 1960). An orthogonal array technique was used in order to design the finite element analyses (FEA) (Taguchi 1960). Factors and their levels that affect the roof displacements and the base shear forces of two adjacent structures were decided according to the former studies on the subject. The selected factors and their levels given in Table 1 were used in the FEA according to the L_{16} orthogonal array which is recommended by Taguchi (1960) for four factors each has four levels (Table 2) (Taguchi 1960; Bayrak and Hınıslıoğlu 2017).

Table 1. Factors and their levels used for FEA.

Factors	Levels			
	1	2	3	4
(A) Soil Type	-	I	II	III
(B) H_B/H_A Ratio	1.00	1.50	1.75	2.00
(C) Damping Coefficient (Ns/m)	1×10^4	1×10^5	1×10^6	1×10^7
(D) Number of Damper	1 FVD	3 FVD	6 FVD	12 FVD

Table 2. L_{16} orthogonal array.

FEA No	Soil Type	H_B/H_A Ratio	Damping Coefficient	Number of Damper
1	1	1	1	1
2	1	2	2	2
3	1	3	3	3
4	1	4	4	4
5	2	1	2	3
6	2	2	1	4
7	2	3	4	1
8	2	4	3	2
9	3	1	3	4
10	3	2	4	3
11	3	3	1	2
12	3	4	2	1
13	4	1	4	2
14	4	2	3	1
15	4	3	2	4
16	4	4	1	3

The numbers shown in Table 2 are the levels of each factor. The analysis order was arbitrarily chosen to minimize the noise sources that affect the results in a negative way (Taguchi 1960; Bayrak and Hınıslıoğlu 2017). The obtained roof displacements and base shear forces were calculated based on the quality characteristic of 'smaller the better' using Eq. (1):

$$\frac{S}{N} = -10\log_{10}\left(\frac{1}{n}\sum_{i=1}^{n} Y_i^2\right) \quad (1)$$

where S/N (signal to noise ratio, unit: dB) are performance statistics, Y_i is a performance value of the i^{th} analysis, and n is the number of repeated analysis.

The optimum conditions can be obtained by the levels of factors that maximize the average S/N values. However, in the Taguchi method, the levels of factors indicating optimum conditions may not be found in L_{16} orthogonal array (Table 2) (Bayrak and Hınıslıoğlu 2017). In such cases, the prediction of the S/N value for optimum conditions can be calculated by Eq. (2) according to the L_{16} orthogonal array.

$$Y_i = \mu + X_i + e_i \quad (2)$$

where X_i, μ, and e_i are the fixed effect of the factor level combination used in the i^{th} analysis, the overall mean of the performance value, and the random error in the i^{th} analysis, respectively (Taguchi 1960). Because of Eq. (2) is a point estimation, the confidence interval must be evaluated. The confidence interval at the chosen error level may be calculated by using Eq. (3).

$$\mu \pm \sqrt{F_{\alpha,1,DF_{MSe}}\left[\left(\frac{1+m}{N}\right)+\left(\frac{1}{n_i}\right)\right]} \quad (3)$$

where α, F, DF_{MSe}, N, m, and n_i are the error level, the value of the F table, degrees of freedom of mean square error, the number of total analyses, degrees of freedom used in the prediction of Y_i, and the number of repeated analysis, respectively.

3. Numerical Modeling of Coupled System

First of all, some assumptions and limitations were considered in order to make the problem governable. Two adjacent structures were assumed to be symmetric frames with their symmetric planes in alignment. Possible torsional effects due to linked viscous dampers between two structures were neglected. Assuming the ground excitation occurred in one dimension in the plane of the structures, the problem can be handled as a two-dimensional (2D) problem. The adjacent frame structures were idealized as linear shear-type structures with lateral degrees of freedom at their floor levels. The adjacent structures system was assumed to remain in the linear elastic stage under ground motion due to a considerable increase in energy-absorbing capacity. It was also assumed that the floors of each frame were at the same level where two neighboring floors were connected with fluid viscous dampers. However, the number of stories in each structure can be different. Each viscous damper was modeled as a linear dashpot direct proportional to the relative velocity between the two adjacent floors. Both adjacent structures were assumed to be subjected to the same seismic excitation and the effects due to SSI were considered. The soil was assumed to be homogeneous, linear-elastic, and isotropic medium.

The coupled structures-soil model presented in this study is schematically shown in Fig. 1. Structure A and

Structure B were assumed that have n stories and n + m stories, respectively. The mass, damping coefficient and lateral stiffness values for i^{th} story are $m_{i,A}$, $c_{i,A}$, and $k_{i,A}$ for Structure A and $m_{i,B}$, $c_{i,B}$, and $k_{i,B}$ for Structure B, respectively. The damping coefficient of the viscous damper at i^{th} floor is $c_{d,i}$. The governing equations of motion of the interconnected structures system can be expressed in the matrix form as (Xu et al. 1999; Zhang and Xu 1999):

$$\mathbf{M}\ddot{\mathrm{U}} + (\mathbf{C} + \mathbf{C_D})\dot{\mathrm{U}} + (\mathbf{K} + \mathbf{K_D})\mathrm{U} = -\mathbf{M}\,\mathbf{I}\,\ddot{\mathrm{u}}_g \tag{4}$$

where, M, C and K are the mass, damping and stiffness matrices of the system, respectively. K_D and C_D represent the additional damping and stiffness matrices due to the installation of the FVDs, respectively. The corresponding equations of motions, when the two adjacent buildings are connected with viscous dampers, can simply be obtained by making K_D equal to null matrix in the Eq. (4) (Bhaskararao and Jangid 2004). U is the relative displacement vector with respect to the ground motion; I is a vector with all elements equal to 1, and $\ddot{u}_g$ is the applied ground motion acceleration. The details of each matrix were given in (Xu et al. 1999; Zhang and Xu 1999; Bhaskararao and Jangid 2004).

A number of dynamic analyses were carried out by the finite element-based software ANSYS (2021) according to the L_{16} orthogonal array presented in Table 2. The direct approach which enables the solving of the coupling frames system and the soil in a single step was employed. The columns and beams of the frames were modeled with BEAM189 element (ANSYS 2021) which is a quadratic three-node beam element. The structural elements were idealized as the linear-elastic materials with Rayleigh damping. The damping ratio (ξ) of structures is assumed to be 0.05 (Ada and Ayvaz 2019). Rayleigh damping is a linear combination of the mass and stiffness matrices, and it can be calculated by the following equation:

$$\mathbf{C} = \alpha[\mathbf{M}] + \beta[\mathbf{K}] \tag{5}$$

where α and β are the damping coefficients with units $1/s$ and s, respectively. If the damping coefficients are not known, assuming the i^{th} and j^{th} modes have the same damping ratio (ξ), the coefficient can be calculated by the following equation:

$$\begin{Bmatrix}\alpha\\ \beta\end{Bmatrix} = \frac{2\xi}{\omega_i+\omega_j}\begin{Bmatrix}\omega_i\omega_j\\ 1\end{Bmatrix} \tag{6}$$

where ω_i and ω_j are the angular frequencies of the i^{th} and j^{th} modes, respectively.

The soil environment assumed to be a homogeneous, isotropic, and linear-elastic material was modeled with PLANE182 element (ANSYS 2021) which is a four-node plane element with three degrees of freedom at each node. In order to provide energy transmitting in boundaries, viscous boundary conditions were defined at the edges of finite soil medium by using COMBIN14 element (ANSYS 2021) in both vertical and horizontal directions. Viscous boundary conditions were used as non-reflecting boundaries on the edges of finite soil zone.

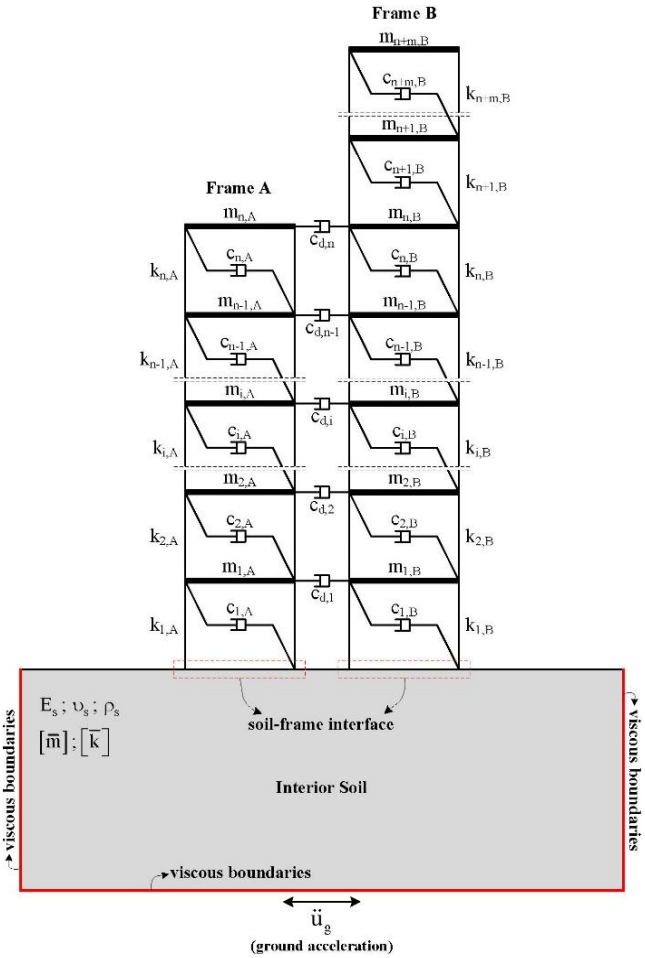

Fig. 1. Schematic representation of adjacent structures-soil system (Düzgün and Hatipoğlu 2022).

The non-reflecting viscous boundaries was first introduced by Lysmer and Kuhlemeyer (1969). Since its implementation involves placing viscous dashpots at the boundary, it is also often referred to as the viscous boundary. Viscous boundary method appears to treat both dilatational and shear waves with sufficient accuracy in many applications. The viscous forces, or dashpots, do not depend upon the frequencies of the transmitted waves. It can absorb harmonic and non- harmonic waves. Viscous boundaries are local in space and time; therefore, this technique is suitable for transient analysis (Wolf 1988).

Fluid viscous dampers, as an energy dissipating device, were used for avoiding pounding and response reduction in adjacent frames. The linear damper behavior can be expressed by

$$F_T = F_D + F_E = CV^{c.exp} + KD_k \tag{7}$$

where, F_T, V, C, K, and D_k are total force provided by the damper, velocity across the damper, the damping coefficient, the spring constant, and displacement across the spring, respectively. The damping exponent expressed by *c.exp* and it must be positive. In the literature, the practical range of the damping exponent is between 0.3 and 2 (Tezcan and Uluca 2003; Hou 2008; Uz 2009). In this study, since the fluid viscous dampers were taken as

linear, the damping exponent was assumed equal to 1. F_T consists of two parts as shown in Eq. (7). The first part is the damping force F_D and the second part is restoring force F_E. In the lack of stiffness, the force in the fluid viscous damper can be expressed by

$$F_D = CV^{c.exp}\text{sgn}(V) \quad (8)$$

where, sgn is the signum function. Then, the function defines the sign of the relative velocity term (Hou 2008). The verification of the model was presented in Düzgün and Hatipoğlu (2022).

4. Parametric Studies

In the soil-adjacent structures system, the mass density, modulus of the elasticity, and Poisson ratio of the adjacent structures were assumed to be ρ_{str}=2500 kg/m^3, E_{str}=30000 MPa, and υ=0.20, respectively. The mean story-to-story spacing was 3 m. It was assumed that the height of Structure A (H_A) was constant as 36 meters (12-story) while the height of Structure B (H_B) was selected proportional to H_A. The H_B/H_A ratios used in this study can be seen in Table 1. On the other hand, the column and beam dimensions of both frames were the same for each story with the column dimensions of 0.5x0.5 m, and the beam dimensions of 0.3x0.6 m. The damping ratio of both adjacent frames was taken constant as 5%. The mass and shear stiffness of both frames were uniform for each story with the mass of 1.124x10^4 kg, and the shear stiffness of 2.1x10^8 N/m. Fluid viscous dampers were used to connect two adjacent floors. Four different damper connection scenarios are taken based on the number of dampers as can be seen in Table 1. The damper connection scenarios are shown in Fig. 2. The selected damping coefficients for the dampers are also shown in Table 1.

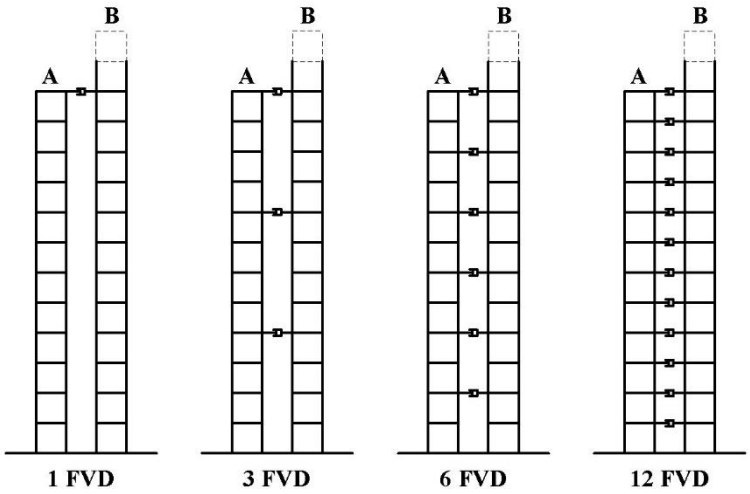

Fig. 2. Fluid viscous damper connection scenarios.

It is noted that no relative displacement was allowed at the soil-frame interface in all simulations. The dimensions of finite soil region were selected as 210 m. in width and 90 m. in depth. In order to obtain dynamic response of adjacent structures-soil system, three different soil types were considered by the name of Soil Type I Soil Type II and Soil Type III. These soil types represent dense, medium, and loose soil characteristics, respectively. The selected mechanical properties of all soil types are presented in Table 3. The mechanical properties of all soil types were adopted from the study conducted by Çelebi et al. (2012). The mechanical properties of selected soil types represent the general properties of the loose, medium, and dense soils instead of representing a specific soil material to determine how to affect soil medium the dynamic response of adjacent frames.

Kocaeli, Turkey (1999) earthquake (PGA = 0.34g) was chosen for acceleration data of the ground motion acting horizontally at the bottom edge of the soil layer. The ground motion time history is shown in Fig. 3. A numerical procedure was used to evaluate the system response in the analyses. The finite elements and boundary conditions mentioned earlier were used in the numerical treatment.

Table 3. Mechanical properties of soil types.

Soil Type	I	II	III
Modulus of Elasticity (E) (MPa)	6000	400	35
Poisson Ratio (υ)	0.30	0.30	0.25
Mass Density (ρ) (kg/m^3)	2100	1900	1700
Shear Wave Velocity (v_s) (m/sec)	1029	285	91
Pressure Wave Velocity (v_p) (m/sec)	2141	532	157

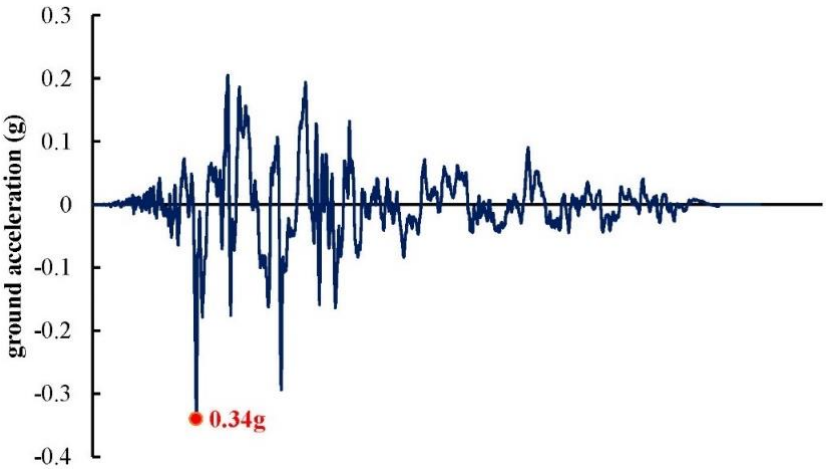

Fig. 3. Input ground motion time history.

5. Results and Discussion

According to the factors and levels (Tables 1 and 2), the optimum conditions were determined for the minimum roof displacements and minimum base shear forces of the coupled structures-soil system by using the Taguchi method. The results were presented separately for the Structures A and B. The S/N values were calculated by using Eq. (1) according to the FE analysis results given in Table 4. The optimum conditions for the minimum response are obtained by average S/N effects which can be calculated from the S/N values.

Table 4. The S/N values, roof displacement and base shear force values of both frames.

	Performance Statistics (S/N)							
	Structure A				Structure B			
	Roof Displacements		Base Shear Forces		Roof Displacements		Base Shear Forces	
FEA No	S/N	m	S/N	kN	S/N	m	S/N	kN
1	20.193	0.0978	-45.251	183.04	20.193	0.0978	-45.251	183.04
2	22.225	0.0774	-43.495	149.53	17.380	0.1352	-43.236	145.14
3	20.336	0.0962	-44.366	165.31	14.789	0.1822	-42.985	141.01
4	15.274	0.1723	-47.064	225.53	8.232	0.3876	-46.940	222.34
5	21.190	0.0872	-44.899	175.78	21.577	0.0834	-50.447	332.92
6	20.193	0.0978	-44.674	171.28	15.815	0.1619	-45.351	185.16
7	17.822	0.1285	-45.350	185.13	12.822	0.2285	-46.008	199.70
8	17.247	0.1373	-45.978	199.02	9.042	0.3531	-44.975	177.32
9	11.434	0.2681	-51.995	397.89	11.444	0.2678	-52.895	441.33
10	13.073	0.2220	-48.671	271.37	9.704	0.3272	-48.974	280.99
11	10.958	0.2832	-51.412	372.06	6.630	0.4661	-51.157	361.28
12	14.600	0.1862	-48.102	254.15	8.702	0.3672	-47.143	227.59
13	10.377	0.3028	-46.836	219.69	10.377	0.3028	-47.744	243.88
14	10.308	0.3052	-45.829	195.63	6.335	0.4822	-45.618	190.95
15	10.288	0.3059	-46.844	219.89	3.129	0.6975	-44.869	175.17
16	7.004	0.4465	-47.344	232.91	-4.420	1.6634	-49.591	301.69
Average	15.158		-46.757		10.734		-47.074	

Table 5. The average S/N effects for roof displacements of Structure A.

Factors	Levels			
	1	2	3	4
(A) Soil Type	19.507	19.113	12.516	9.494
(B) H_B/H_A Ratio	15.799	16.450	14.851	13.531
(C) Damping Coefficient	14.587	17.076	14.831	14.137
(D) Number of Damper	15.731	15.202	15.401	14.297

Table 6. The average S/N effects for roof displacements of Structure B.

Factors	Levels			
	1	2	3	4
(A) Soil Type	15.149	14.814	9.120	3.855
(B) H_B/H_A Ratio	15.898	12.309	9.343	5.389
(C) Damping Coefficient	9.555	12.697	10.403	10.284
(D) Number of Damper	12.013	10.857	10.284	9.655

Table 7. The average S/N effects for base shear forces of Structure A.

Factors	Levels			
	1	2	3	4
(A) Soil Type	-45.044	-45.225	-50.045	-46.713
(B) H_B/H_A Ratio	-47.245	-45.667	-46.993	-47.122
(C) Damping Coefficient	-47.170	-45.835	-47.042	-46.980
(D) Number of Damper	-46.133	-46.930	-46.320	-47.644

Table 8. The average S/N effects for base shear forces of Structure B.

Factors	Levels			
	1	2	3	4
(A) Soil Type	-44.603	-46.695	-50.042	-46.956
(B) H_B/H_A Ratio	-49.084	-45.795	-46.255	-47.162
(C) Damping Coefficient	-47.838	-46.424	-46.618	-47.417
(D) Number of Damper	-46.005	-46.778	-47.999	-47.514

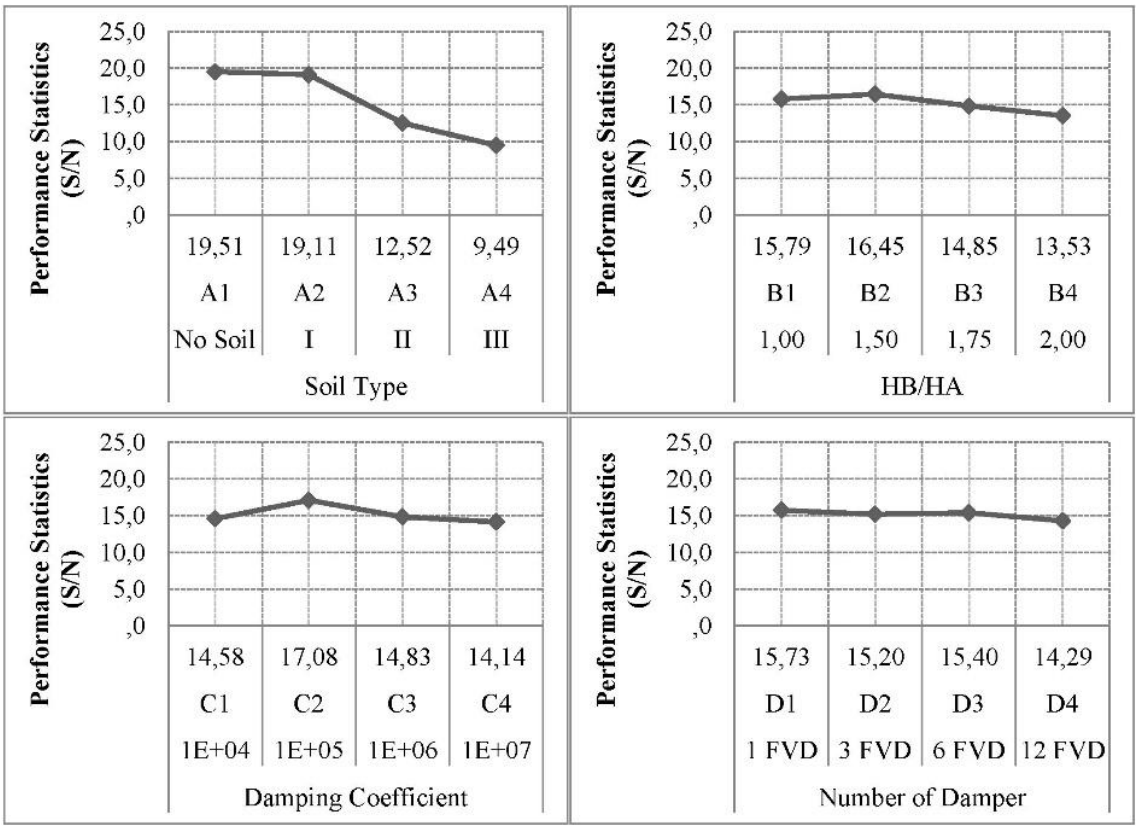

Fig. 4. The effects of parameters on roof displacements for Structure A.

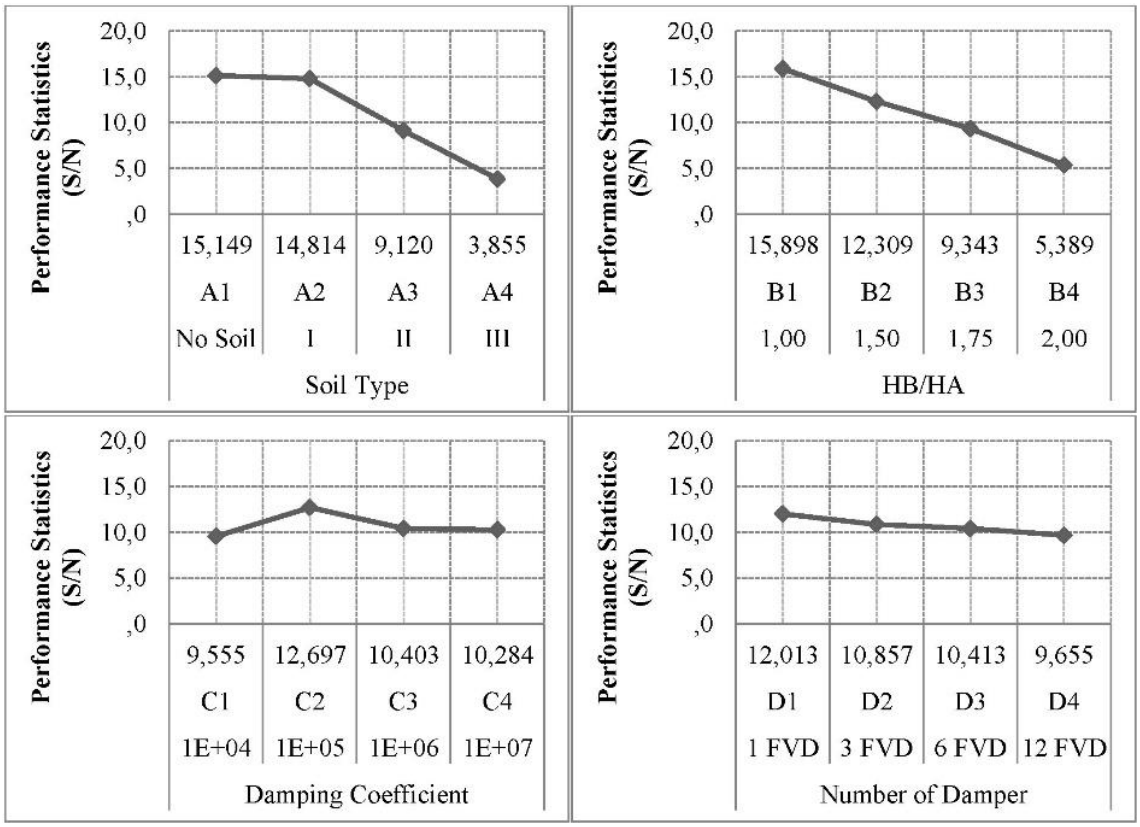

Fig. 5. The effects of parameters on roof displacements for Structure B.

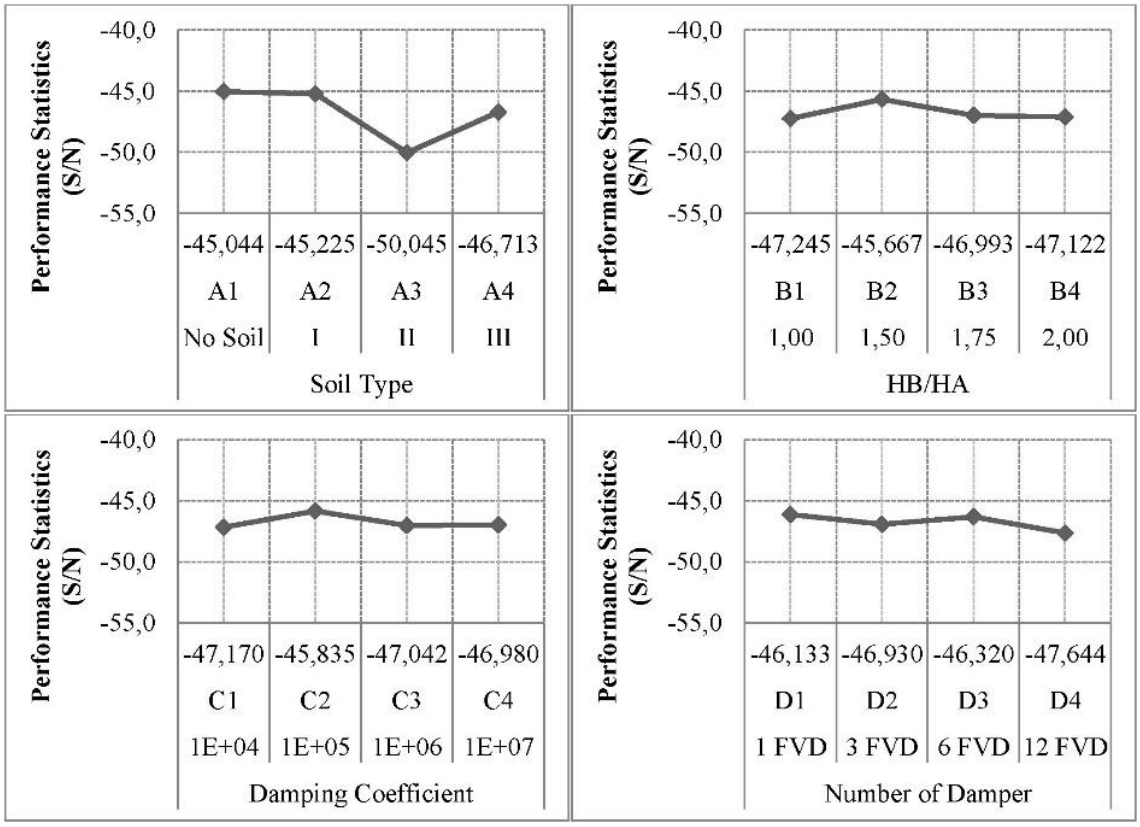

Fig. 6. The effects of parameters on base shear forces for Structure A.

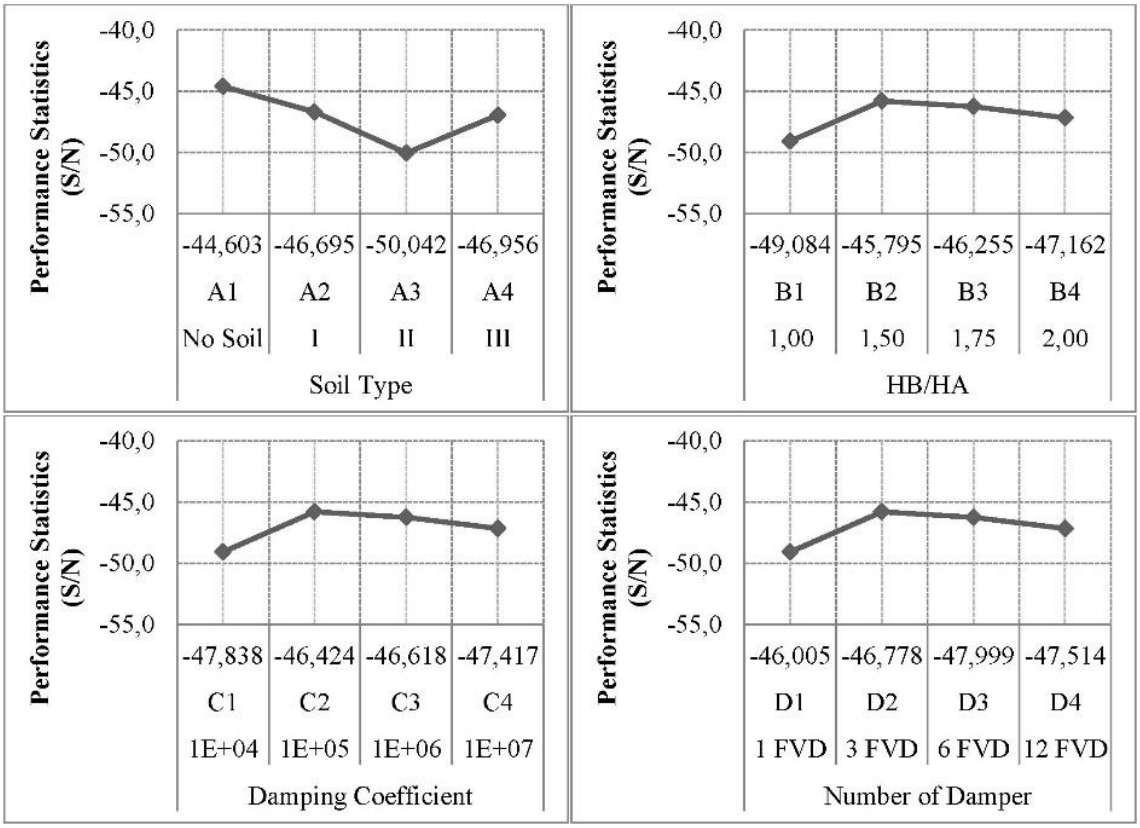

Fig. 7. The effects of parameters on base shear forces for Structure B.

Table 9. Contribution of the factors on the roof displacements of Structure A.

Factors	Level No	Contribution to the S/N
Soil Type	A1	4.349
H_B/H_A Ratio	B2	1.292
Damping Coefficient	C2	1.918
Number of Damper	D1	0.573
Contribution of all factors		8.132
Expected value (S/N) / (m)		23.290 / 0.068
Confirmation result (S/N) / (m)		21.618 / 0.083
Confidence interval (α=95%) (S/N)		19.946 – 26.634

Table 10. Contribution of the factors on the roof displacements of Structure B.

Factors	Level No	Contribution to the S/N
Soil Type	4.415	4.349
H_B/H_A Ratio	5.164	1.292
Damping Coefficient	1.963	1.918
Number of Damper	1.279	0.573
Contribution of all factors		12.821
Expected value (S/N) / (m)		23.555 / 0.066
Confirmation result (S/N) / (m)		20.175 / 0.098
Confidence interval (α=95%) (S/N)		18.658 – 28.452

Table 11. Contribution of the factors on the base shear forces of Structure A.

Factors	Level No	Contribution to the S/N
Soil Type	1.713	4.349
H_B/H_A Ratio	1.090	1.292
Damping Coefficient	0.922	1.918
Number of Damper	0.624	0.573
Contribution of all factors		4.349
Expected value (S/N) / (m)		-42.408 / 131.95
Confirmation result (S/N) / (m)		-43.906 / 156.78
Confidence interval (α=95%) (S/N)		-44.576 – -40.240

Table 12. Contribution of the factors on the base shear forces of Structure B.

Factors	Level No	Contribution to the S/N
Soil Type	2.471	4.349
H_B/H_A Ratio	1.279	1.292
Damping Coefficient	0.650	1.918
Number of Damper	1.069	0.573
Contribution of all factors		5.469
Expected value (S/N) / (m)		-41.605 / 120,30
Confirmation result (S/N) / (m)		-44.210 / 162.37
Confidence interval (α=95%) (S/N)		-46.831 – -36.379

The average S/N effects for roof displacements of Structure A were given in Table 5. Fig. 4 represents the optimum conditions for the roof displacements of Structure A. According to Fig. 4, the parameters and their levels that minimize the maximum roof displacements were A1-B2-C2-D1. This means that the first level of soil type (no soil case), the second level of H_B/H_A ratio of 1.50, the second level of damping coefficient of viscous damper of $1x10^5$ N.s/m and the first level of number of damper (1 FVD) minimize the maximum roof displacements. In other words, the optimum conditions for the roof displacements of Structure A are the first level of soil type, the second level of H_B/H_A ratio, the second level of damping coefficient of damper and the first level of the number of damper. The contribution of the factors on the roof displacements of Structure A and performance prediction are given in Table 9. The most effective factor on the roof displacements of Structure A is soil type, then damping coefficient of damper, then H_B/H_A ratio, and then the number of the damper. The average S/N effects for roof displacements of Structure B are given in Table 6. The optimum conditions for the roof displacements of Structure B are shown in Fig. 5. According to Fig. 5, the parameters and their levels that minimize the maximum roof displacements are A1-B1-C2-D1. This means that the first level of soil type (no soil case), the first level of H_B/H_A ratio of 1.00, the second level of damping coefficient of viscous damper of $1x10^5$ N.s/m and the first level of number of damper (1 FVD) minimize the maximum roof displacements. The contribution of the factors on the roof displacements of Structure A and performance prediction is given in Table 10. The most effective factor on the roof displacements of Structure B is H_B/H_A ratio, then soil type, then the damping coefficient of damper, and then the number of the damper.

The average S/N effects for base shear forces of Structure A are given in Table 7. Fig. 6 represents the optimum conditions for the base shear forces of Structure A. According to Fig. 6, the parameters and their levels that minimize the maximum base shear forces are A1-B2-C2-D1. This means that the optimum conditions for the base shear forces of Structure A are the first level of soil type, the second level of H_B/H_A ratio, the second level of damping coefficient of viscous damper, and the first level of the number of damper. The contribution of the factors on the base shear forces of Structure A and performance prediction is given in Table 11. The most effective factor on the base shear forces of Structure A is soil type, then H_B/H_A ratio, then the damping coefficient of damper, and then the number of the damper. The average S/N effects for base shear forces of Structure B are given in Table 8. Fig. 7 represents the optimum conditions for the base shear forces of Structure B. According to Fig. 7, the parameters and their levels that minimize the maximum base shear forces are A1-B2-C2-D1. This means that the optimum conditions for the base shear forces of Structure B are the first level of soil type, the second level of H_B/H_A ratio, the second level of damping coefficient of viscous damper and the first level of the number of damper. The contribution of the factors on the base shear forces of Structure B and performance prediction is given in Table 12. The most effective factor on the base shear forces of Structure B is soil type, then H_B/H_A ratio, then the number of the damper, and then the damping coefficient of damper.

According to the results, the most effective factor and its level on the roof displacements and the base shear forces for both frames is the first level of soil type, i.e., rigid base (no soil) case. When taking the soil medium into account in the analysis, greater displacement and base shear force values were obtained. This is an expected result. However, the increase in the displacement and base shear force values became apparent when the soil got looser. In other words, as the soil gets stiffer, the displacement and base shear force values systematically decrease. This fact indicates that as the soil gets looser, greater amplification can be expected. It can be also said that, the effectiveness of viscous damper on response mitigation decrease when the soil gets looser. The H_B/H_A ratio has a minor effect on the roof displacements and base shear forces of Structure A, on the other hand, the H_B/H_A ratio is more effective on the response of Structure B which is the taller one. Minimum response is obtained when the H_B/H_A ratio is equal to 1.50 for both frames. Minimum roof displacements and base shear forces are obtained at the second level of the damping coefficient of viscous damper of $1x10^5$ N.s/m. These results correspond with those of the literature. The previous studies indicated that the optimum value of the viscous damper is the value that leads to the minimum response, although no optimization study has been carried out (Bhaskararao and Jangid 2004; Patel and Jangid 2014). Most of the previous papers indicated that the optimum value of the damping coefficient of dampers is between 10^5 and 10^6 N.s/m according to the characteristics of the problem handled in their studies (Xu et al. 1999; Zhang et al. 1999; Wu et al. 2017). The results also show that there is no necessity to interconnect every floor with dampers. Thus, more economical solutions can be obtained by using only one damper. At the optimum conditions, the decrease in the roof displacements and base shear forces of both frames were up to 30% relative to those of the reference system which is the unlinked system. The time histories of the roof displacements and the base shear forces are given in Figs. 8 and 9, respectively.

6. Conclusions

This paper presents optimum conditions for minimum system response of two adjacent frame structures interconnected by viscous dampers, including SSI effects. The optimum parameters were investigated for the adjacent structures-soil system which was subjected to seismic load by 2D FE analysis with the Taguchi method. An optimization study was carried out for soil type, height ratio of the frames, damping coefficient of viscous damper, and the number of viscous damper. According to the optimizations;

- It is determined that the most effective parameter on the system response was Soil Type.
- It can be said that viscous dampers are more effective in response mitigation in relatively stiffer soils.

- The minimum roof displacements and base shear forces were obtained at rigid base (no soil) case, 1.50 for the H_B/H_A ratio, 1x10^5 N.s/m for the damping coefficient of viscous damper, and 1 for the number of the viscous damper.
- When the soil medium is considered in the analysis, the minimum roof displacements and base shear forces were obtained at dense soil (Soil Type I) case, 1.50 for the H_B/H_A ratio, 1x10^5 N.s/m for the damping coefficient of viscous damper, and 1 for the number of the viscous damper.
- In order to obtain the minimum system response, it is sufficient that the damping coefficient of the viscous damper is equal to 1x10^5 N.s/m.
- There is no necessity to connect two neighboring frames by dampers on all floors. More economical solutions can be obtained by using only one damper.
- It is drawn that the Taguchi method can be applied with the FE method for determining optimum conditions of a soil-structure system for minimum system response.

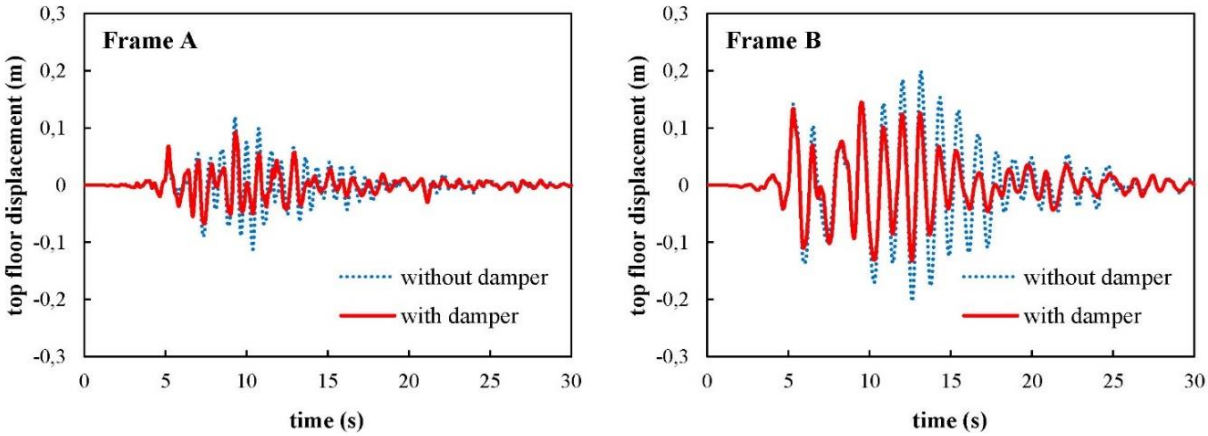

Fig. 8. Top floor displacement time histories at optimum conditions.

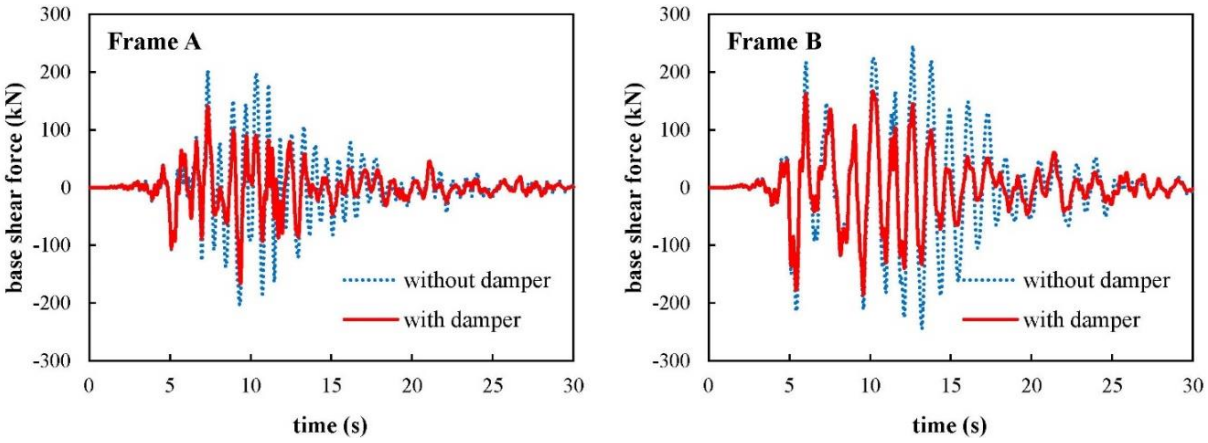

Fig. 9. Base shear force time histories at optimum conditions.

Acknowledgements

None declared.

Funding

The authors received no financial support for the research, authorship, and/or publication of this manuscript.

Conflict of Interest

The authors declared no potential conflicts of interest with respect to the research, authorship, and/or publication of this manuscript.

References

Ada M, Ayvaz Y (2019). The structure-soil-structure interaction effects on the response of the neighbouring frame structures. *Latin American Journal of Solids and Structures*, 16(8), 1-19.

ANSYS (2021). ANSYS Academic Research Mechanical (Version 19).

Avinash AR, Lingaraju MC, Kamath K (2017). Seismic performance of adjacent structures connected with Fluid viscous dampers by considering soil structure interaction-An analytical study. *International Journal of Civil Engineering and Technology*, 8(7), 421-431.

Bakre SV, Jangid RS (2007). Optimum parameters of tuned mass damper for damped main system. *Structural Control and Health Monitoring*, 14(3), 448-470.

Bayrak OÜ, Hınıslıoğlu S (2017). A new approach to the design of rigid pavement: single-axle loading. *Road Materials and Pavement Design*, 18(3), 573-589.

Bharti SD, Dumne SM, Shrimali MK (2010). Seismic response analysis of adjacent buildings connected with MR dampers. *Engineering Structures*, 32(8), 2122-2133.

Bhaskararao AV, Jangid RS (2004). Seismic response of adjacent buildings connected with dampers. *The 13th World Conference on Earthquake Engineering*, Vancouver, BC, Canada, Paper No. 3143, 1-14.

Bhaskararao AV, Jangid RS (2006a). Harmonic response of adjacent structures connected with a friction damper. *Journal of Sound and Vibration*, 292(3-5), 710-725.

Bhaskararao AV, Jangid RS (2006b). Seismic response of adjacent buildings connected with friction dampers. *Bulletin of Earthquake Engineering*, 4(1), 43-64.

Bhaskararao, AV, Jangid RS (2007). Optimum viscous damper for connecting adjacent SDOF structures for harmonic and stationary white-noise random excitations. *Earthquake Engineering and Structural Dynamics*, 36(4), 563-571.

Cimellaro GP, Garcia DL (2007). Seismic response of adjacent buildings connected by nonlinear viscous dampers. *Research Frontiers at Structures Congress*, Long Beach, California, United States, 1-12.

Çelebi E, Göktepe F, Karahan N (2012). Non-linear finite element analysis for prediction of seismic response of buildings considering soil-structure interaction. *Natural Hazards and Earth System Sciences*, 12, 3495-3505.

De Domenico D, Ricciardi G, Takewaki I (2019). Design strategies of viscous dampers for seismic protection of building structures: a review. *Soil Dynamics and Earthquake Engineering*, 118, 144-165.

Düzgün OA, Hatipoğlu YS (2022). Effective damping coefficient of fluid viscous dampers for dynamic response mitigation of coupled frames. *Journal of Vibration Engineering and Technologies*, Article in Press.

Hou CY (2008). Fluid dynamics and behavior of nonlinear viscous fluid dampers. *Journal of Structural Engineering*, 134(1), 56-63.

Housner GW, Bergman A, Caughey TK, Chassiakos AG, Claus RO, Masri SF, Skelton RE, Soong TT, Spencer BF, Yao JTP (1997). Structural control: past, present, and future. *Journal of Engineering Mechanics*, 123(9), 897-971.

Luco JE, De Barros FCP (1998). Optimal damping between two adjacent elastic structures. *Earthquake Engineering and Structural Dynamics*, 27(7), 649-659.

Lysmer J, Kuhlemeyer RL (1969). Finite dynamic model for infinite media. *Journal of the Engineering Mechanics Division,* 95(4), 859-878.

Makris N, Constantinou MC (1990). Viscous dampers: testing, modeling and application in vibration and seismic isolation. *National Center for Earthquake Engineering Research, Technical Report (NCEER-90-0028)*, State University of New York at Buffalo, New York, United States.

Patel CC, Jangid RS (2008). Influence of Soil-structure Interaction on Response of Adjacent SDOF Structures Connected by Viscous Damper. *The 12th International Conference of International Association for Computer Methods and Advances in Geomechanics*, Goa, India, 1-6.

Patel CC, Jangid RS (2014). Dynamic response of identical adjacent structures connected by viscous damper. *Structural Control and Health Monitoring*, 21(2), 205-224.

Taguchi G (1960). Table of orthogonal arrays and linear graphs. *Reports of Statistical Application Research*, 6, 1-52.

Tezcan SS, Uluca O (2003). Reduction of earthquake response of plane frame buildings by viscoelastic dampers. *Engineering Structures*, 25(14), 1755-1761.

Tubaldi E, Barbato M, Dall'Asta A (2014). Performance-based seismic risk assessment for buildings equipped with linear and nonlinear viscous dampers. *Engineering Structures*, 78, 90-99.

Tubaldi E (2015). Dynamic behavior of adjacent buildings connected by linear viscous/viscoelastic dampers. *Structural Control and Health Monitoring*, 22(8), 1086-1102.

Uz ME (2009). Improving the Dynamic Behaviour of Adjacent Buildings by Connecting Them with Fluid Viscous Dampers. *M.Sc. thesis*, School of Civil, Mining and Environmental Engineering, University of Wollongong, Wollongong, Australia.

Westermo BD (1989). The dynamics of interstructural connection to prevent pounding. *Earthquake Engineering and Structural Dynamics*, 18(5), 687-699.

Wolf JP (1988). Soil-Structure Interaction Analysis in Time Domain. Prentice Hall, New Jersey, United States.

Wu QY, Zhu HP, Chen XY (2017). Seismic fragility analysis of adjacent inelastic structures connected with viscous fluid dampers. *Advances in Structural Engineering*, 20(1), 18-33.

Xu YL, He Q, Ko JM (1999). Dynamic response of damper-connected adjacent buildings under earthquake excitation. *Engineering Structures*, 21(2), 135-148.

Zhang W, Xu Y (1999). Dynamic characteristics and seismic response of adjacent buildings linked by discrete dampers. *Earthquake Engineering and Structural Dynamics*, 28(10), 1163-1185.

Zhu H, Wen Y, Iemura H (2001). A study on interaction control for seismic response of parallel structures. *Computers and Structures*, 79(2), 231-242.

Zhu HP, Xu YL (2005). Optimum parameters of Maxwell model-defined dampers used to link adjacent structures. *Journal of Sound and Vibration*, 279(1-2), 253-274.

Zou L, Huang K, Wang L, Butterworth J, Ma X (2012). Vibration control of adjacent buildings considering pile-soil-structure interaction. *Journal of Vibration and Control*, 18(5), 684-695.

Challenge Journal of Structural Mechanics

Research Article

Numerical investigation of the effect of minaret height on its dynamic characteristics

Hakan Erkek [a], Musa Yetkin [b,*], İbrahim Özgür Dedeoğlu [c]

[a] *Department of Civil Engineering, Osmaniye Korkut Ata University, 80010 Osmaniye, Türkiye*
[b] *Department of Civil Engineering, Fırat University, 23119 Elazığ, Türkiye*
[c] *Department of Civil Engineering, Batman University, 72000 Batman, Türkiye*

ABSTRACT

Minarets are structures that have an important place in Islamic architecture. Although these structures have a long, thin and delicate appearance, they can be constructed in different cross-sections and heights. Due to their geometry, minarets can be damaged under earthquake and wind loads. In order to minimize the possibility of damage to these structures, they must be constructed with suitable geometry and materials. In this study, the effect of minaret height on dynamic characteristics (natural frequency and mode shape) was investigated numerically. For numerical application, 19 different minarets with heights ranging from 13.5 m to 33.75 m were modeled in the ANSYS finite element package program. It is assumed that the minarets have as masonry and the base of the minaret was fixed support to the soil. These minarets were evaluated in terms of natural frequency, mode shape and modal mass participation ratios by performing modal analyses. In addition, an equation has been derived that can predict the first natural frequency of the minaret depending on its height.

ARTICLE INFO

Article history:
Received 8 November 2022
Revised 7 December 2022
Accepted 20 December 2022

Keywords:
Minaret
Dynamic characteristic
Natural frequency
Mode shape
Modal mass participation ratio

1. Introduction

Minarets are tower-shaped tall structures built for the purpose of chanting the call to prayer and spreading the sound around. These structures, which are built adjacent to or separately from mosques, have one or more balconies, and the doors of these balconies must face to the qibla. In minarets built adjacent to the mosque, the minaret entrance door usually opens into the mosque. Minarets of different geometries and heights have been built and are still being built all over the world. The minaret of the II. Hasan Mosque in Morocco is the tallest minaret in the world (with a height of 210 m), and the minaret of the Sabancı Merkez Mosque in Adana is the highest minaret in Türkiye (with a height of 99 m) (Fig. 1).

Minarets, which have an important place in Islamic architecture, carry traces of the time they were built and are symbolic structures that have an important place in the urban fabric. Minarets built in different regions reflect the culture of the region they were built because they have different identities. For example, Seljuk and Syrian minarets are generally short, while Ottoman minarets are longer. Iraqi minarets are generally cone-shaped, while Arab minarets are rectangular. In Egyptian architecture, minarets are usually square at the bottom, octagonal in the middle and dome-shaped at the top. Moroccan-style minarets are square at the base as in Egyptian architecture, and as the minaret height increases, narrowing is seen in the section.

Minarets are mostly built with a carcass and masonry load bearing system. While carcass minarets are generally made of reinforced concrete, wood and steel materials, masonry minarets are generally made of stone and brick materials. Minarets are built using these building materials in a way that consists of seven different parts. Minaret parts are boot (pulpit), transition segment, body, balcony, upper part of the minaret body, spire and end ornament. In addition, there are stairs built with or

* *Corresponding author*. Tel.: +90-424-237-0000 ; Fax: +90-424-241-5526 ; E-mail address: musayetkin@firat.edu.tr (M. Yetkin)
ISSN: 2149-8024 / DOI: https://doi.org/10.20528/cjsmec.2023.01.003

without a core inside the minarets, and these stairs generally continue up to the upper part of the minaret body. Explanations about the minaret parts are given below:

- The boot (pulpit) is the bottom part of the minaret, adjacent to the soil/foundation. This part can usually be built as rectangular, cylindrical and polygonal, and in minarets built separately from the mosque, the minaret door is mostly located in this part.
- The transition segment is the part that connects the boot and the body parts. This part is not encountered in minarets that do not differ in size and geometry between the boot and the body.
- The body is the part between the transition segment and the balcony and is generally cylindrical. In order to provide lighting and ventilation in the minaret, small windows are usually opened at regular intervals in this part.
- The balcony is one of the most aesthetically striking parts of the minarets. Almost every minaret has at least one balcony, and in some minarets it is possible to come across 3 balconies.
- The upper part of the minaret body is the part between the balcony and the spire, and is usually built with the same cross-section as the body part.
- The spire is the part that can be called the roof of the minarets and is generally built in the form of cones and domes.
- The end ornament is the part on the top of the minaret that is made in various ways to add beauty to the shape of the spire.

a) II. Hasan Mosque (Morocco) b) Sabancı Merkez Mosque

Fig. 1. The tallest minarets of the (a) world and (b) Türkiye.

Minarets can be damaged or collapsed under earthquake and wind forces due to the structural factors revealed by their architectural appearance (Fig. 2). Various studies are carried out by researchers in order to understand the reasons for these negative situations, to identify minarets that may have the potential to be damaged/collapsed, and to determine what precautions can be taken for minarets with this potential.

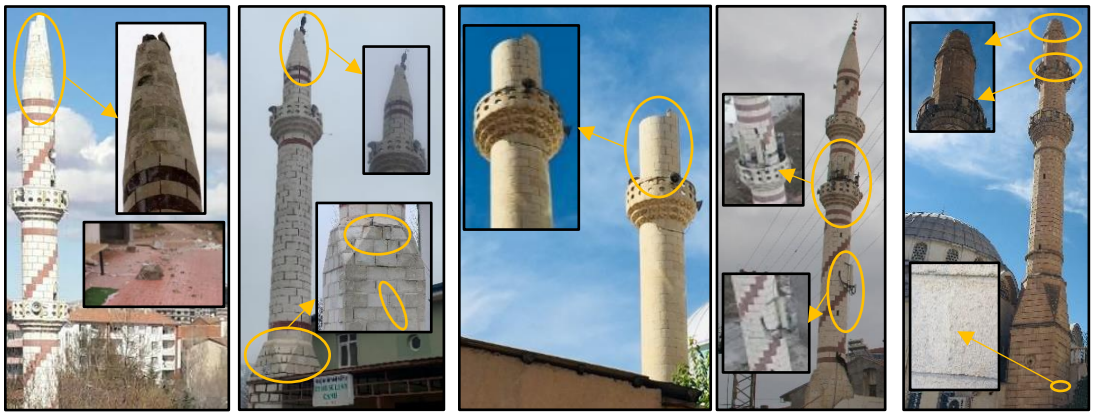

Fig. 2. Some examples for minaret damages (Yetkin et al. 2021).

Köksal et al. (2016) determined the dynamic behavior of the masonry minaret of the Yörgüç Pasha mosque (Samsun) against the ground motion caused by the surface blast-induced ground motion artificially generated

for the finite element model they created. Döven et al. (2018) modeled the Kütahya Yeşil Mosque minaret in two different ways as open and closed balconies, and then performed the experimental measurements of the minaret using operational modal analysis method using 2 different types of accelerometers and compared the finite element model analysis results they obtained with the experimental results. Yetkin et al. (2018) experimentally determined the dynamic characteristics of a reinforced concrete minaret and updated the finite element model in the light of these values. Adam et al. (2020) created a finite element model of a historical masonry minaret and determined its structural behavior under various loadings. Bayraktar and Hökelekli (2020) performed modal analyses and nonlinear seismic performance analyses of different types of minaret-foundation-soil interaction systems for different foundation types. Bayraktar and Hökelekli (2021) created finite element models for minaret types, which they assumed to be formed with different materials, and performed nonlinear analyses by strengthening these models with various methods. At the end of the study, they proposed a cost-effective seismic reinforcement technique with better workability and lower cost. Calayir et al. (2021) updated the finite element model of a masonry minaret by using the dynamic characteristics obtained from the operational modal analysis. Yetkin et al. (2021a) after the M_w=6.8 earthquake that occurred in Elazığ on January 24, 2020, they determined the damages in the minarets in the province of Elazığ and evaluated the causes of these damages. At the end of the study, they made some recommendations for the repair and strengthening of existing damaged minarets and the construction of new minarets. Yetkin et al. (2021b) carried out experimental measurements for a reinforced concrete minaret and updated the numerically constructed finite element model by taking into account the minaret-foundation-soil interaction using the shape functions/mode shapes they obtained. Yetkin et al. (2021c) determined the dynamic characteristics of a reinforced concrete minaret based on environmental vibration data for different measurement schemes. Usta (2021) created finite element models of five different minarets and determined their seismic behavior under various earthquakes. Yurdakul et al. (2021) investigated the earthquake performance of a historical masonry minaret. As a result of finite element model analysis, they stated that damages may occur in some parts of the minaret body.

Although there is no comprehensive standard for minaret design today, there is only a guide published by Presidency of the Republic of Türkiye Presidency of Religious Affairs (PRTPRA) in 2021, which sets some standards on minaret geometry. In this study, finite element models of 19 different masonry minarets with different heights were created, taking into account the guideline published by the PRTPRA. Then, modal analyses were performed for these models. The natural frequencies, mode shapes and modal mass participation ratios obtained as a result of the analyses were evaluated by comparing them with each other. In addition, an equation has been derived to predict the first natural frequency of the minaret depending on the minaret height.

2. Material and Method

2.1. Mosque planning and design guide

The Mosque Planning and Design Guide - 2021 (MPDG 2021), which is recommended to be used in new mosques by the PRTPRA has been published. This guide has brought new recommendations for mosque construction in many respects. Some of these recommendations were made for the design of minarets. These recommendations can be listed as a number of ratios in terms of the numbers and locations of minarets, the number of balconies, the dimensions of the balcony parapets, the width dimensions of the stairs, the positions of the minaret entrance doors and balconies, and the height between the minaret parts according to the mosque type. Some recommendations regarding minaret geometry are given in Fig. 3.

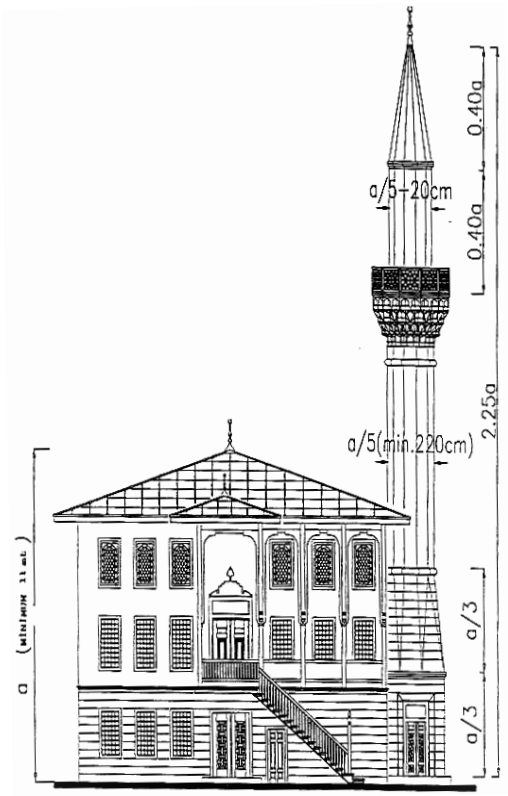

Fig. 3. Some recommendations on minaret geometry (MPDG 2021).

Within the scope of this study, the effect of height variation on natural frequencies, mode shapes and modal mass participation ratios is investigated for minarets with different heights, considering the relationships given in Fig. 3.

3. Numerical Application

Within the scope of the study, finite element models were created by choosing minarets with different heights. While choosing the geometry of each parts of the minarets, the recommendations given in MPDG (2021)

were followed (Fig. 3). The minarets created consist of a single balcony. Door openings at the entrance and balcony of the minarets were taken into account. Details of minaret geometries are given in Table 1.

Table 1. Details of minaret geometries.

*a** (m)	Boot height (m)	Transition segment height (m)	Body (m)	Upper part of the minaret body height (m)	Spire (m)	Wall thickness (m)	Boot cross-section (m^2)	Cylindrical outer diameter (m)	Door openings (m^2)	Total height (m)
6.0	2.00	2.00	4.70	2.40	2.40					13.500
6.5	2.17	2.17	5.09	2.60	2.60					14.625
7.0	2.33	2.33	5.48	2.80	2.80					15.750
7.5	2.50	2.50	5.87	3.00	3.00					16.875
8.0	2.67	2.67	6.27	3.20	3.20					18.000
8.5	2.83	2.83	6.66	3.40	3.40					19.125
9.0	3.00	3.00	7.05	3.60	3.60					20.250
9.5	3.17	3.17	7.44	3.80	3.80					21.375
10.0	3.33	3.33	7.83	4.00	4.00					22.500
10.5	3.50	3.50	8.22	4.20	4.20	0.25	2.6×2.6	2.2	0.5×1.7	23.625
11.0	3.67	3.67	8.62	4.40	4.40					24.750
11.5	3.83	3.83	9.01	4.60	4.60					25.875
12.0	4.00	4.00	9.40	4.80	4.80					27.000
12.5	4.17	4.17	9.79	5.00	5.00					28.125
13.0	4.33	4.33	10.18	5.20	5.20					29.250
13.5	4.50	4.50	10.57	5.40	5.40					30.375
14.0	4.67	4.67	10.97	5.60	5.60					31.500
14.5	4.83	4.83	11.36	5.80	5.80					32.625
15.0	5.00	5.00	11.75	6.00	6.00					33.750

* *a* parameter is given in Fig. 3.

It has been accepted that the minarets have a masonry load bearing system. In the finite element modelling, macro modelling approach was used, and the elasticity modulus, density and Poisson's ratio of the masonry material were chosen as 14000 MPa, 2200 kg/m^3 and 0.2, respectively. It has assumed that the minarets are fixed support at the foundation level. All modellings and analyses were performed with the ANSYS package program (ANSYS 2009). An example of the finite element modelling of minarets is given in Fig. 4.

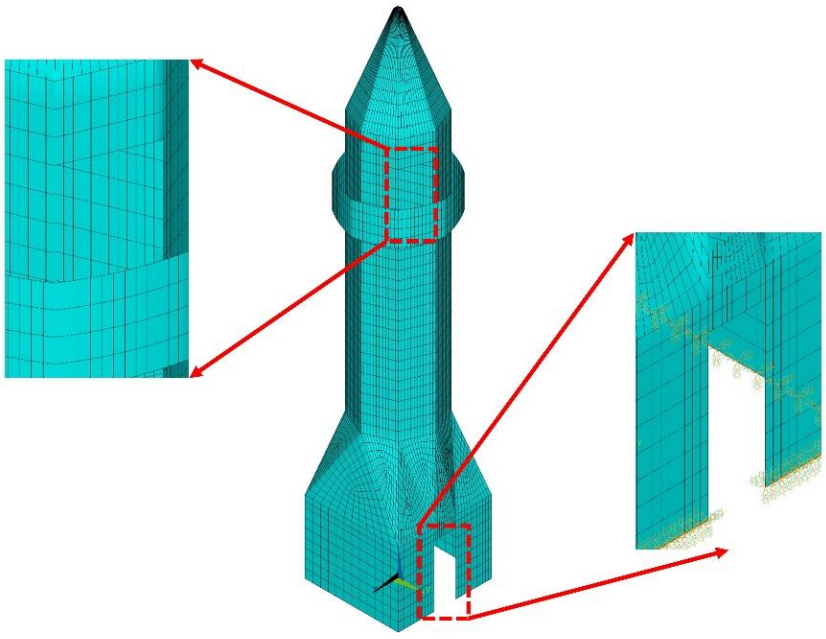

Fig. 4. An example of the finite element modelling of minarets.

4. Results and Discussion

The modal analyses were performed for all minarets and the first 10 natural frequency values obtained are presented in Table 2. When the natural frequency values are examined, it is seen that the natural frequency value decreases as the minaret height increases (the case of the a parameter increasing from 6.0 to 15.0). The largest decrease was 82.56% for the 1st natural frequency value and the smallest decrease was 58.01% for the 5th natural frequency value (Fig. 5).

An equation was derived that allows the first natural frequency values obtained from the study to be estimated depending on the a parameter (Eq. (1)). For Eq. (1), f_1 denotes the first natural frequency value (Hz) and a denotes the parameter related to height (m) shown in Fig. 3.

$$f_1 = 4.229a^4 \, x \, 10^{-5} - 2.147a^3 \, x \, 10^{-3} + 4.181a^2 \, x \, 10^{-2} - 3.799a \, x \, 10^{-1} + 1.44 \quad (1)$$

Table 2. Natural frequency values for the first 10 modes of minarets (in Hz).

Mode	a parameter values (m)																		
	6.0	6.5	7.0	7.5	8.0	8.5	9.0	9.5	10.0	10.5	11.0	11.5	12.0	12.5	13.0	13.5	14.0	14.5	15.0
1	0.258	0.223	0.194	0.171	0.151	0.135	0.121	0.109	0.099	0.090	0.082	0.076	0.070	0.064	0.060	0.055	0.052	0.048	0.045
2	0.262	0.226	0.197	0.173	0.154	0.137	0.123	0.111	0.100	0.091	0.084	0.077	0.071	0.065	0.060	0.056	0.052	0.049	0.046
3	1.092	0.968	0.862	0.771	0.693	0.625	0.566	0.515	0.471	0.432	0.397	0.366	0.339	0.315	0.293	0.273	0.255	0.239	0.224
4	1.112	0.980	0.870	0.777	0.699	0.632	0.574	0.523	0.478	0.439	0.404	0.373	0.345	0.321	0.298	0.278	0.260	0.244	0.229
5	1.196	1.110	1.036	0.971	0.914	0.864	0.818	0.778	0.741	0.707	0.677	0.649	0.623	0.599	0.577	0.556	0.537	0.519	0.502
6	1.624	1.511	1.411	1.324	1.247	1.178	1.115	1.059	1.006	0.949	0.884	0.822	0.766	0.715	0.669	0.627	0.589	0.554	0.522
7	2.225	1.990	1.790	1.618	1.470	1.340	1.227	1.128	1.042	0.974	0.912	0.848	0.789	0.737	0.689	0.645	0.606	0.570	0.537
8	2.281	2.040	1.835	1.659	1.507	1.375	1.259	1.156	1.066	0.985	0.927	0.887	0.850	0.817	0.787	0.758	0.732	0.707	0.684
9	3.111	2.881	2.684	2.512	2.361	2.225	2.090	1.936	1.793	1.664	1.549	1.445	1.351	1.266	1.188	1.118	1.053	0.993	0.938
10	3.723	3.342	3.017	2.738	2.497	2.288	2.115	1.969	1.824	1.692	1.573	1.466	1.369	1.281	1.201	1.128	1.062	1.000	0.944

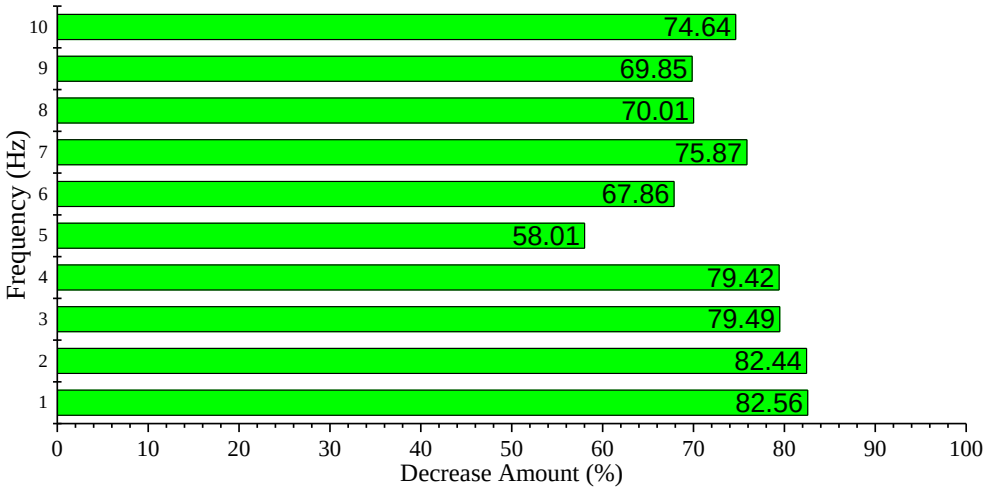

Fig. 5. The decrease amount in the natural frequency for the case where the a parameter increases from 6 to 15.

As a result of the modal analyses of the minarets, the mode shapes were obtained also. It has been observed that the mode shapes are generally similar. For this reason, mode shapes for only a=6.0 m solutions are given for the first 10 modes (Fig. 6). Graphics of visual comparison of mode shapes from different perspectives are shown in Figs. 7 and 8. According to Figs. 7 and 8, it is possible to say that the similarity of mode shapes is higher for the first modes, but this similarity gradually decreases for the later modes.

Furthermore, modal mass participation ratios (MMPR) were calculated as a result of the modal analysis of the minarets. In order to evaluate the effect of each mode on this ratio in a wider perspective, the MMPR of the first 50 modes are calculated and given in Tables 3 and 4.

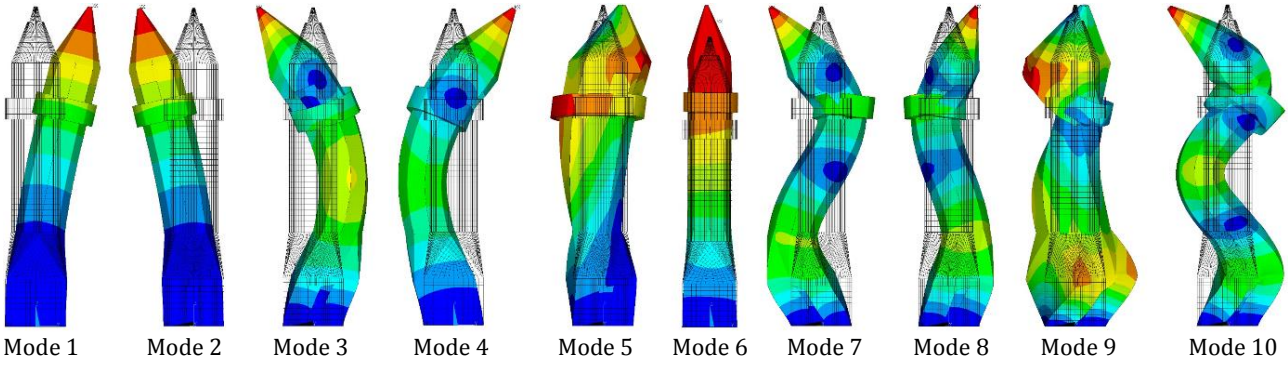

Fig. 6. First 10 mode shapes for a=6.0 m solutions.

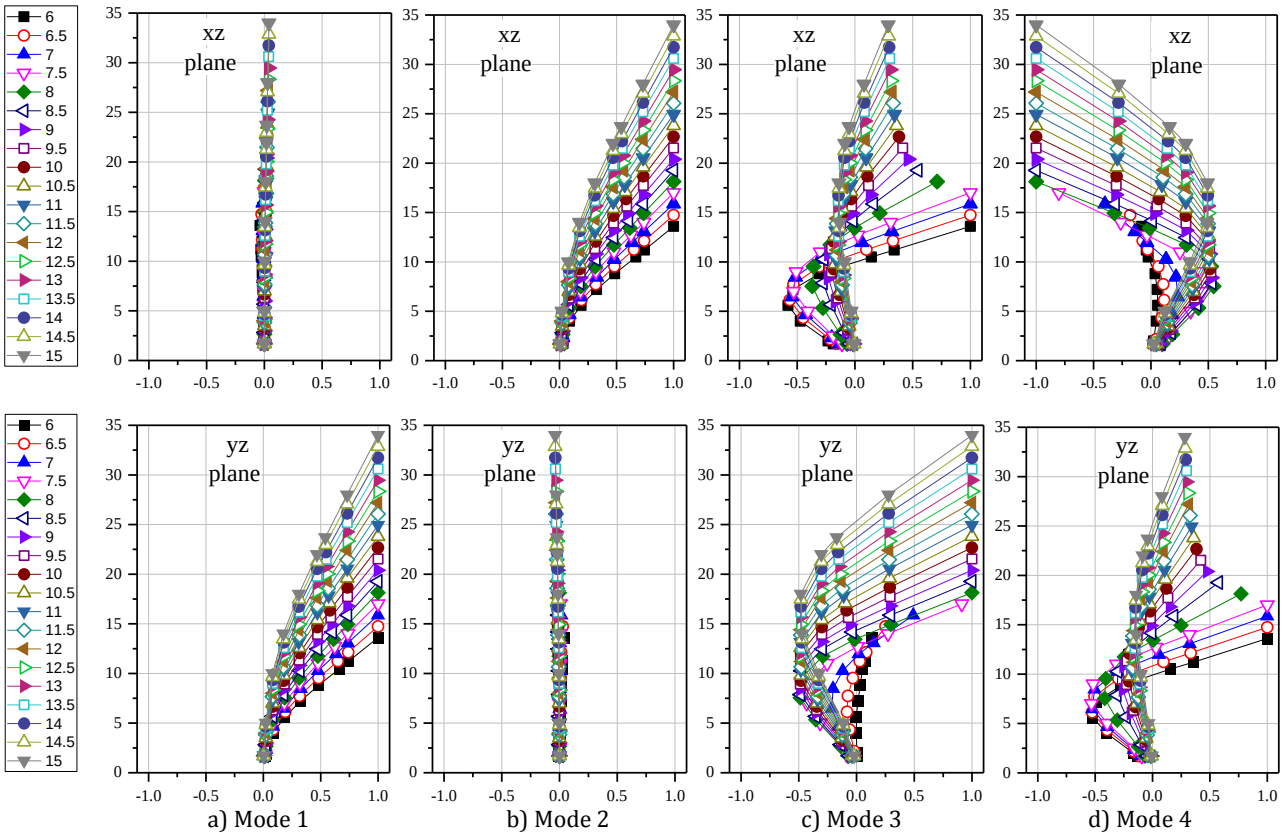

Fig. 7. Comparisons of mode shapes 1-4.

For the MMPR values given in Tables 3 and 4, values between 86.701-89.970% in the x direction and 81.996-85.225% in the y direction were obtained for the first 10 modes. For the first 10 modes, it was observed that as the minaret height increased, the MMPR decreased for both directions (x-y). For the first 20 and first 30 modes, there is no such relationship between minaret height and the MMPR. For the first 40 modes, values in the range of 94.056-96.532% in the x direction and 94.016-96.344% in the y direction were obtained. For the first 50 modes, values in the range of 94.859-96.827% in the x direction and 94.703-96.750% in the y direction were obtained. For the first 40 and 50 modes, the MMPR increased as the minaret height increased.

5. Conclusions

In this study, the effect of height on dynamic characteristics was investigated for 19 different minaret examples with heights ranging from 13.5 to 33.75 m. Finite element models of these 19 different minarets were created for numerical application. It is assumed that the minarets were built as masonry and connected to the soil with a fixed support. In addition, it is thought that the minarets have only one balcony, and both the balcony and the minaret entrance door openings are taken into account. Modal analyses were carried out for the minarets and their evaluations were made in terms of natural frequencies, mode shapes and modal mass participation ratios. The results obtained within the scope of the study are listed below:

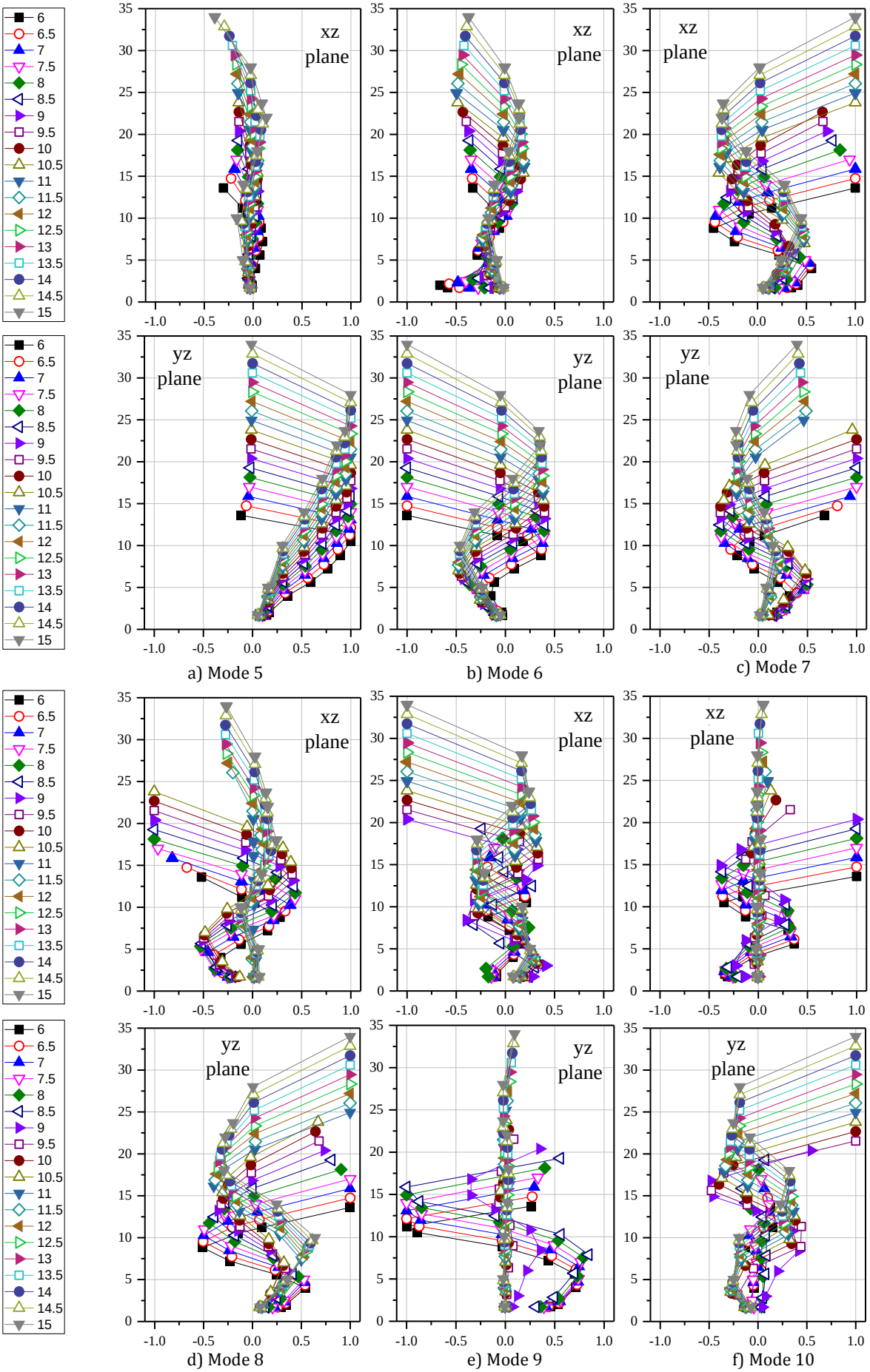

Fig. 8. Comparisons of mode shapes 5-10.

Table 3. Modal mass participation ratios (MMPR) for the *x* direction.

Mode	α parameter values (m)															
	6.0	6.5	7.0	7.5	8.0	8.5	9.0	9.5	10.0	10.5	11.0	11.5	12.0	12.5	13.0	13.5	14.0	14.5	15.0
1	0.077	0.032	0.010	0.001	0.001	0.005	0.011	0.019	0.026	0.033	0.040	0.046	0.051	0.056	0.060	0.064	0.067	0.070	0.072
2	51.172	50.937	50.716	50.510	50.322	50.152	49.999	49.861	49.737	49.626	49.526	49.436	49.353	49.279	49.211	49.149	49.092	49.039	48.991
3	26.434	24.357	20.953	14.231	8.592	5.703	4.251	3.439	2.937	2.601	2.363	2.186	2.051	1.944	1.857	1.786	1.726	1.675	1.632
4	0.304	1.149	4.214	10.591	15.904	18.490	19.663	20.222	20.496	20.624	20.675	20.683	20.667	20.637	20.599	20.559	20.517	20.476	20.436
5	0.124	0.009	0.001	0.010	0.020	0.029	0.037	0.043	0.049	0.055	0.061	0.068	0.076	0.087	0.103	0.126	0.164	0.235	0.400
6	0.003	0.004	0.005	0.007	0.010	0.016	0.029	0.070	0.276	1.381	2.017	2.025	1.933	1.825	1.720	1.620	1.524	1.426	1.301
7	6.933	6.352	5.725	5.109	4.555	4.068	3.648	3.285	2.874	2.154	8.695	8.622	8.659	8.704	8.738	8.758	8.758	8.729	8.633
8	2.541	3.816	4.452	5.298	6.014	6.604	7.072	7.421	7.623	7.216	0.000	0.014	0.010	0.007	0.005	0.004	0.003	0.002	0.002
9	0.001	0.000	0.008	0.030	0.090	0.331	2.842	4.495	4.736	4.875	4.979	5.058	5.117	5.159	5.187	5.203	5.208	5.205	5.193
10	2.382	2.839	3.252	3.545	3.791	3.820	1.536	0.083	0.017	0.004	0.001	0.000	0.001	0.004	0.008	0.014	0.020	0.029	0.041
Total MMPR value for the first 10 modes ∑	89.970	89.496	89.336	89.332	89.299	89.218	89.089	88.939	88.771	88.569	88.356	88.137	87.919	87.702	87.488	87.281	87.080	86.886	86.701
11	0.076	0.075	0.055	0.034	0.016	0.003	0.004	0.005	0.006	0.030	0.061	0.097	0.138	0.188	0.249	0.330	0.439	0.598	0.838
12	0.177	1.001	0.904	0.950	1.058	1.271	1.572	1.890	2.155	2.355	2.504	2.616	2.698	2.753	2.781	2.780	2.745	2.670	2.244
13	0.011	0.012	0.016	0.028	0.207	1.063	0.812	0.520	0.371	0.294	0.249	0.217	0.192	0.170	0.149	0.127	0.099	0.050	0.265
14	0.000	0.134	0.884	1.059	0.949	0.034	0.109	0.203	0.202	0.184	0.178	0.191	0.224	0.288	0.405	0.634	1.074	1.667	1.994
15	0.636	0.370	0.074	0.054	0.021	0.000	0.000	0.000	0.001	0.002	0.003	0.005	0.008	0.016	0.034	0.083	0.064	0.017	0.209
16	0.122	0.231	0.185	0.061	0.000	0.499	1.406	1.586	1.638	1.639	1.611	1.568	1.511	1.433	1.327	1.294	1.198	0.703	0.246
17	0.040	0.036	1.382	1.495	1.575	0.999	0.000	0.011	0.052	0.121	0.205	0.291	0.372	0.441	0.472	0.287	0.019	0.022	0.012
18	0.094	0.006	0.006	0.121	0.090	0.172	0.278	0.113	0.051	0.015	0.010	0.574	0.800	0.908	0.983	1.047	1.105	1.160	1.211
19	0.001	0.000	0.023	0.000	0.001	0.001	0.005	0.011	0.024	0.059	0.208	0.195	0.114	0.085	0.077	0.074	0.072	0.072	0.072
20	1.347	1.315	0.098	0.012	0.000	0.000	0.046	0.370	0.785	0.826	0.653	0.001	0.036	0.040	0.046	0.060	0.086	0.133	0.219
Total MMPR value for the first 20 modes ∑	92.474	92.676	92.962	93.147	93.216	93.258	93.322	93.650	94.056	94.093	94.038	93.891	94.012	94.024	94.013	93.996	93.980	93.979	94.011
21	0.135	0.152	0.046	0.001	0.000	0.010	0.006	0.457	0.058	0.016	0.061	0.191	0.048	0.010	0.007	0.544	0.705	0.724	0.695
22	0.050	0.063	0.039	0.000	0.001	0.126	0.777	0.014	0.005	0.002	0.001	0.000	0.000	0.000	0.001	0.000	0.013	0.022	0.013
23	0.002	0.001	0.002	0.004	0.008	0.185	0.002	0.000	0.000	0.477	0.531	0.579	0.625	0.666	0.686	0.142	0.018	0.007	0.004
24	0.007	0.003	0.101	0.762	0.786	0.556	0.066	0.263	0.410	0.000	0.062	0.062	0.062	0.060	0.060	0.084	0.041	0.012	0.002
25	0.003	0.000	0.037	0.118	0.114	0.012	0.003	0.025	0.058	0.061	0.000	0.000	0.004	0.011	0.395	0.523	0.535	0.536	0.535
26	0.001	0.435	0.275	0.109	0.025	0.153	0.232	0.095	0.029	0.040	0.023	0.014	0.000	0.628	0.202	0.084	0.111	0.135	0.156
27	0.032	0.286	0.493	0.000	0.096	0.049	0.037	0.041	0.002	0.007	0.363	0.531	0.604	0.001	0.064	0.071	0.047	0.036	0.030
28	0.589	0.056	0.010	0.001	0.000	0.052	0.053	0.032	0.015	0.001	0.017	0.011	0.002	0.000	0.000	0.020	0.053	0.095	0.138
29	0.006	0.000	0.003	0.004	0.008	0.000	0.008	0.002	0.001	0.082	0.022	0.115	0.068	0.015	0.001	0.000	0.000	0.003	0.046
30	0.106	0.000	0.002	0.005	0.001	0.007	0.000	0.511	0.526	0.368	0.245	0.007	0.001	0.001	0.000	0.000	0.036	0.044	0.001
Total MMPR value for the first 30 modes ∑	93.405	93.674	93.970	94.151	94.254	94.408	94.506	95.089	95.161	95.147	95.364	95.402	95.425	95.417	95.428	95.464	95.539	95.593	95.630
31	0.003	0.001	0.116	0.000	0.019	0.000	0.490	0.001	0.091	0.168	0.001	0.000	0.000	0.019	0.018	0.000	0.011	0.206	0.193
32	0.029	0.111	0.003	0.000	0.000	0.063	0.031	0.083	0.000	0.000	0.000	0.000	0.004	0.019	0.051	0.045	0.122	0.000	0.000
33	0.091	0.210	0.005	0.007	0.006	0.019	0.041	0.000	0.000	0.000	0.037	0.015	0.002	0.173	0.308	0.307	0.147	0.021	0.000
34	0.152	0.022	0.011	0.005	0.503	0.420	0.003	0.000	0.091	0.063	0.000	0.000	0.344	0.174	0.037	0.174	0.216	0.250	0.273
35	0.276	0.031	0.000	0.010	0.062	0.074	0.016	0.052	0.000	0.000	0.063	0.074	0.037	0.016	0.005	0.011	0.029	0.029	0.029
36	0.003	0.022	0.013	0.021	0.009	0.001	0.000	0.002	0.000	0.172	0.362	0.320	0.000	0.000	0.099	0.012	0.058	0.046	0.032
37	0.000	0.008	0.002	0.282	0.000	0.006	0.108	0.062	0.000	0.040	0.000	0.038	0.060	0.086	0.000	0.004	0.011	0.003	0.005
38	0.066	0.020	0.000	0.048	0.021	0.010	0.002	0.001	0.051	0.063	0.010	0.000	0.113	0.098	0.015	0.098	0.000	0.000	0.126
39	0.025	0.015	0.009	0.108	0.024	0.002	0.005	0.002	0.054	0.013	0.000	0.087	0.034	0.057	0.128	0.000	0.000	0.000	0.000
40	0.006	0.015	0.015	0.063	0.002	0.000	0.001	0.000	0.013	0.154	0.002	0.027	0.000	0.000	0.002	0.008	0.032	0.116	0.242
Total MMPR value for the first 40 modes ∑	94.056	94.131	94.146	94.694	94.900	95.003	95.205	95.291	95.461	95.819	95.838	95.962	96.018	96.060	96.092	96.122	96.165	96.264	96.532
41	0.025	0.210	0.527	0.113	0.000	0.013	0.012	0.000	0.000	0.000	0.026	0.001	0.000	0.006	0.308	0.345	0.334	0.254	0.004
42	0.005	0.001	0.001	0.001	0.011	0.006	0.001	0.055	0.022	0.009	0.000	0.000	0.067	0.211	0.008	0.020	0.016	0.012	0.003
43	0.001	0.000	0.002	0.063	0.062	0.080	0.000	0.001	0.034	0.001	0.053	0.000	0.000	0.001	0.020	0.000	0.000	0.002	0.009
44	0.091	0.000	0.000	0.001	0.014	0.274	0.215	0.142	0.261	0.031	0.001	0.068	0.071	0.076	0.036	0.001	0.011	0.000	0.028
45	0.030	0.111	0.167	0.000	0.285	0.017	0.048	0.053	0.036	0.023	0.033	0.001	0.005	0.000	0.006	0.029	0.000	0.029	0.003
46	0.003	0.011	0.074	0.050	0.008	0.014	0.005	0.170	0.036	0.001	0.011	0.022	0.005	0.009	0.005	0.000	0.021	0.001	0.035
47	0.013	0.402	0.012	0.053	0.055	0.025	0.000	0.002	0.001	0.011	0.004	0.002	0.005	0.032	0.000	0.000	0.001	0.018	0.205
48	0.085	0.002	0.015	0.173	0.000	0.000	0.093	0.003	0.000	0.008	0.013	0.009	0.109	0.005	0.009	0.011	0.000	0.000	0.002
49	0.527	0.020	0.014	0.080	0.076	0.072	0.040	0.113	0.007	0.001	0.001	0.017	0.032	0.000	0.000	0.017	0.051	0.144	0.000
50	0.024	0.038	0.002	0.016	0.021	0.001	0.157	0.002	0.000	0.001	0.005	0.119	0.001	0.032	0.000	0.000	0.007	0.002	0.007
Total MMPR value for the first 50 modes ∑	94.859	94.925	94.961	95.244	95.432	95.507	95.775	95.833	95.858	95.904	95.986	96.200	96.314	96.432	96.484	96.545	96.607	96.727	96.827

Table 4. Modal mass participation ratios (MMPR) for the *y* direction.

Mode	α parameter values (m)																			
	6.0	6.5	7.0	7.5	8.0	8.5	9.0	9.5	10.0	10.5	11.0	11.5	12.0	12.5	13.0	13.5	14.0	14.5	15.0
1	51.066	50.880	50.700	50.531	50.373	50.228	50.095	49.974	49.863	49.762	49.670	49.586	49.508	49.437	49.372	49.311	49.256	49.204	49.155
2	0.079	0.033	0.010	0.001	0.001	0.005	0.012	0.019	0.027	0.034	0.041	0.047	0.053	0.058	0.062	0.066	0.069	0.072	0.075
3	0.220	0.978	3.761	9.664	14.682	17.203	18.409	19.034	19.383	19.590	19.715	19.792	19.840	19.869	19.886	19.894	19.897	19.896	19.893
4	23.433	22.513	19.517	13.410	8.203	5.511	4.151	3.387	2.913	2.594	2.369	2.200	2.071	1.968	1.884	1.815	1.757	1.707	1.665
5	0.140	0.047	0.023	0.014	0.009	0.007	0.005	0.004	0.003	0.003	0.002	0.002	0.002	0.002	0.002	0.002	0.002	0.002	0.000
6	0.000	0.001	0.005	0.013	0.028	0.057	0.124	0.320	1.220	5.274	7.578	8.084	8.302	8.439	8.540	8.620	8.687	8.750	8.821
7	2.635	3.585	4.468	5.246	5.889	6.400	6.767	6.901	6.216	2.019	1.683	1.872	1.799	1.702	1.607	1.517	1.433	1.349	1.256
8	7.242	6.456	5.690	4.988	4.388	3.883	3.467	3.141	2.921	3.050	1.064	0.346	0.174	0.106	0.072	0.053	0.040	0.032	0.026
9	0.000	0.001	0.005	0.015	0.044	0.148	0.369	0.125	0.061	0.033	0.018	0.009	0.003	0.001	0.000	0.001	0.005	0.010	0.018
10	0.411	0.309	0.212	0.133	0.067	0.008	0.030	0.502	0.784	0.964	1.042	1.084	1.109	1.121	1.126	1.123	1.116	1.104	1.087
Total MMPR value for the first 10 modes ∑	85.225	84.801	84.391	84.015	83.684	83.450	83.427	83.406	83.391	83.324	83.182	83.022	82.862	82.704	82.550	82.403	82.261	82.125	81.996
11	3.896	4.171	4.405	4.589	4.723	4.758	4.580	3.905	0.227	0.105	0.064	0.046	0.037	0.033	0.030	0.031	0.033	0.037	0.045
12	0.141	0.128	0.133	0.150	0.181	0.220	0.256	0.271	0.265	0.248	0.228	0.208	0.189	0.169	0.148	0.124	0.093	0.041	0.366
13	0.079	0.081	0.089	0.110	0.192	0.353	1.137	1.903	2.251	2.417	2.515	2.583	2.633	2.674	2.710	2.744	2.781	2.833	2.505
14	0.002	0.017	0.015	0.002	0.000	0.467	1.298	1.064	0.251	0.127	0.072	0.043	0.027	0.016	0.007	0.001	0.008	0.082	0.240
15	0.053	0.176	2.142	2.220	2.195	1.598	0.006	0.009	0.022	0.033	0.045	0.061	0.087	0.142	0.282	0.721	1.598	2.186	2.237
16	0.862	1.840	0.001	0.000	0.000	0.008	0.005	0.004	0.046	0.128	0.231	0.338	0.437	0.511	0.500	0.150	0.234	0.080	0.003
17	0.119	0.006	0.217	0.198	0.158	0.313	1.987	2.057	2.076	2.048	1.992	1.921	1.842	1.758	1.668	1.614	0.671	0.187	0.075
18	0.832	0.026	0.001	1.513	1.665	1.593	0.000	0.000	0.000	0.001	0.025	0.066	0.057	0.052	0.051	0.052	0.053	0.055	0.056
19	0.044	0.022	0.003	0.014	0.016	0.006	0.001	0.000	0.003	0.014	0.028	0.504	1.206	1.353	1.415	1.455	1.486	1.513	1.537
20	0.242	0.229	0.976	0.035	0.010	0.008	0.278	0.512	0.129	0.073	0.271	0.825	0.190	0.079	0.049	0.037	0.032	0.032	0.034
Total MMPR value for the first 20 modes ∑	91.495	91.496	92.372	92.846	92.823	92.774	92.975	93.131	92.662	92.518	92.653	93.618	93.568	93.490	93.410	93.330	93.249	93.171	93.093
21	1.026	1.182	0.401	0.000	0.000	0.090	0.008	0.417	1.123	1.253	1.061	0.024	0.000	0.000	0.001	0.039	0.048	0.036	0.015
22	0.062	0.080	0.063	0.001	0.006	0.008	0.010	0.373	0.073	0.017	0.003	0.000	0.001	0.007	0.026	0.132	0.582	0.879	0.973
23	0.003	0.013	0.023	0.039	0.073	0.586	0.978	0.004	0.003	0.092	0.095	0.096	0.095	0.092	0.089	0.094	0.339	0.081	0.032
24	0.002	0.000	0.001	0.150	0.140	0.238	0.017	0.057	0.083	0.006	0.655	0.699	0.739	0.774	0.792	0.675	0.000	0.000	0.000
25	0.005	0.000	0.039	1.037	1.046	0.362	0.028	0.113	0.544	0.603	0.002	0.001	0.003	0.012	0.051	0.094	0.138	0.174	0.204
26	0.041	0.232	0.614	0.000	0.001	0.032	0.048	0.035	0.005	0.002	0.001	0.002	0.001	0.000	0.457	0.760	0.735	0.714	0.699
27	0.007	0.226	0.431	0.001	0.009	0.004	0.402	0.373	0.014	0.004	0.030	0.020	0.005	0.811	0.333	0.004	0.001	0.000	0.000
28	0.096	0.183	0.001	0.000	0.002	0.320	0.011	0.002	0.000	0.004	0.688	0.761	0.797	0.001	0.001	0.007	0.013	0.020	0.026
29	0.017	0.289	0.014	0.001	0.026	0.003	0.000	0.000	0.002	0.008	0.041	0.000	0.000	0.000	0.003	0.000	0.000	0.026	0.452
30	0.647	0.005	0.004	0.000	0.005	0.001	0.003	0.100	0.108	0.203	0.000	0.001	0.000	0.000	0.000	0.000	0.317	0.420	0.006
Total MMPR value for the first 30 modes ∑	93.400	93.706	93.961	94.077	94.132	94.417	94.480	94.604	94.617	94.709	95.230	95.223	95.209	95.188	95.163	95.136	95.424	95.521	95.500
31	0.001	0.003	0.032	0.005	0.151	0.002	0.095	0.001	0.580	0.513	0.001	0.000	0.001	0.001	0.001	0.022	0.102	0.037	0.031
32	0.003	0.024	0.009	0.002	0.000	0.003	0.134	0.549	0.008	0.008	0.001	0.003	0.001	0.333	0.424	0.422	0.061	0.001	0.002
33	0.251	0.055	0.002	0.000	0.001	0.014	0.347	0.002	0.000	0.005	0.003	0.001	0.010	0.001	0.040	0.031	0.000	0.001	0.000
34	0.083	0.237	0.135	0.027	0.098	0.088	0.009	0.006	0.010	0.007	0.004	0.003	0.030	0.036	0.009	0.037	0.039	0.039	0.037
35	0.051	0.018	0.004	0.001	0.406	0.448	0.012	0.008	0.003	0.000	0.408	0.408	0.438	0.113	0.025	0.073	0.322	0.344	0.362
36	0.024	0.092	0.000	0.320	0.064	0.008	0.011	0.002	0.001	0.003	0.058	0.068	0.006	0.004	0.029	0.161	0.003	0.002	0.001
37	0.007	0.000	0.000	0.016	0.050	0.000	0.009	0.006	0.000	0.308	0.011	0.020	0.024	0.028	0.004	0.073	0.001	0.000	0.002
38	0.147	0.032	0.016	0.257	0.000	0.002	0.000	0.000	0.011	0.002	0.015	0.001	0.022	0.047	0.266	0.004	0.002	0.003	0.241
39	0.049	0.000	0.002	0.002	0.004	0.053	0.000	0.001	0.000	0.113	0.000	0.014	0.193	0.204	0.002	0.003	0.003	0.001	0.003
40	0.000	0.114	0.437	0.075	0.006	0.002	0.040	0.021	0.000	0.009	0.000	0.147	0.002	0.000	0.012	0.030	0.086	0.204	0.165
Total MMPR value for the first 40 modes ∑	94.016	94.282	94.598	94.783	94.913	95.038	95.138	95.200	95.232	95.670	95.731	95.888	95.933	95.955	95.974	95.993	96.043	96.153	96.344
41	0.001	0.008	0.016	0.002	0.005	0.001	0.008	0.001	0.000	0.162	0.002	0.002	0.148	0.057	0.016	0.033	0.050	0.150	0.027
42	0.006	0.004	0.013	0.008	0.001	0.000	0.016	0.001	0.024	0.010	0.139	0.011	0.002	0.027	0.072	0.403	0.323	0.102	0.022
43	0.488	0.000	0.001	0.006	0.008	0.012	0.000	0.068	0.417	0.021	0.000	0.129	0.014	0.225	0.384	0.000	0.001	0.000	0.001
44	0.002	0.459	0.340	0.011	0.028	0.046	0.045	0.037	0.059	0.000	0.004	0.001	0.000	0.001	0.003	0.006	0.000	0.001	0.005
45	0.012	0.017	0.031	0.273	0.038	0.195	0.395	0.431	0.113	0.001	0.004	0.007	0.008	0.006	0.011	0.001	0.000	0.004	0.037
46	0.033	0.006	0.004	0.006	0.110	0.159	0.016	0.014	0.002	0.002	0.070	0.000	0.004	0.034	0.001	0.057	0.002	0.013	0.220
47	0.026	0.070	0.007	0.014	0.317	0.082	0.018	0.004	0.001	0.002	0.011	0.001	0.006	0.098	0.003	0.006	0.125	0.251	0.035
48	0.081	0.014	0.002	0.063	0.202	0.203	0.002	0.002	0.001	0.039	0.032	0.020	0.038	0.002	0.002	0.000	0.009	0.005	0.001
49	0.034	0.078	0.126	0.285	0.018	0.004	0.006	0.017	0.000	0.002	0.003	0.015	0.128	0.014	0.000	0.000	0.000	0.016	0.002
50	0.003	0.089	0.077	0.009	0.015	0.012	0.121	0.038	0.000	0.001	0.001	0.023	0.001	0.009	0.000	0.000	0.128	0.008	0.057
Total MMPR value for the first 50 modes ∑	94.703	95.027	95.214	95.461	95.655	95.754	95.764	95.814	95.849	95.911	95.995	96.097	96.281	96.428	96.467	96.499	96.681	96.703	96.750

- It has been determined that the natural frequency values decrease as the minaret height increases (in case of the *a* parameter increases from 6.0 to 15.0). However, this amount of decrease did not occur proportionally between the increase in the natural frequency number and the increase in the height.
- Mode shapes are generally similar in the first modes. However, it has been observed that this similarity gradually decreases for the following modes.
- For the first 10 modes, it was determined that as the minaret height increased, the modal mass participation ratios in both *x* and *y* directions decreased.
- For the first 10 modes, a modal mass participation ratios of over 80% was achieved in both directions (*x*-*y*). These ratios were higher in the *x* direction and ranged from 86.701 to 89.970%. In the *y* direction, these ratios are in the range of 81.996-85.225%.
- For the first 20 and 30 modes, no linear relationship could be obtained between the change in minaret height and the change in modal mass participation ratios.
- For the first 40 and 50 modes, it has been determined that as the minaret height increases, the modal mass participation ratios increase in both *x* and *y* directions.

In the study, an equation was derived that allows the first natural frequency of minarets to be estimated depending on the minaret height. It should be noted that this equation is specific to the selected minaret material and geometry properties. It will be useful to develop this equation for minarets with different material and geometry properties.

Acknowledgements

None declared.

Funding

The authors received no financial support for the research, authorship, and/or publication of this manuscript.

Conflict of Interest

The authors declared no potential conflicts of interest with respect to the research, authorship, and/or publication of this manuscript.

References

Adam MA, El-Salakawy TS, Salama MA, Mohamed AA (2020). Assessment of structural condition of a historic masonry minaret in Egypt. *Case Studies in Construction Materials,* 13, e00409.

ANSYS Inc. (2017). ANSYS Mechanical Theory Reference: Release 18.1. Canonsburg, PA, USA.

Bayraktar A, Hökelekli E (2020). Influences of earthquake input models on nonlinear seismic performances of minaret-foundation-soil interaction systems. *Soil Dynamics and Earthquake Engineering,* 139, 106368.

Bayraktar A. Hökelekli E (2021). A cost-effective FRCM technique for seismic strengthening of minarets. *Engineering Structures,* 229, 111672.

Calayır Y, Yetkin M, Erkek H (2021). Finite element model updating of masonry minarets by using operational modal analysis method. *Structures,* 34, 3501-3507.

MPDG (2021). Cami Planlama ve Tasarımı Kılavuzu, Presidency of the Republic of Türkiye Presidency of Religious Affairs, Ankara, Türkiye (in Turkish).

Döven M, Serhatoğlu C, Kaplan O, Livaoğlu R (2018). Dynamic behavior change of Kütahya Yeşil Minaret with covered and open balcony architecture. *Eskişehir Technical University Journal of Science and Technology B- Theoritical Sciences,* 6, 192–203 (in Turkish).

Köksal O, Hacıefendioğlu K, Alpaslan E, Birinci F (2016). Influence of blast-induced ground motion on dynamic response of masonry minaret of Yörgüç Paşa Mosque. *Challenge Journal of Structural Mechanics,* 3(1), 31–37.

Usta P (2021). Assessment of seismic behavior of historic masonry minarets in Antalya, Türkiye. *Case Studies in Construction Materials,* 15, e00665.

Yetkin M, Erkek H, Calayır Y (2018). Determining dynamic characteristics of reinforced concrete minarets and updating of their finite element models using environmental vibration data. *Fırat University Turkish Journal of Science & Technology,* 13(1), 93-98.

Yetkin M, Dedeoğlu İÖ, Calayır Y (2021a). Investigation and assessment of damages in the minarets existing at Elazig after 24 January 2020 Sivrice Earthquake. *Fırat University Journal of Engineering Science,* 33(2), 379-389 (in Turkish).

Yetkin M, Erkek H, Calayır Y (2021b). Model updating of a reinforced concrete minaret by using ambient vibration tests. *9th Turkish Conference on Earthquake Engineering*, Istanbul, Türkiye, 459-467.

Yetkin M, Erkek H, Calayır, Y (2021c). Comparison of measurements with and without reference in operational modal analysis method: A minaret example. *Journal of the Institute of Science and Technology,* 11(3), 2069-2078 (in Turkish).

Yurdakul M, Yılmaz F, Artar M, Can Ö, Öner E, Daloğlu AT (2021). Investigation of time-history response of a historical masonry minaret under seismic loads. *Structures,* 30, 265-276.

Challenge Journal of Structural Mechanics

Review

A discussion on the beam on elastic foundation theory

Tunay Uzbay Yelce [a], Erdem Balcı [a,*], Niyazi Özgür Bezgin [a]

[a] *Department of Civil Engineering, İstanbul University-Cerrahpaşa, 34320 İstanbul, Türkiye*

ABSTRACT

A railway track is a structural composure of many elements. Railway track analyses requires analyses for the interaction between these elements and the interaction between the track and the vehicle passing over the track. Various design models have been developed to simplify the analysis of railway tracks and to establish appropriate design criteria. Winkler's representation of the subgrade support as a continuous structure with independent springs was adapted to railway tracks by Zimmermann that further evolved into what is known as the Beam on Elastic Foundation Theorem (BOEF) today. A soil and structure interaction model based on BOEF theorem, frequently used by engineers to analyze the response of continuously supported structures on bearing layers, provides estimates for the distribution of deflections, bearing pressure, shears and moments along a continuously supported structure, such as a plate, by subgrade. This study aims to provide an in-depth and an explicit solution to the 4th order differential equation of BOEF and serve as a resource for those who are interested in this topic. This study will also present the historical development of the BOEF model, its use in railway track analysis, as well as its underlying assumptions in terms of structural behavior.

ARTICLE INFO

Article history:
Received 12 June 2022
Revised 1 October 2022
Accepted 31 October 2022

Keywords:
Beam on elastic foundation
Winkler
Talbot
Zimmermann
Railway track analysis

1. Introduction

Transportation engineering is a field of civil engineering dedicated to developing means and methods to ensure the presence of a number of people or a quantity of goods (number, quantity), at a certain location (distance), reliably at a given condition (comfort, serviceability, safety), within a certain period of time (time). Railway transportation is a significant symbol of industrial revolution and mechanization of humanity that allowed humanity to transport, greater number of people and greater amount of goods, to further distance within smaller time intervals, reliably, comfortably and safely. To ensure this advancement, early engineers designed heavier vehicles known as trains along specially designed routes known as railway tracks. The intense forces exerted on railway tracks by the trains and the response of the track to these forces posed a significant challenge for the early engineers to qualitatively assess and quantify. Absence of the necessary geotechnical knowledge, mechanical theories, thermodynamic theories and metallurgical knowledge at the time, posed even a greater challenge since the necessary theoretical framework to respond to the necessary design challenges was absent. While the development of the railway tracks was mostly based on experimental –trial and error- based research in its early days, it evolved further with mathematical analysis after the second half of the 1800's (Kerr 2003). A ballasted railway track consists of steel rails, rail fasteners, timber, concrete, composite or steel sleepers, ballast layer, sub-ballast layer, which is also known as protective layer and subgrade materials. Occasionally, railway tracks can also include rail pads and under sleeper pads if required. The interaction between these elements due to their different mechanical properties makes the understanding of track structural behavior challenging. It is found to be practical to consider each track component as a single structural unit, so that one may observe the interaction between these units through the definition of suitable boundary conditions and load transfer patterns (Sadeghi and Barati 2010). However, not only the interaction between the in-

* *Corresponding author*. E-mail address: erdembalci@outlook.com (E. Balcı)
ISSN: 2149-8024 / DOI: https://doi.org/10.20528/cjsmec.2023.01.004

ternal elements of the track effects the reaction of the track to the wheel forces; but also the interaction between the track and the vehicle passing over the track and the interaction between the soil and structure, also effect the response of the track as well (Balcı et al. 2022). Therefore, the interaction between the rail elements as well as train-track interaction and soil-track interaction has to be examined to analyze railway tracks and determine design criteria.

Two types of track were to be analyzed; longitudinal-tie track and cross-tie track. In the first one, the track is assumed to be supported continuously, while, in the latter track is supported discretely by cross-ties that are also known as sleepers. Fig. 1 shows the comparison of the longitudinal-tie tracks with the cross-tie tracks. Even though, discussions are made on the "continuity" assumption of a discretely supported railway track, deep rail sections over ties with limited tie spacing enhanced the justification of the application of the analyses of a continuously supported track to discretely supported track over time. Detailed discussions and historic development of these two types of tracks can be found in the related work (Kerr 1976).

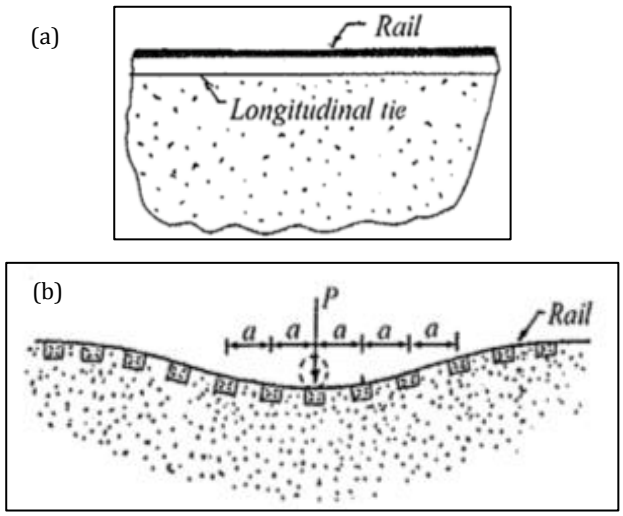

Fig. 1. Physical problem of: (a) Longitudinal-tie; (b) Cross-tie tracks (Kerr 2003).

Emil Winkler (1867) proposed a classical mathematical model to simplify the complex behavior of the soils by representing the soil with elastically deformable springs. Winkler's equation shed light on the analysis of railway tracks. Zimmermann's method idealized the railway track as a continuously supporting beam resting on a Winkler's foundation. However, in reality, the track is only supported at regular intervals (sleeper spacing), therefore, a discrete support model is developed. Heténi (1946) also developed some equations considering the boundary conditions in the railway track. These steps historically developed the beam on elastic foundation (BOEF) theory which is still in use to analyze railway tracks analytically. Finally, Talbot's experimental and analytical work showed the applicability of the BOEF theorem to the analyses of railway tracks (Kerr 2003).

This paper presents the development of the BOEF model to analyze longitudinal-tie and cross-tie tracks. The 4th order differential equation of the BOEF model is solved step by step so that one can obtain the necessary equations to determine deformation, moment, and shear forces. The shortcoming of the BOEF model is discussed. Finally, the continuous rail and discontinuous rail cases are compared according to the BOEF model.

2. Analysis of Railway Tracks

Railway tracks are complex structures to analyze due to fact that various components with different properties combine and interact with each other and they lay on a soil that is not fully homogenous. However, various researchers simplified the problem by making some assumptions and they developed mathematical models. The following explains the fundamental and practical models that are still in use and that led to the development of the BOEF theory.

2.1. Winkler model and subgrade modulus

Winkler developed a model to represent soil so that one can understand soil-track interaction better. Winkler Model describes the soil as linear, independent, elastic, closely located, and with an infinite number of springs. When a load is applied on a plate, the plate responds to this loading in relation to the mechanical qualities of the subgrade as well as the relative relation of the stiffness of the plate, which is the bending stiffness, with the compressive stiffness of the subgrade, which is a manifested quantity in relation to the bearing area of the plate and its bending stiffness. Fig. 2 is a general representation of a vertically loaded plate in three dimension, with a length L defined along the x-axis and width B defined along the y-axis with a bending rigidity of EI where E is the elastic modulus of the plate material and I is the moment of inertia of the plate along it's relevant bending axis. This plate is loaded by a generalized representation of distributed force defined as $f(x, y)$ which can be variable along the x and y axis. As a result of this applied force and in relation to the relative bending stiffness of this plate with respect to the compressive stiffness manifested in the subgrade, soil reaction denoted as $p(x, y)$ appears underneath the plate as a result of the soil deflection $w(x, y)$, which is not shown in this figure in order to maintain the clarity of the figure. Within the simplicity of the statement above, lies an important fundamental aspect of soil and structure interaction such that the soil reaction or in other words the substructure reaction is interrelated to the structural stiffness of the superstructure, which is the plate. The response of the supporting subgrade is not an independent and an isolated quality of the subgrade but a quality that varies with the stiffness of the supported structure. Emil Winkler, in his struggle to describe the generalized response of a structure supported by soil, represented the soil as a distribution of mechanically independent springs that elastically deform $w(x, y)$ under the pressure $f(x, y)$. Winkler's

model correlates the vertical contact pressure $p(x, y)$ at an arbitrary point in the underneath the plate to the corresponding vertical deformation $w(x, y)$ by using a coefficient, which is the "coefficient of vertical subgrade reaction" denoted by the term C in Eq. (1). Other symbols such as n_v and k_v, can also be used in liu of C, which is chosen to represent coefficient of vertical subgrade reaction in this study.

$$p(x, y) = C.w(x, y) \tag{1}$$

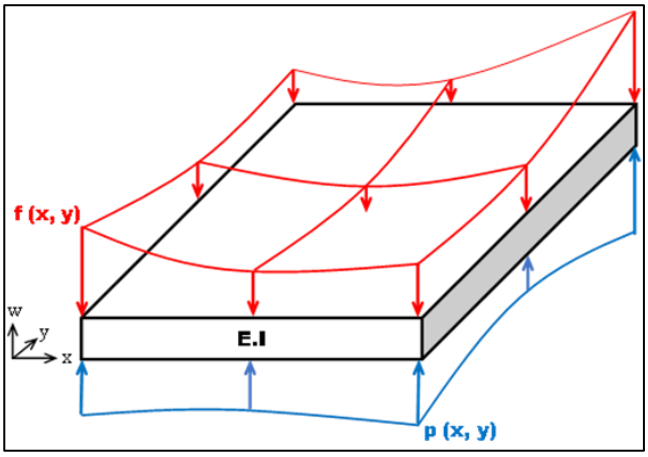

Fig. 2. Representation of a plate loaded by distributed load $f(x,y)$ and supported by the pressure generated by the subgrade $p(x,y)$.

The coefficient of vertical subgrade reaction is the ratio of the pressure at a particular point underneath a surface structure to the vertical deflection measured for that particular location (Terzaghi 1955). However, the coefficient of vertical subgrade reaction is not only affected by the subgrade material but also by the mechanical and geometrical properties of the superstructure. As its name implies, it is a particular reaction the subgrade gives to a loading by a particular structural element. In other words, the same subgrade would react differently to structures with different bending stiffness values and contact areas with the subgrade. Terzaghi (1955) investigated the change in stress distribution and the variation of the coefficient of vertical subgrade reaction with respect to the changes in superstructure qualities.

Winkler Model does not consider the vertical deformation in the soil springs located outside and underneath plate loading area due to shear transfer within the soil continuum (Skar et al. 2019). This leads to discontinuity of vertical deformation at the edges of the loaded area as shown in Fig. 3. Normally, the shear stresses would couple the deformation of adjacent springs and therefore there had to be a continuity in the deformation at the edges of the loading area (Worku 2009). However, shear stresses are not considered in the Winkler approach and thus, a spring undergoes the deformation independently of the neighboring springs (Horvath 1983a). Various attempts have been made to include the effect of shear stress. Some of them are Horvath (2002), Horvath (1983b), Kerr (1964), Reissner (1958), Worku (2009), and Onu (2000).

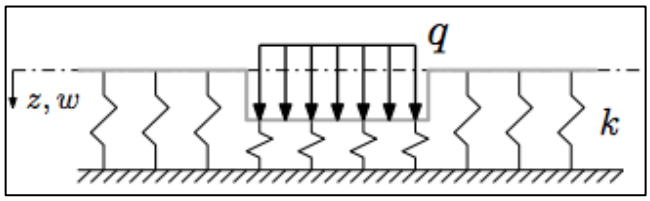

Fig. 3. Winkler soil model and the deformations (Skar et al. 2019).

Two-parameter model of Pasternak (1954) uses a second parameter k_2 to consider shear reactions of the foundation in addition to the first (Winkler) parameter k_1. Poddubny and Gordon (2021) concludes that shear rigidity vanishes when there is a sudden change in the physical and mechanical features of the foundation. Therefore negative effects caused by sudden changes in track should be considered in beams resting on elastic base models.

Two-parameter model of Vlasov and Leont'ev (1966) considers the depth of the soil layer under the foundation in addition to the shear forces and shear strain energy. While the foundation is modelled as an elastic layer, deflections within the foundation is restricted to an appropriate mode shape, $\varphi(z)$ by using constraints. However, a method for the determination of the parameter used for the decay of the stress distribution, γ is not proposed by the authors. Jones and Xenophontos (1977) correlated the γ and the displacement characteristics. Later, Vallabhan and Das (1988) determined γ as a function of the characteristics of the beam and the foundation.

Datta and Roy (2002), Wang et al. (2005), Balabušić et al. (2019), Tivari and Kuppa (2014), and Campione et al. (2021) evaluate and discuss the models established for the interaction between the structures and elastic foundations. Even though the assumptions it made, the Winkler Model is widely preferred among engineers due to its simplicity.

Application of the Winkler model, to railway tracks with discrete ties supports, has raised concern with regards to its applicability. However, Talbot's experimental work led by a team of railway experts, showed that the spacing between the discrete tie supports could be neglected and that the Winkler's continuously supported beam model can be applied to railway tracks as well (Kerr 2003). The depth of the rails in relation to the spacing of the ties is significant and therefore the rail acts as a deep-beam between the ties generating significant bending and shear stiffness thus providing continuity between the ties (Bezgin 2018).

Further studies are conducted to include different aspects of the elastic foundation-structure interaction. Abouelregal (2020) investigated the coupling between deformation and the temperature field caused by ultrafast laser heating for a beam resting on Winkler foundation. Froio et al. (2021) numerically modelled the moving load beam problem to effectively resolve the dynamic response of beams subjected to high velocity moving load. Thomas et al. (2020) investigated the applicability of almost incompressible elastomeric layers to the Winkler model by deriving a model that interpolates be-

tween the incompressible limits for thin elastic layers. Authors conclude that Poisson ratio and a compressibility parameter (related to layer's slenderness) are effective on the applicability of Winkler model. Aizikovich et al. (2016) examined the relationship between the interlayer thickness, gradient of elastic properties and the distribution of the contact stress under the beam.

2.2. Zimmermann model and track modulus

In the 1880s, Zimmermann applied the Winkler Model to the railway tracks by considering rails as constantly supported beams resting on the soil. Zimmermann adopted this approach in an attempt to fully comply the adoption of a continuously supported structure for a discretely supported railway track structure. While the supported part of the structure is the rails, the supporting parts are the sleepers/slab and the underlying layers. In the railway application, the rails are modeled as two parallel continuous beams constrained by the sleepers at regular intervals (sleeper spacing). Since the sleepers are supported by the underlying layers as well as the two sides of the sleeper, it is assumed that there is no deformation in the sleeper. The idea behind the Zimmermann method is to determine the supported area of a single beam and then transfer bearing areas into a continuously supported beam (Prakoso 2012).

In Fig. 4, l is the length of sleeper, m is the length of sleeper without support, b_1 is the width of sleeper, b is the width of the beam, and a is the sleeper spacing.

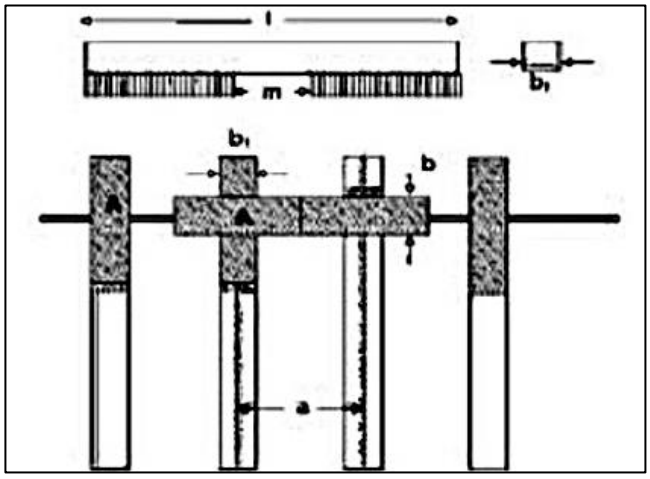

Fig. 4. Supporting areas in the Zimmermann model (Steidl 2007).

The supported area of one sleeper $F = (l - m) * b_1/2$ can be connected to the support areas of adjacent sleepers so that theoretical continuous rail support can be provided. The length of the transformed area is the sleeper spacing (a) and the width of it is the $b=F/a$. In order to include the response of the track, a single representative value is used in the model that has the same units of $Force/Length^3$ as in the coefficient of vertical subgrade reaction. However, in reality, the track consists of various elements with different responses. Therefore, a combined value representative value (C_{total}) of these elements must be used as shown in Eq. (2).

$$\frac{1}{C_{\text{total}}} = \frac{1}{C_{\text{railpad}}} + \frac{1}{C_{\text{ballast}}} + \frac{1}{C_{\text{subballast}}} + \frac{1}{C_{\text{subsoil}}} \tag{2}$$

The characteristic length of the structure can be determined through Eq. (3).

$$L = \sqrt{\frac{4.E.I}{b.C}} \tag{3}$$

The deflections and bending moments at a specific location can be calculated by using an influence factor of deflection (η) and influence factor of bending moment (μ), which are respectively shown in Eq. (4).

$$\eta = \frac{\sin\xi + \cos\xi}{e^{\xi}} \quad , \quad \mu = \frac{-\sin\xi + \cos\xi}{e^{\xi}} \tag{4}$$

where $\xi = x/L$, and "x" is the distance of the calculated point to the loading point and "L" is the characteristic length. The deflection diagram and moment diagram can be obtained by using the following Eqs. (5) and (6), respectively.

$$y = \frac{Q}{2.b.C.L}.\eta \tag{5}$$

$$M = \frac{Q.L}{4}.\mu \tag{6}$$

In his book "Beam on Elastic Foundations", Hetényi developed some equations for various boundary conditions in order to explain the response of the railway track to the vertical wheel forces (Hetényi 1946). The 2D model illustrates for a railway track, a single rail supported by the half width of the track. The vertical depth of the model represents deformation, moments, pressure, or the shear forces developed in the track.

A railway track lays on subgrade and reacts to the vehicle forces together with the subgrade. A "track modulus" term can explain the mutual deformation characteristics of the soil and the railway track, when the railway track is portrayed as a linear structure and its deflection characteristics investigated in two dimensions. Coefficient of vertical subgrade reaction is determined by the plate loading test by using a plate with high bending stiffness subjected to a concentrated loading. When one considers the loaded plate in three dimensions presented in Fig. 2 and represents this plate as a beam supported by an elastic subgrade as in Fig. 5a, one needs to portray the subgrade reaction on a unit length of the beam along x-axis by taking into account the width of the plate along the y-axis. When the same loading conditions are applied to the railway track, the unit force acting on a single rail can be found by multiplying the pressure (p) developed on the subgrade by half of the track width (B). Fig. 5b shows the pressures under a single rail and Eqs. (7) and (8) show the track modulus (u) related to the coefficient of vertical subgrade reaction and the width of the supported plate.

$$u = -\frac{p(x)*B}{y(x)} = -\frac{q(x)}{y(x)} \tag{7}$$

$$u = C \cdot B \tag{8}$$

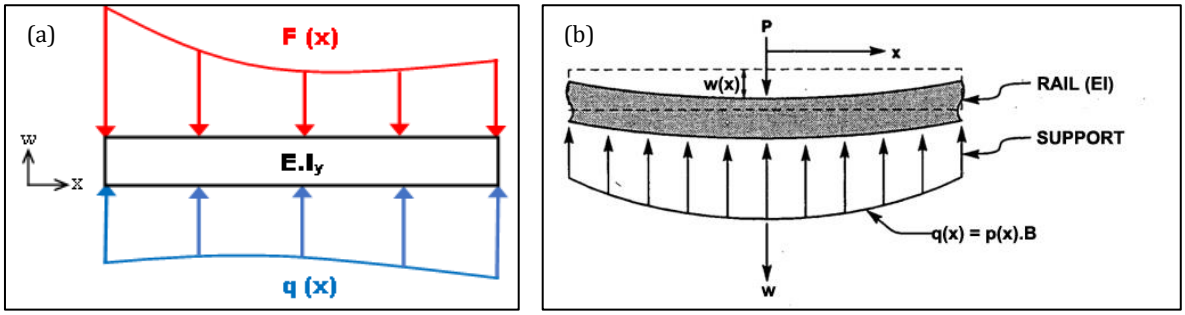

Fig. 5. (a) Two dimensional representation of a plate loaded in three dimensions as a beam; (b) A single rail supported by the half width of the track by Selig and Waters (1994).

The BOEF model offers a "track stiffness" concept which is determined by considering the rigidity of the rail and track modulus. The value of this parameter is highly effective on the general performance of the track (Balcı and Bezgin 2020) and the value of dynamic impact forces developed on the track. Bezgin (2017), Bezgin (2018), Wehbi and Bezgin (2019), and Bezgin and Kolukırık (2020) offers equations that correlates track stiffness and dynamic impact forces on railway tracks. Bezgin (2018) and Bezgin and Wehbi (2019) show that variation of the track stiffness over a specific length of a track leads to the occurrence of additional dynamic impact forces.

When a wheel force of *"P"* is exerted on the track, the maximum deformation w_{max}=$w(0)$ occurs at the point where the wheel contacts the track. Track stiffness (k) is the total track resistance per unit of deformation as shown in Eq. (9) and it is a lumped sum estimate of the total track resistance manifested along the railway track to a unit deformation exerted at a certain location on the rail.

$$k = \frac{P}{w_{\max}} \tag{9}$$

2.3. Discrete elastic support model

Considering that in reality, the rail is not continuously but discretely supported by the sleepers, further models are developed (Fig. 6).

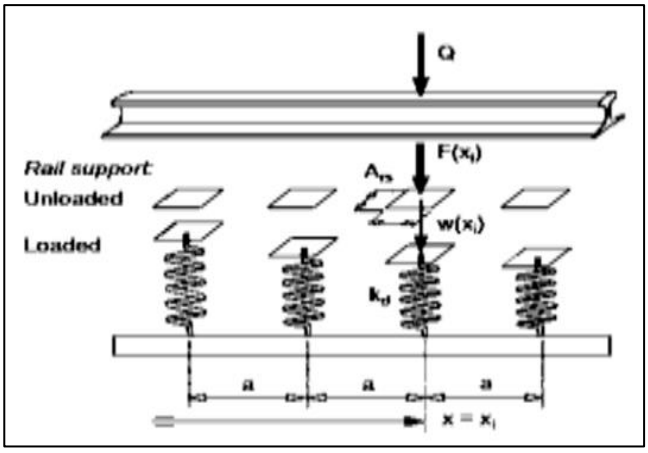

Fig. 6. Discrete support model by Esveld (2001).

When $F(x_i)$ is the vertical force at a i^{th} discrete support (x=x_i), A_{rs} is the effective rail support area, and $w(x_i)$ is the deformation at the point of interest, Winkler's model suggest the correlation shown in Eq. (10).

$$F(x_i) = C.A_{rs}.w(x_i) = k_d.w(x_i) \tag{10}$$

Thus, spring constant of the support is shown in Eq. (11).

$$k_d = C.A_{rs} \tag{11}$$

Spring constant in a homogenously supported track is the ratio of the wheel load to the sum of all measured significant deformations in the vicinity of the load as presented in Eq. (12).

$$k_d = \frac{Q}{\Sigma w} \tag{12}$$

However, spring constant (k_d) is the property of the support and is different than total spring constant of the track i.e. track stiffness (k_{total}). Eq. (13) shows the track stiffness and Eq. (14) correlates track stiffness to the support spring constant.

$$k_{\text{total}} = \frac{Q}{w_{\max}} \tag{13}$$

$$k_d = \frac{w_{\max}}{\Sigma w}.k_{\text{total}} \tag{14}$$

2.4. Talbot's work

One of the most significant contributions to the railway track analysis is made by Arthur Newell Talbot who ran the Engineering Experiment Station at the University of Illinois at Urbana-Champaign. Dr. Talbot has fundamental research, which has been directed since 1914 and summarized under "Stresses in Railroad Track" that forms a basis for railway engineering. Mechanical properties, mode of action, and resistances developed in the various track components under the dynamic forces of locomotives and cars moving at various speeds are investigated by Illinois (2022) to obtain authoritative information. Since the knowledge about the scientific nature of the stresses in railway tracks was very limited at the time the work was begun, the work provided an understanding of the interaction between track and rolling

stock and contributed to a more rational basis for railway track design. Fig. 7 shows the Talbot Committee loading device (1918) setup used to determine rail deflection profiles and the track modulus. There has been no attemp to improve Talbot's procedure until 1960s. Later, efforts have been made by analyzing track as a layered system using finite element analysis (Hay 1991).

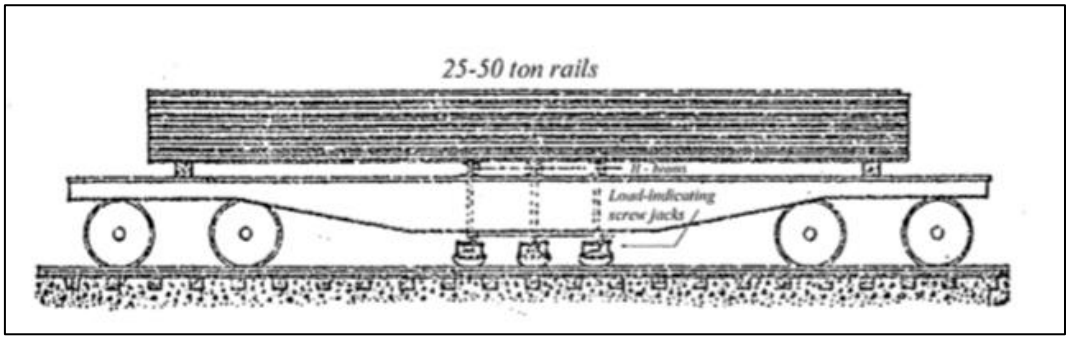

Fig. 7. Talbot Committee loading device (1918) for the analysis of rail deflection profile (Kerr 2003).

3. Analytical Solution of the BOEF Equation

The solution of the 4th-grade differential equation proposed by the BOEF model allows one to obtain the equations of deformation, moment, and shear forces. In this chapter, the solution to this equation will be presented. Eq. (15) correlates track pressure per unit length of track to track stiffness and track deflection.

$$q(x) = -u.y(x) \tag{15}$$

In this equation, u is the track modulus, $y(x)$ is the downward deflection of the foundation under the rail, and $q(x)$ is the downward force from the foundation on the rail per unit length of rail.

Fig. 8 shows a beam on elastic foundation and the forces applied to this beam. This beam is in equilibrium under these forces. The moment equation applied to the beam under the effect of bending is combined with the equilibrium equation. As a result, a differential equation is obtained.

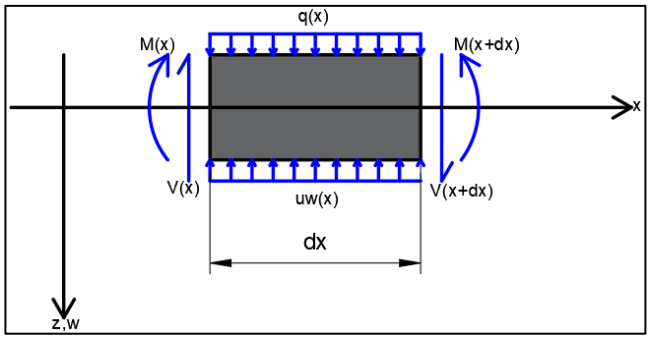

Fig. 8. The forces applied to the beam on elastic foundation.

Eq. (16) presents the equilibrium equation of the beam in Fig. 8 and solves for the variation of the shear force through Eqs. (17) and (18):

$$V - (V + dV) + u.y.dx - qdx = 0 \tag{16}$$

$$-dV + u.y.dx - qdx = 0 \tag{17}$$

$$\frac{dV}{dx} = u.y(x) - q(x) \tag{18}$$

where $V(x)$ is the shear force.

The shear force is obtained by taking the derivative of the moment. In order to write the above equation in terms of moment, the second degree derivative of the moment is taken in Eq. (19).

$$V(x) = \frac{dM(x)}{dx} \rightarrow \frac{dV(x)}{dx} = \frac{d^2M(x)}{dx^2} = u.y(x) - q \tag{19}$$

The moment equation of a beam under bending is shown below. In order to combine this equation with the above equation, the second derivative of the moment equation of the beam under bending is taken as shown in Eq. (20). As a result, a fourth degree derivative is obtained as in Eq. (21). Where E is modulus of elasticity and I is moment of inertia.

$$V(x) = \frac{dM(x)}{dx} \rightarrow \frac{dV(x)}{dx} = \frac{d^2M(x)}{dx^2} = u.y(x) - q \tag{20}$$

$$EI\frac{d^4y}{dx^4} = q(x) - u.y(x) \tag{21}$$

These equations can now be applied to railway tracks. Instead of a distributed vertical load, concentrated point loads (P) will be considered and load distribution will be disregarded such that $q(x)$ = 0. Hence, the general form of Eq. (21) is revised in Eq. (22) and it's special form for $q(x)$=0 is presented in Eq. (23).

$$\frac{d^4y(x)}{dx^4} + \frac{u.y(x)}{EI} = \frac{q(x)}{EI} \tag{22}$$

$$\frac{d^4y(x)}{dx^4} + \frac{u.y(x)}{EI} = 0 \tag{23}$$

After restating the differential equation for beam on elastic foundation, $y(x)$=e^{ax} is proposed as a solution for

$y(x)$. Taking the necessary derivatives of $y(x)$, Eqs. (24-28) are obtained.

$$y(x) = e^{ax} \tag{24}$$

$$y'(x) = a \times e^{ax} \tag{25}$$

$$y''(x) = a^2 \times e^{ax} \tag{26}$$

$$y'''(x) = a^3 \times e^{ax} \tag{27}$$

$$y''''(x) = a^4 \times e^{ax} \tag{28}$$

These equations are inserted into Eq. (23), leading to Eqs. (29-32).

$$y''''(x) + \frac{u.y(x)}{EI} = 0 \tag{29}$$

$$a^4 e^{ax} + \frac{u.e^{ax}}{EI} = 0 \tag{30}$$

$$a^4 e^{ax} = -\frac{u.e^{ax}}{EI} \tag{31}$$

$$a^4 = -\frac{u}{EI} = \frac{u}{EI} \times (-1) = \sqrt[4]{\frac{u}{EI}} \times \sqrt[4]{-1} \tag{32}$$

In the above equation, "a" is of fourth order and has 4 roots. To find these roots, complex numbers and polar representations of complex numbers are used. Eq. (33) presents the complex number representation of -1 and its polar representation in this complex number.

$$-1 = -1 + 0i = r(\cos\theta + i\sin\theta) \tag{33}$$

In polar representation of complex numbers, the distance of the complex number in the coordinate system from the origin is defined by "r".

De Moivre's Theorem (N^{th} Root Theorem) is used to find these roots. Eqs. (34-36) can be used to find the roots of an equation whose polar representation is known by applying De Movrie's Theorem.

$$a_{k'} = \sqrt[n]{r}(\cos(a) + i\sin(\alpha)) \tag{34}$$

$$\alpha = \frac{\theta + 2\pi k}{n} \tag{35}$$

The equation obtained using the above two formulas is shown below.

$$a_{k'} = \sqrt[n]{r}\left(\cos\left(\frac{\theta}{n} + \frac{2\pi k}{n}\right) + i\sin\left(\frac{\theta}{n} + \frac{2\pi k}{n}\right)\right) \tag{36}$$

Substitute of the n and r values in the equations above leads to Eqs. (37-41). The k value starts from 0 and goes up to the n-1 value where n = 4 and r = 1.

$$a_{k'} = \cos\left(\frac{\pi}{4} + \frac{2k\pi}{4}\right) + i\sin\left(\frac{\pi}{4} + \frac{2k\pi}{4}\right) \quad k = 0, 1, 2, 3 \tag{37}$$

$$a_{0'} = \cos\frac{\pi}{4} + i\sin\frac{\pi}{4} = \frac{\sqrt{2}}{2} + i\frac{\sqrt{2}}{2} \tag{38}$$

$$a_{1'} = \cos\left(\frac{\pi}{4} + \frac{2\pi}{4}\right) + i\sin\left(\frac{\pi}{4} + \frac{2\pi}{4}\right) = \cos\frac{3\pi}{4} + i\sin\frac{3\pi}{4} = -\frac{\sqrt{2}}{2} + i\frac{\sqrt{2}}{2} \tag{39}$$

$$a_{2'} = \cos\frac{5\pi}{4} + i\sin\frac{5\pi}{4} = -\frac{\sqrt{2}}{2} - i\frac{\sqrt{2}}{2} \tag{40}$$

$$a_{3'} = \cos\frac{7\pi}{4} + i\sin\frac{7\pi}{4} = \frac{\sqrt{2}}{2} - i\frac{\sqrt{2}}{2} \tag{41}$$

By simplifying the equations above, the following roots shown in Eqs. (42-45) are obtained.

$$a_{0'} = \frac{\sqrt{2}}{2} + i\frac{\sqrt{2}}{2} = \frac{2}{2\sqrt{2}} + \frac{2i}{2\sqrt{2}} = \frac{1+i}{\sqrt{2}} \tag{42}$$

$$a_{1'} = -\frac{\sqrt{2}}{2} + i\frac{\sqrt{2}}{2} = \frac{-1+i}{\sqrt{2}} \tag{43}$$

$$a_{2'} = -\frac{\sqrt{2}}{2} - i\frac{\sqrt{2}}{2} = \frac{-1-i}{\sqrt{2}} \tag{44}$$

$$a_{3'} = \frac{\sqrt{2}}{2} - i\frac{\sqrt{2}}{2} = \frac{1-i}{\sqrt{2}} \tag{45}$$

If these roots are substituted in Eq. (32) and rearrangement of the roots of this equation leads to the values shown in Eqs. (46-49) by considering Eq. (46).

$$a_0 = \sqrt[4]{\frac{u}{EI}} \times \frac{1}{\sqrt{2}}(1+i) = \sqrt[4]{\frac{u}{4EI}} \times (1+i) \tag{46}$$

$$a_1 = \sqrt[4]{\frac{u}{4EI}}(-1+i) \tag{47}$$

$$a_2 = \sqrt[4]{\frac{u}{4EI}}(-1-i) \tag{48}$$

$$a_3 = \sqrt[4]{\frac{u}{4EI}}(1-i) \tag{49}$$

All the equations above have $\sqrt[4]{\frac{u}{4EI}}$ as a common combined parameter. It is represented by β as shown in Eq. (50) for simplification.

$$\beta = \sqrt[4]{\frac{u}{4EI}} \tag{50}$$

Hence, Eqs. (51-54) present a_0, a_1, a_2 and a_3 in terms of β.

$$a_0 = \beta + \beta i \tag{51}$$

$$a_1 = -\beta + \beta i \tag{52}$$

$$a_2 = -\beta - \beta i \tag{53}$$

$$a_3 = \beta - \beta i \tag{54}$$

By writing the roots of "a" in terms of β in the $y(x) = e^{ax}$ equation, Eqs. (55-58) are acquired.

$$\text{for } a_0;\ \ y(x) = e^{a_0 x} = e^{\beta x + i\beta x} \tag{55}$$

$$\text{for } a_1;\ \ y(x) = e^{a_1 x} = e^{-\beta x + i\beta x} \tag{56}$$

$$\text{for } a_2;\ \ y(x) = e^{a_2 x} = e^{-\beta x - i\beta x} \tag{57}$$

$$\text{for } a_3;\ \ y(x) = e^{a_3 x} = e^{\beta x - i\beta x} \tag{58}$$

The solution that includes all solutions of a differential equation is called general solution. There are 4 integral constants for the general solution of the above equation. These constants are called A_1, A_2, A_3 and A_4. The general solution of this differential equation is shown in Eqs. (59-60).

$$y(x) = A_1.e^{a_0 x} + A_2.e^{a_1 x} + A_3.e^{a_2 x} + A_4.e^{a_3 x} \tag{59}$$

$$y(x) = A_1.e^{\beta x + i\beta x} + A_2.e^{-\beta x + i\beta x} + A_3.e^{-\beta x - i\beta x} + A_4.e^{\beta x - i\beta x} \tag{60}$$

Euler has a solution for the $e^{i\beta x}$ expansion called the Euler Formula shown in Eq. (61).

$$e^{i\beta x} = \cos(\beta x) + i\sin(\beta x) \tag{61}$$

Substituting Euler's formula in the general solution of the differential equation, Eq. (62) is obtained.

$$y = A_1.e^{\beta x}(\cos\beta x + i\sin\beta x) + A_2.e^{-\beta x}(\cos\beta x + i\sin\beta x) + A_3.e^{-\beta x}(\cos\beta x - i\sin\beta x) + A_4.e^{\beta x}(\cos\beta x - i\sin\beta x) \tag{62}$$

The above equation is simplified in Eq. (63). The new constant values in the equation are then denoted by C_n as shown in Eqs. (64-67).

$$y = e^{\beta x}[(A_1 + A_4)\cos(\beta x) + (A_1 i - A_4 i)\sin(\beta x)] + e^{-\beta x}[(A_2 + A_3)\cos(\beta x) + (A_2 i - A_3 i)\sin(\beta x)] \tag{63}$$

$$(A_1 + A_4) = C_1 \tag{64}$$

$$(A_1 i - A_4 i) = C_2 \tag{65}$$

$$(A_2 + A_3) = C_3 \tag{66}$$

$$(A_2 i - A_3 i) = C_4 \tag{67}$$

Eq. (68) presents the general solution for displacement is as follows.

$$y(x) = e^{\beta x}[C_1.\cos(\beta x) + C_2.\sin(\beta x)] + e^{-\beta x}[C_3.\cos(\beta x) + C_4.\sin(\beta x)] \tag{68}$$

Following the attainment of this general solution is obtained, one can apply its particular solution to railway engineering. One can consider infinite beam or rail loaded with a singular P force at $x = 0$. C_1 and C_2 terms lead to infinite deflection (y) when $x \to \infty$ at the right of the beam. This is contrary to the boundary conditions of the beam. When $C_1 = C_2 = 0$, only half of the equation remains and the deflection is zero when $x \to \infty$, which is in agreement with the boundary conditions. Such being the case, Eq. (69) represents the special form of Eq. (68) when applied to an continous railway track supported by subgrade. The derivatives of this written equation are shown in Eqs. (70-72).

$$y(x) = e^{-\beta x}[C_3\cos(\beta x) + C_4\sin(\beta x)] \tag{69}$$

$$y'(x) = \beta e^{-\beta x}[(-C_3 + C_4)\cos(\beta x) + (-C_3 - C_4)\sin(\beta x)] \tag{70}$$

$$y''(x) = \beta^2 e^{-\beta x}[-2C_4\cos(\beta x) + 2C_3\sin(\beta x)] \tag{71}$$

$$y'''(x) = \beta^3 e^{-\beta x}[2(C_3 + C_4)\cos(\beta x) + (-C_3 + C_4)\sin(\beta x)] \tag{72}$$

The singular force P acting on the rails is applied from the x=0 point. Eq. (68) applies for the whole track except the point that load is applied. The deflection and bending moment at the load P is not known. However, the shear force at that point is known and can be obtained by taking the derivative of the moment variation along the supported track. Since the point load P is symmetrically supported by a homogenenous track, the maximum value of the shear forces to the immediate right and left of the location where the load P is acting is $P/2$. Hence, Eq. (73) presents the shear force $V(x)$ and it has maximum value at x=0.

$$V(x) = \frac{dM(x)}{dx} = EI.y'''(x) \to for\ x = 0, V_{\max} = \frac{P}{2} \tag{73}$$

Substituting the third derivative of the displacement in this equation, Eq. (74) is obtained.

$$V(x) = EI(\beta^3 e^{-\beta x}[2(C_3 + C_4)\cos(\beta x) + 2(-C_3 + C_4)\sin(\beta x)]) \tag{74}$$

Eq. (75) results for $x = 0$, where $C_3 + C_4$ is presented in Eq. (76).

$$2EI\beta^3(C_3 + C_4) = \frac{P}{2} \tag{75}$$

$$C_3 + C_4 = \frac{P}{4EI\beta^3} \tag{76}$$

The derivative of the beam's displacement function gives the slope. Since it is a symmetrical system, the slope at $x = 0$ is equal to 0. In this case, $y' = 0$ shown in Eq. (77) and solved through Eqs. (78-79).

$$y'(x) = \beta e^{-\beta x}[(-C_3 + C_4)\cos(\beta x) + (-C_3 - C_4)\sin(\beta x)] = 0 \quad (77)$$

$$\beta e^{0}[(-C_3 + C_4)\cos(0) + (-C_3 - C_4)\sin(0)] = 0 \quad (78)$$

$$\beta(-C_3 + C_4) = 0 \quad (79)$$

β is a fourth-degree root. So this cannot be equal to 0 and hence the part in parentheses must be equal to 0 as shown in Eq. (80).

$$C_4 - C_3 = 0 \rightarrow C_3 = C_4 = C \quad (80)$$

If the above equations are combined, Eq. (81) is obtained where *"u"* is presented in Eq. (82) and C_3 and C_4 are presented in Eq. (83).

$$2C = \frac{P}{4EI\beta^3} \rightarrow C = \frac{P}{8EI\beta^3} \quad (81)$$

$$u = 4EI\beta^4 \quad (82)$$

$$C_3 = C_4 = C = \frac{P\beta}{2u} \quad (83)$$

As a result of the calculations, the displacement formula on the railway lines has been simplified in Eqs. (84) and (85).

$$y(x) = e^{-\beta x}[C_3\cos(\beta x) + C_4\sin(\beta x)] \quad (84)$$

Since $C_3 = C_4$;

$$y(x) = e^{-\beta x}[C_3\cos(\beta x) + C_3\sin(\beta x)] \quad (85)$$

By placing the equation in C_3 brackets into the equation above, one obtains the Eqs. (86) and (87).

$$y(x) = C_3 e^{-\beta x}[\cos(\beta x) + \sin(\beta x)] \quad (86)$$

Eq. (87) is the general formula of the displacement under the rail on the railway lines.

$$y(x) = \frac{P\beta}{2u} e^{-\beta x}[\cos(\beta x) + \sin(\beta x)] \quad (87)$$

1st, 2nd and 3rd order derivatives of the above displacement equation when multiplied by *EI*, gives the slope, moment and shear distribution along the track.

Taking the 1st derivative of the displacement function through Eqs. (88) and (89) results in Eq. (90) for the general equation for the variation of the slope along the deflected track:

$$y'(x) = -\frac{P\beta^2}{2u}(\cos(x\beta) + \sin(\beta x)) + \frac{P\beta^2}{2k} e^{-\beta x}(-\beta\sin(\beta x) + \cos(\beta x)\beta) \quad (88)$$

$$\frac{P\beta^2}{2u} e^{-\beta x}(-\cos(\beta x) - \sin(\beta x) - \sin(\beta x) + \cos(\beta x)) \quad (89)$$

$$y'(x) = \frac{P\beta^2}{2u} e^{-\beta x}(-2\,sin(\beta x)) \quad (90)$$

Second derivative of the deflection equation results in the general equation of moment along the track:

$$y''(x) = -\frac{P\beta^3}{2u} e^{-\beta x}(-2\sin(\beta x)) + \frac{P\beta^3}{2u} e^{-\beta x}(-2\cos(\beta x)) \quad (91)$$

$$y''(x) = \frac{P\beta^3}{2u} e^{-\beta x}(2\sin(\beta x) - 2\cos(\beta x)) = \frac{P\beta^3}{u} e^{-\beta x}(\sin(\beta x) - \cos(\beta x)) \quad (92)$$

$$M(x) = -EIy''(x) \rightarrow EI = \frac{u}{4\beta^4} \rightarrow -\frac{u}{4\beta^4}\frac{P\beta^3}{u} e^{-\beta x}(\sin(\beta x) - \cos(\beta x)) \quad (93)$$

$$M(x) = \frac{P}{4\beta} e^{-\beta x}(\cos(\beta x) - \sin(\beta x)) \quad (94)$$

The 3rd derivative of the deflection equation results in the general equation of shear force along the track:

$$y'''(x) = -\frac{P\beta^4}{u} e^{-\beta x}(\sin(\beta x) - \cos(\beta x)) + \frac{P\beta^4}{u} e^{-\beta x}(\cos(\beta x) + \sin(\beta x)) \quad (95)$$

$$y'''(x) = \frac{P\beta^4}{u} e^{-\beta x}(-\sin(\beta x) + \cos(\beta x) + \cos(\beta x) + \sin(\beta x)) = \frac{P\beta^4}{u} e^{-\beta x} \times 2 \times \cos(\beta x) \quad (96)$$

$$V(x) = \frac{dM(x)}{dx} = -EI.w'''(x) = -\frac{u}{4\beta^4}\frac{P\beta^4}{u} e^{-\beta x} \times 2 \times \cos(\beta x) \quad (97)$$

$$V(x) = \frac{P}{2} e^{-\beta x}\cos(\beta x) \quad (98)$$

The pressure is obtained in Eq. (101) by multiplying the track deflections by k as shown in Eqs. (99) and (100).

$$P(x) = u.w(x) \quad (99)$$

$$w(x) = y = \frac{P\beta}{2u} e^{-\beta x}(\cos(\beta x) + \sin(\beta x)) \quad (100)$$

$$P(x) = u.w(x) = u\frac{P\beta}{2u} e^{-\beta x}(\cos(\beta x) + \sin(\beta x) = \frac{P\beta}{2} e^{-\beta x}(\cos(\beta x) + \sin(\beta x) \quad (101)$$

Maximum bending moment, maximum shear stress, and maximum intensity of pressure against the rail are shown in Eqs. (102-104).

$$M_{\max} = P(\frac{EI}{64u})^{1/4} \quad (102)$$

$$V_{\max} = -P/2 \tag{103}$$

$$P_{\max} = P\left(\frac{u}{64EI}\right)^{1/4} \tag{104}$$

The "u" term used in the equations is used to describe "track modulus". Eq. (105) shows the relation between track stiffness (k) and track modulus (u).

$$k = \frac{2u}{\beta} = \sqrt[4]{64.E.I.u^3} \tag{105}$$

Track stiffness values can vary highly from site to site. In Li and Berggren's work (2010), 32 kN/mm track stiffness is evaluated as "soft track", whereas 78 kN/mm is described as "normal track" and 172 kN/mm is "stiff track".

Minimization of the energy released by materials during the deformation (called elastic strain energy) can be used to find optimum track stiffness. Wehbi and Musgrave (2017) carried out the experiments for British Railways and concluded that a minimum of elastic strain energy can be reached while track stiffness goes to 160 kN/mm. However, it is seen that the effect of the strain energy is reduced after the track stiffness of 45 kN/mm. Therefore, the optimum value can be chosen as 45 kN/mm. Lopez Pite et al. (2004), on the other hand, suggests optimum track stiffness of 70-80 kN/mm by optimizing maintenance costs and dissipated energy. However, higher track stiffness values can be seen depending on the support conditions. For instance, the stiffness of the ballasted track laying on the bridge is found to be 109 kN/mm and the ballastless track in the tunnel is found to be 203 kN/mm in the measurements taken by Zhao et al (2015) from a part of the Shanghai-Kunming railway line.

While the track modulus of a soft track can be low as 7 MPa, stiff tracks can be high as 80 MPa. When the optimum track stiffness values stated in the literature is considered, the optimum values of track modulus should be between 20 to 45 MPa when UIC 60 rail type is used.

4. Shortcomings of the BOEF Model

While the BOEF model offers a practical and simple solution for the analysis of the railway tracks, there are some points where it deviates from the real track conditions because of the assumptions it make. Since the BOEF model is developed based on the Winkler model, those shortcomings are valid for BOEF as well.

According to the deformation values calculated using the BOEF model, the maximum deformation value occurs under the point where the wheel contacts the track. As one moves away from this point, the deformation gradually decreases. If the wheel is at a certain distance from the point of contact with the track, there is a reverse deformation due to the tensile forces on the track. Track deformations for different track bed moduli are shown in Fig. 9(a) and moments are shown in Fig. 9(b). As the track stiffness decreases, the maximum deformation in the track increases together with the value of reverse deformation. The reverse deformation means the compressive stress must be negative at the points of interest. In reality, however, such a tensile force does not occur in the subgrade. In fact, the formation of negative stress is not physically possible because the ballast layer cannot absorb the tensile force (Esveld 2001). Hence, the maximum deformation value offered by the BOEF equations under the single wheel force is different than the actual deformation value. This should be taken into account during design. In order to overcome this problem, deformation calculations can be balanced by using some optimization programs.

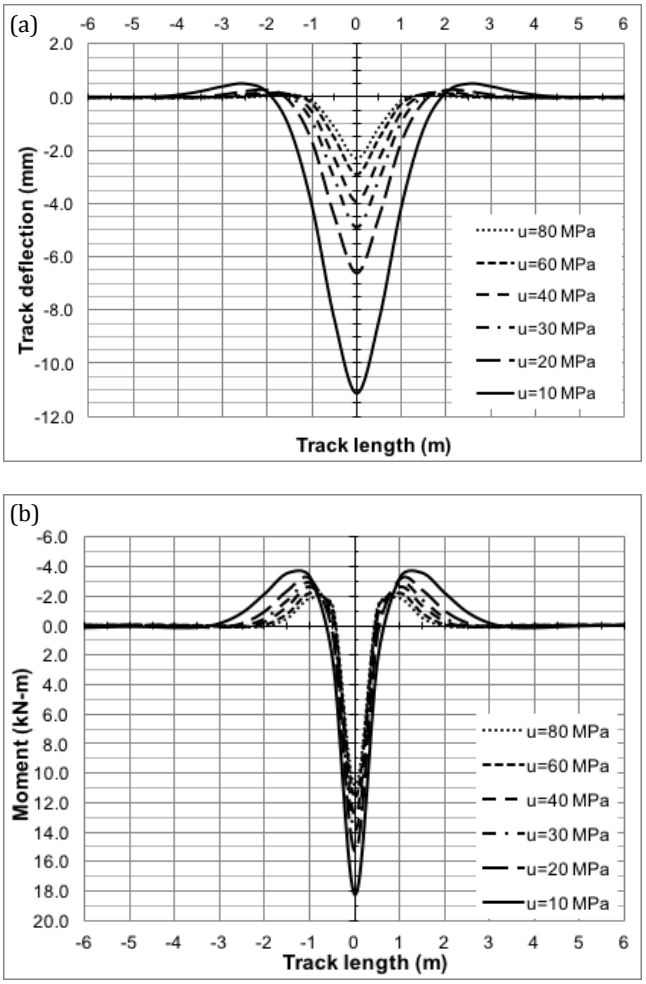

Fig. 9. a) Track deflections;
b) Moments for various track bed moduli values.

This situation is similar to a simple beam calculation shown in Fig. 10. While negative moments occur at the endpoints of a beam with fixed supports, a maximum positive moment occurs in the span. Being constrained at the endpoints ensures that the beam is supported at the ends and this reduces the moment in the mid-span. However, one can assume as the supports at the ends of this beam can be loosened, its bending stiffness can be reduced, and the same beam may become a simply supported beam. In this case, since the beam cannot receive a response from the endpoints, a negative moment does not occur here. The negative moments occurring at the

endpoints in the first case are now collected in the middle span and the maximum positive moment in the middle span increases. In Fig. 10, the moments occurring in a fixed beam and a simply supported beam are presented. Likewise, in the railway track example, the assumed negative moments to occur at the ends of the deformation curve or a certain percentage of it be added to the point where the wheel contacts the track, i.e. the point where the maximum positive moment occurs. According to one source, the regions where rail is raised above ground level must be pulled down by the ground at 4% of the maximum pressure under load (Hartog 1987). Since the ground cannot actually pull onto a track, a part of the positive moment shown in Fig. 10 will likely collect along the negative moment region. Kerr, in his book highlights his particular research on the topic and concentrates on the variations of the moments and deflections along the uplifted track region (Kerr 2003) and suggests the amount of variations along the actual track with regards to the estimated behavior by the BOEF theorem.

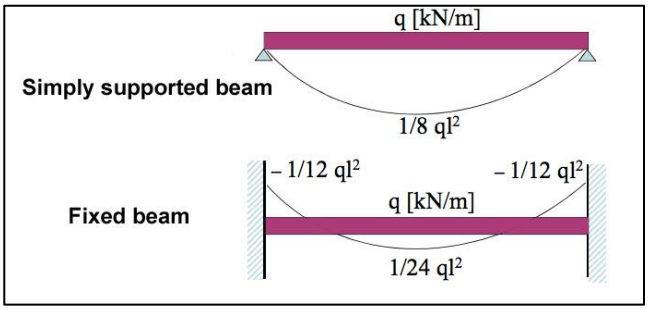

Fig. 10. Moments in the fixed and simply supported beam.

On the other hand, although the BOEF model assumes that the track is constantly supported, this support is impaired at specific points where there are geometric profile changes, such as insulated rail joints and turnouts. In such cases, the modified BOEF should be used in calculations. Kerr (2003) offered some equations for the two-axle trucks near a poorly maintained joint. Poorly maintained joint means an area where bending moments are not transferred to the adjacent rail and thus, neighboring rails act independently as shown in Fig. 11. Eq. (106) shows the deformation and Eq. (107) shows the bending moments in this case.

$$w(x) = \frac{P\beta}{2k}\{4e^{-\beta x}\cos\beta x + e^{-\beta|x-b|}[\cos\beta|x-b| + \sin\beta|x-b|] + +e^{-\beta|x+b|}[\cos\beta|x+b| + \sin\beta|x+b|] + 2e^{-\beta|x+b|}[\cos\beta(x-b) - \sin\beta(x-b)]\} \quad (x>0) \quad (106)$$

$$M(x) = -EIw''(x) = -\frac{P}{4\beta}\{4e^{-\beta x}\sin\beta x + e^{-\beta|x-b|}[\sin\beta|x-b| - \cos\beta|x-b|] + e^{-\beta|x+b|}[\sin\beta|x+b| - cos\beta|x+b|] + 2e^{-\beta|x+b|}(\cos\beta b - \sin\beta b)(\cos\beta x + \sin\beta x)\} \quad (107)$$

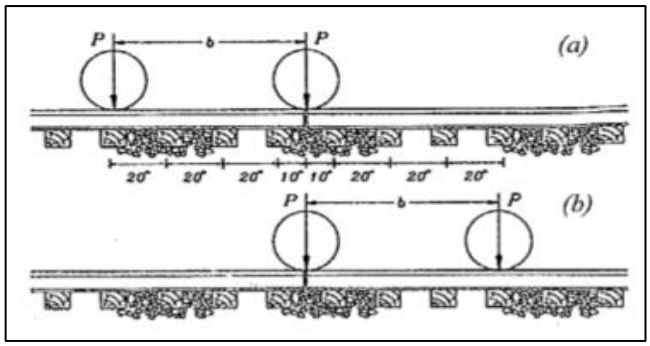

Fig. 11. 2-axle truck positions near a poorly maintained joint represented by Kerr (2003).

5. Comparison of Continuous Rail and Rail End Cases

All calculations within this chapter are done for UIC 60 rail type. Figs. 12 and 13 compare the deformations and moments of a continuous rail and a rail-end case under a 2-axle bogie with an axle spacing of 2 m, UIC 60 rail profile, and k=120 kN/mm track stiffness. One can see that maximum track deformation is the highest when the wheel contacts the rail-end point. The deformation under the second wheel is also relatively higher compared to the deformation of the continuous rail. The maximum negative bending moment occurs between the neighboring wheels and is higher for the rail-end case. However, the moment equals to zero at the point where rail is ended. The first cross-tie near a rail joint is subjected to the rail seat force that is at least three times larger than the force applied to the normal ties without joint or far away from the joint (Kerr 2003).

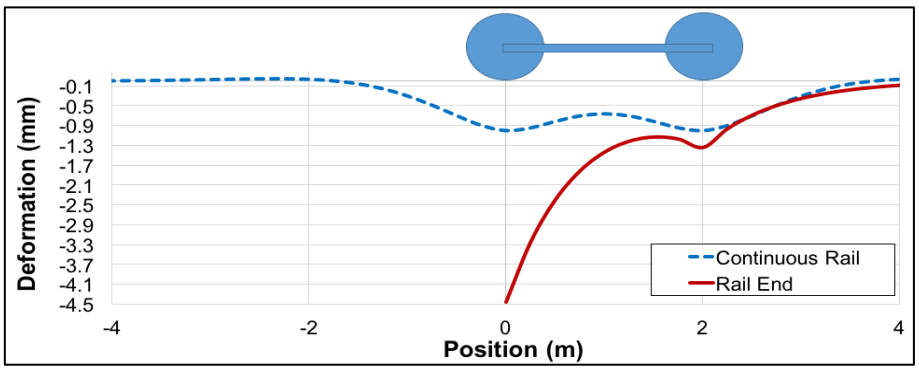

Fig. 12. Comparison of the deformations for continuous rail and rail-end.

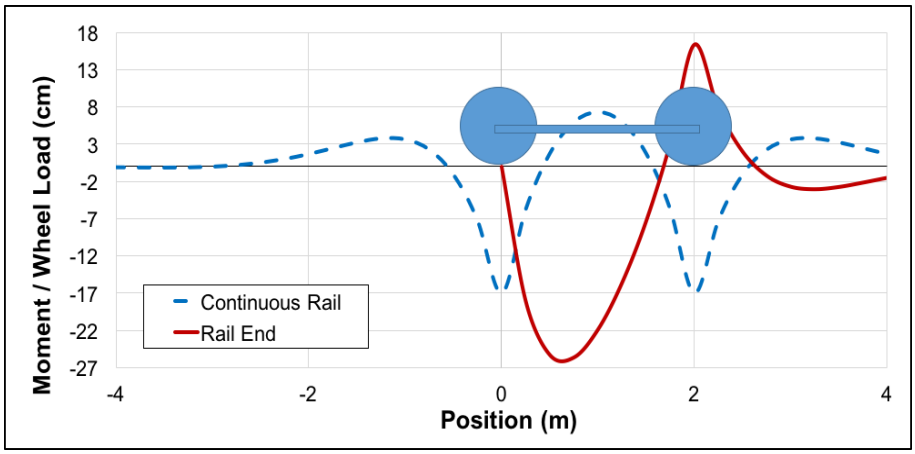

Fig. 13. Comparison of the moments for continuous rail and rail-end.

Figs. 14(a) and 14(b) show the deformations of continuous rail and the rail-end case for track stiffness varying between k=20 kN/mm and k=120 kN/mm. While track stiffness changes from k=20 kN/mm to k=120 kN/mm, the ratio of the maximum deformation of the continuous rail to the rail-end case varies between 3.6 and 4.4, respectively. In other words, the stiffness of the discontinuous track is about 25% of the stiffness of the continuous track on average.

Figs. 15(a) and 15(b) represent the ratio of the moments to the wheel loads for continuous rail and rail-end cases for different track stiffness values. While track stiffness varies between k=20 kN/mm and k=120 kN/mm, the ratio of the maximum negative moment of the continuous rail to the rail-end case is approximately 1.5 for all track stiffness values. These findings show that rail requires more bending capacity in rail joint case and also dynamic impact factor can be higher due to this abrupt variations in track stiffness, which causes the track to deteriorate more throughout its service life.

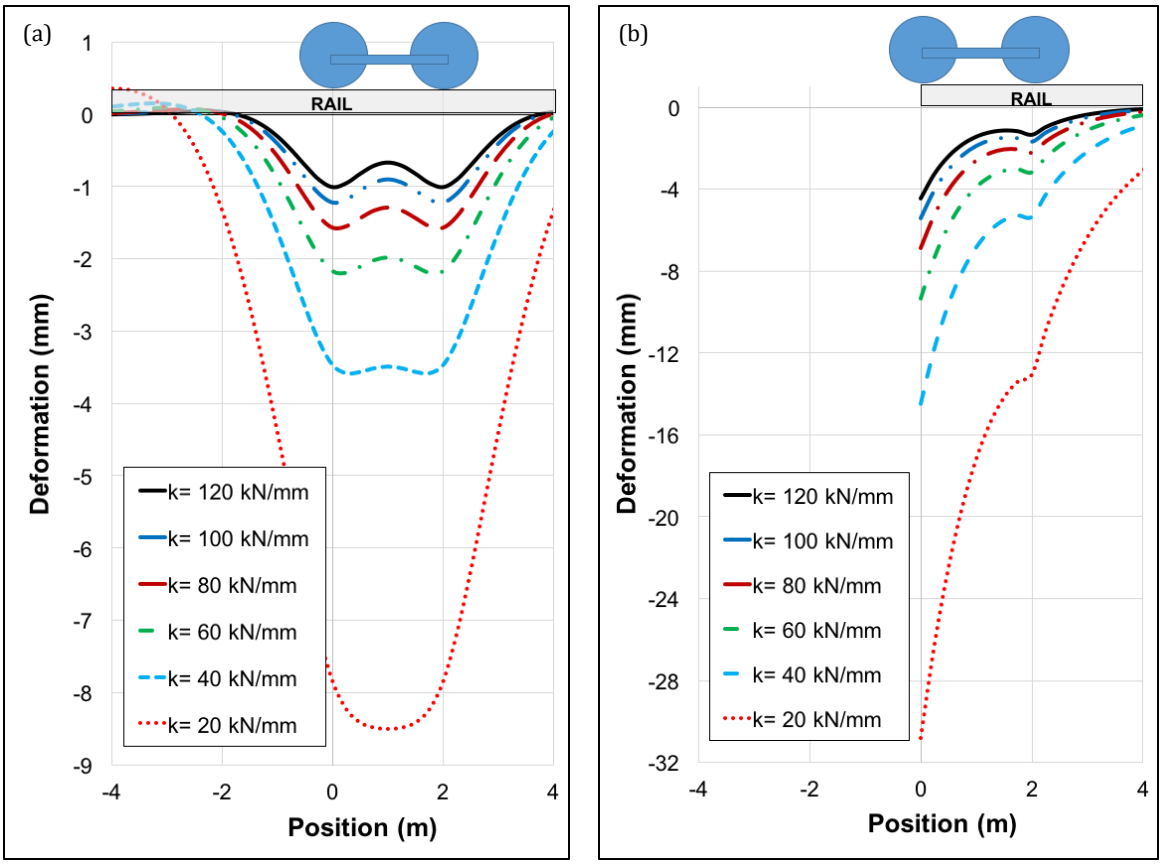

Fig. 14. Deformations at a) continuous rail and b) rail-end for various track stiffness values.

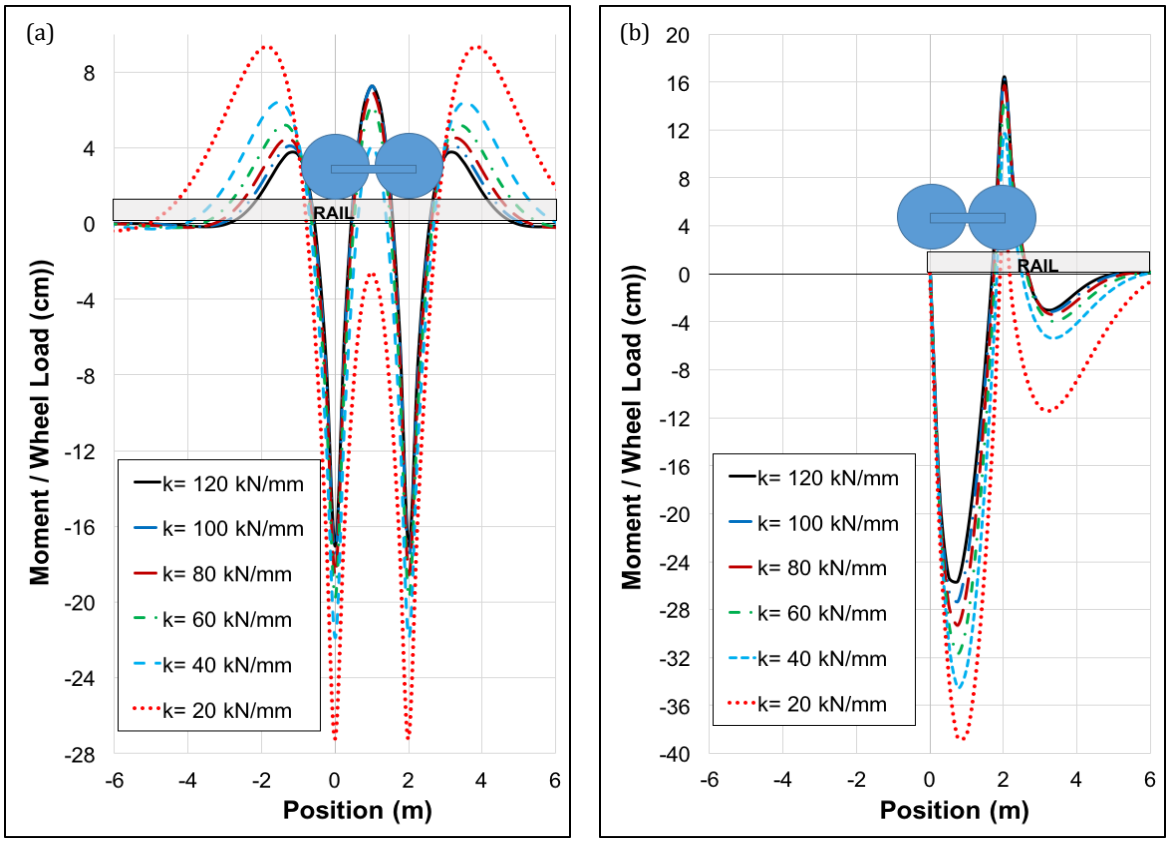

Fig. 15. Moments at a) continuous rail and b) rail-end for various track stiffness values.

6. Conclusions

Development of a mathematical analysis for design of railway tracks became necessary for better understanding and assessment of their responses towards the end of 19th Century. Since railway tracks are directly supported by the subgrade and they are a union of different structural elements, both the analysis of the interaction of the subgrade with the structure and the mutual interaction of the railway components should be well understood for the analysis of the railway tracks. There is also an interaction between the track superstructure and the train as it is directly exposed to train wheel forces. This study, presented an insight into the historic development of the BOEF approach in railway track analyses and provides a mathematical perspective into the development of the response parameters of the railway track.

Although analyzes using the finite element method are quite common today, these analyzes require plenty of time, computational power and also detailed material and geometrical knowledge about the properties of the track's components. For this reason; deformation, moment and shear force calculations can be still made using the BOEF model. These analysis equations are obtained as a result of solving the 4th order differential equation presented by the BOEF model. The step-by-step solution of this differential equation is presented in this study. Afterwards, the difference between the BOEF model and the real railway track case due to the assumptions made are discussed. The BOEF theory, with its explicit nature, continues to support engineers and researchers in their assessment and understanding of railway track mechanics.

Acknowledgements

None declared.

Funding

The authors received no financial support for the research, authorship, and/or publication of this manuscript.

Conflict of Interest

The authors declared no potential conflicts of interest with respect to the research, authorship, and/or publication of this manuscript.

References

Abouelregal AE (2021). Thermoelastic fractional derivative model for exciting viscoelastic microbeam resting on Winkler foundation. *Journal of Vibration and Control*, 27(17-18), 2123-2135.

Aizikovich SM, Mitrin BI, Seleznev NM, Wang YC, Volkov SS (2016). Influence of a soft FGM interlayer on contact stresses under a beam on an elastic foundation. *Structural Engineering and Mechanics: An International Journal*, 58(4), 613-625.

Arnold K (2003). Fundamentals of Railway Track Engineering. Simmons-Boardman Books, Inc., Nebraska.

Balabušić M, Folić B, Ćorić S (2019). Bending the foundation beam on elastic base by two reaction coefficient of Winkler's subgrade. *Open Journal of Civil Engineering*, 9, 123-134.

Balcı E, Bezgin NÖ, Wehbi M (2022). Variation of track response to wheel forces with bogie axle spacing: Apparent track stiffness and its influence on dynamic impact forces on railway tracks. *Transportation Research Record*, 2676(4), 570-588.

Balcı E, Bezgin N (2020). Hat esneme direncinin hat performansı üzerindeki etkileri. *Demiryolu Mühendisliği*, 11, 75-85. (in Turkish)

Balcı E, Yalçın E, Yelce TU, Bezgin NÖ (2021). Bir demiryolu hattının birim esneme direnci üzerinde etkisi olan mekanik ve geometrik niteliklerin incelenmesi. *Mühendislik Bilimleri ve Tasarım Dergisi*, 9(4), 1408-1423. (in Turkish)

Bezgin NÖ (2017). Development of a new and an explicit analytical equation that estimates the vertical dynamic impact loads of a moving train. *Procedia Engineering*, 189C, 2-10.

Bezgin NÖ (2018). An insight into design of prefabricated and prestressed concrete monoblock railway ties for service loads. *Challenge Journal of Structural Mechanics*, 4(4), 126-136.

Bezgin NÖ (2018). Application of a new concept and a method to estimate the vertical impact forces on railway tracks because of track profile irregularities. *97th Annual Meeting of the Transportation Research Board,* Washington, D.C.

Bezgin NÖ (2018). Proposal of a new analytical method to estimate the vertical impact forces on railway tracks because of changes in track profile and track stiffness. *Proceedings of the 5th International Conference on Road and Rail Infrastructure CETRA*, Zadar, Croatia, 837–845.

Bezgin NÖ, Kolukırık C (2020). Applications and estimate comparisons of bezgin–kolukırık equations for dynamic impact forces because of wheel flats with numerical analysis estimates and instrumented track measurements. *Transportation Research Record: Journal of the Transportation Research Board*, 2674(10), 199- 214.

Bezgin NÖ, Wehbi M (2019). Advancement and application of the bezgin method to estimate the effects of stiffness variations along railways on wheel forces. *Transportation Research Record: Journal of the Transportation Research Board*, 2673(7), 248-264.

Campione G, Cannella F, Zizzo M (2021). Flexural response of reinforced concrete beam on elastic foundation under vertical load and bending moment: review of existing methods and proposed new method. *Practice Periodical on Structural Design and Construction*, 26(2), 04021007.

Chandler TG, Vella D (2020). Validity of Winkler's mattress model for thin elastomeric layers: beyond Poisson's ratio. *Proceedings of the Royal Society A*, 476(2242), 20200551.

Datta SC, Roy R (2002). A critical review on idealization and modeling for interaction among soil – foundation - structure system. *Computers and structures*, 80(2-21), 1579-1594.

Esveld C (2001). Modern Railway Track (vol. 385). Zaltbommel: MRT-productions.

Froio D, Verzeroli L, Ferrari R, Rizzi E (2021). On the numerical modelization of moving load beam problems by a dedicated parallel computing FEM implementation. *Archives of Computational Methods in Engineering*, 28(4), 2253-2314.

Hartog DPJ (1987) Advanced Strength of Materials. Dover Publications Inc., New York.

Hay WW (1991). Railroad Engineering (vol. 1). John Wiley & Sons.

Hetenyi M (1946). Beams on Elastic Foundation: Theory with Applications in the Fields of Civil and Mechanical Engineering (vol. 16). University of Michigan Press, Ann Arbor, MI.

Horvath JS (1983a). Modulus of subgrade reaction: new perspective. *Journal of Geotechnical Engineering*, 109(12), 1591–1596.

Horvath JS (1983b). New subgrade model applied to mat foundations. *Journal of Geotechnical Engineering,* 109(12), 1567-1587.

Horvath JS (2002). Basic SSI Concepts and Applications Overview. Soil-Structure Interaction Research Project, Report No. CGT-2002-2, Manhattan College, School of Engineering, New York.

Illinois, Railtec University of Illinois at Urbana-Champaign (2022). Arthur Newell Talbot (1857-1942). https://railtec.illinois.edu/arthur-newell-talbot/

Jones R, Xenophontos J (1977). The Vlasov Foundation Model. *International Journal of Mechanical Sciences,* 19, 317-323.

Kerr AD (1964). Elastic and viscoelastic foundation models. *Journal of Applied Mechanics*, *ASME*, 25(80), 491-498.

Kerr AD (1976). On the stress analysis of rails and ties. *Proceedings of the American Railway Engineering Association*, 78.

Kerr AD (2003). Fundamentals of Railway Track Engineering. Simmons–Boardman Publishing Corporation.

Li MXD, Berggren EG (2010). A study of the effect of global track stiffness and its variations on track performance: simulation and measurement. *Proceedings of the Institution of Mechanical Engineers, Part F: Journal of Rail and Rapid Transit*, 224(5), 375-382.

Lopez Pita A, Teixeira PF, Robuste F (2004). High speed and track deterioration: the role of vertical stiffness of the track. *Proceedings of the Institution of Mechanical Engineers, Part F: Journal of Rail and Rapid Transit*, 218(F1), 31-40.

Onu G (2000). Shear effect in beam finite element on two-parameter elastic foundation. *Journal of Structural Engineering,* 126(9).

Pasternak PL (1954). Fundamentals of the new method of calculating foundations on elastic base using two bed coefficients. *Gosstroyizdat*, 56.

Poddubny AA, Gordon VB (2021). Dynamic loading of the rod at a sudden change of elastic foundation structure. *IOP Conference Series: Materials Science and Engineering*. IOP Publishing, 042076.

Prakoso PB (2012). The basic concepts of modelling railway track systems using conventional and finite element methods. *Info-Teknik*, 13(1), 57-65.

Reissner E (1958). A note on deflections of plates on a viscoelastic foundation. *Journal of Applied Mechanics*, *ASME*, 25(80), 144-145.

Sadeghi J (1997). Investigation of Characteristics and Modelling of Railway Track System. *Ph.D. thesis*, University of Wollongong, Australia.

Sadeghi J, Barati P (2010). Evaluation of conventional methods in analysis and design of railway track system. *International Journal of Civil Engineering*, 8(1), 44-56.

Selig ET, Waters JM (1994). Track Geotechnology and Substructure Management. Thomas Telford, London.

Skar A, Klar A, Levenberg E (2019). Load-independent characterization of plate foundation support using high-resolution distributed fiber-optic sensing. *Sensors,* 19(16), 3518.

Steidl M (2007). Standards and tests of fastening systems. *AREMA Annual Conference Presentation.*

Terzaghi K (1955). Evaluation of coefficients of subgrade reaction. *Geotechnique*, 5(4), 297-326.

Tivari K, Kuppa R (2014). Overview of methods of analysis of beams on elastic foundation. *IOSR Journal of Mechanical and Civil Engineering*, 11(5), 22-29.

Vallabhan CVG, Das YC (1988). Parametric study of beams on elastic foundations. *Journal of Engineering Mechanics,* 114(12), 2072-2082.

Vlasov VZ, Leont'ev UNA (1966). Beams plates and shells on elastic foundations. Kudüs, Israel, Israel Programme for Scientific Translations.

Wang YH, Tham LG, Cheung YK (2005). Beams and plates on elastic foundations: a review. *Progress in Structural Engineering and Materials,* 7(4), 174-182.

Wehbi M, Bezgin NÖ (2019). Proposal and application of a new technique to forecast railway track damage due to track profile variations. *Transportation Research Record: Journal of the Transportation Research Board*, 2673(4), 568-582.

Wehbi M, Musgrave P (2017) Optimisation of track stiffness on the UK railways. *Permanent Way Institute Journal*, 135.

Worku A (2009). Winkler's single-parameter subgrade model from the perspective of an improved approach of continuum-based subgrade modeling. *Zede Journal*, 26, 11-22.

Zhao C, Wang P, Yi Q, Meng D (2015). Application of polyurethane polymer and assistant rails to settling the abnormal vehicle-track dynamic effects in transition zone between ballastless and ballasted track. *Shock and Vibration*, 2015, 826362.